Universität Hamburg
DER FORSCHUNG | DER LEHRE | DER BILDUNG

Magnetometric Studies on Flux Trapping Sensitivity of Superconducting Radiofrequency Cavities

Department of Physics

Bachelorthesis

Jennifer Ademoye

Prof. Dr. Wolfgang Hillert
Dr. Lea Steder

Universität Hamburg
Deutsches Elektronen-Synchrotron, DESY

May 18, 2025

Contents

Abstract

The increasing demand for high-performance superconducting radiofrequency (SRF) cavities in particle accelerators, especially in free electron lasers, has led to intensified research on optimizing cavity treatments. One promising recent development is the application of medium temperature heat treatments, which are typically performed at 250 °C - 350 °C in a vacuum furnace for several hours. It has been shown that these mid-T heat treatments enhance cavity performance by increased quality factors. However, the improved performance comes with the trade-off of an increased sensitivity to trapped magnetic flux of the cavity, which leads to lower quality factors. For the first time at DESY, the sensitivity to magnetic flux trapping is deduced from parasitic cavity measurements. The data retrieval and analysis in the scope of this project was only accessible due to a new systematic approach to both experimental test conditions and data acquisition systems. The sensitivity to trapped magnetic flux is systematically investigated on four cavities with very different heat treatments. Magnetic field measurements were conducted using three magnetic sensors mounted on the cavity equator. Additionally, the temperature gradients during the cooldown procedures are analyzed and showed consistencies in regard to the according cavity quality factors. Finally, results are compared to data of previous studies. These findings display the complex interplay between chemical and heat treatments, material properties and thermal dynamics on SRF niobium cavities. It can be confirmed that mid-T heat treated cavities show significantly increased sensitivity values 3-5 times higher than for cavities without this heat treatment. Moreover, differences in sensor signals after applying an external magnetic field highlight the influence of cavity characteristics, such as grain structure and defects. These findings provide a strong foundation for future optimization of cavity treatments for a second generation of EuXFEL cavities, which are required for the planned upgrade of the European XFEL accelerator.

1 Introduction

Superconducting radio-frequency (SRF) cavities with high performance are pivotal to modern particle accelerators. The research and development programs for these cavities constantly aim to reach efficient and continuous acceleration of charged particles with minimal energy loss. Promising applications in X-ray science and fundamental physics can be reached by enhanced cavity performance [1, p.1]. Accelerators such as the European X-ray Free-Electron Laser (EuXFEL) at Deutsches Elektronen-Synchrotron (DESY) uses niobium 1.3 GHz cavities to achieve high accelerating gradients and high quality factors. For a planned upgrade of the EuXFEL, a second generation of even better cavities shall be developed. New heat treatments are hence under investigation.

In recent years, medium temperature (mid-T) heat treatments have been under constant development. These treatments describe the exposure of the cavity to temperatures ranging between 250 °C and 350 °C in an ultra-high vacuum furnace for varying duration. These mid-T heat treatments have emerged as a promising method to enhance the intrinsic quality factor of SRF cavities. Yet, this improvement comes at the cost of increased sensitivity to magnetic flux which reduces the quality factor [2].

Consequently, a major challenge to improve cavity performance lies in the control of the magnetic flux trapping during cooldown. During the transition of the critical temperature T_c, the cavity reaches a superconducting state, at which type II superconductors, such as niobium, exhibit flux trapping behaviour. However, a higher sensitivity to trapped magnetic flux leads to an increase in surface resistance and with this to a lower quality factor. It is therefore essential that instead of increased flux trapping, the flux expulsion during this critical temperature transition is maximized. The observed sensitivity parameter quantifies to what extent the cavity is affected by trapped magnetic flux [3, p.1].

In this thesis, the magnetic behaviour and sensitivity to magnetic flux through the tests of four single-cell 1.3 GHz niobium cavities is investigated. These cavities differ in regard to their material structures and surface treatments. Thus, magnetic field measurements were performed in order to analyse the flux trapping behaviour in regard to relevant parameters, such as the different cavity treatments, temperature gradients, and grain structure properties. The results of these tests aim to gain a more comprehensive understanding of sensitivity to trapped magnetic flux and lay the foundation for future optimization of SRF niobium cavities.

In regard to the following structure, the thesis begins with a theoretical background covering key parameters and information relevant to understand SRF cavity performance. An overview of different cavity treatments is also presented. The following section describes the preparation and experimental setup used for the ensuing vertical cavity tests. Only the work in this thesis made it possible to deduce sensitivity data parasitically to standard vertical testing of cavity performances at DESY. Finally, the results are presented, analysed, discussed and put into context in regard to existing studies. These comparisons lead to a final conclusion with suggestions for future research.

2 Theoretical background

In this first section, the theoretical background relevant to the vertical cavity tests of this project is presented. Not only the cavity type and treatment, but also recent investigations on the medium temperature (mid-T) heat treatment on the cavity, and the methods for performance measurements of the cavity are discussed. Besides, the testing environment where the measurements are conducted are introduced.

2.1 Superconductors

X-ray free electron lasers such as the European XFEL operate with superconducting cavities. In an ideal conductor all electrons are accelerated freely without resistance. Perfect conductivity means that there is perfect shielding from external penetration of magnetic flux and that causes the flux density in a perfectly conducting metal to never change. An external magnetic field can cause two different magnetic behaviours in an ideal superconductor. First, a superconducting material is cooled down below the critical temperature T_c with the absence of an external field and the field is applied afterwards, then the magnetic flux will not penetrate the material. Second, a superconductor is

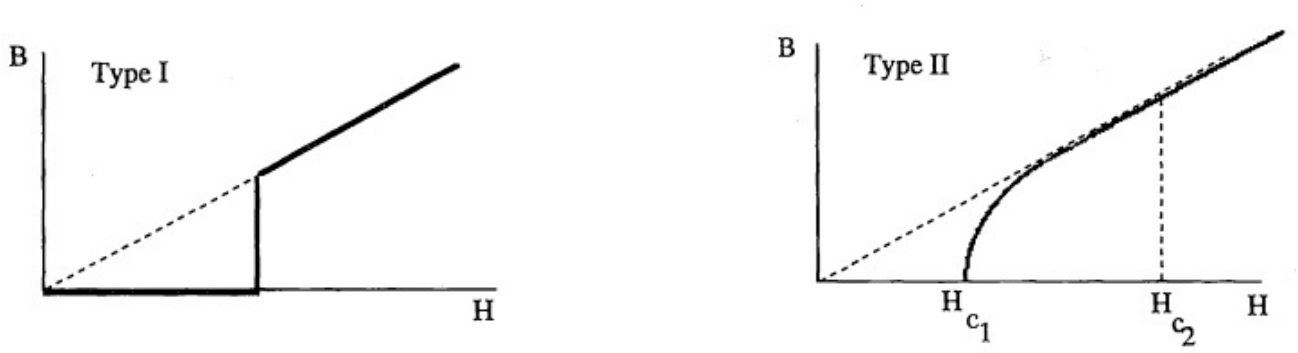

(a) (b)

Figure 1: (a) In a type I superconductor all magnetic flux penetrates the material when the critical field H_c is reached. (b) In a type II superconductor, magnetic flux slowly penetrates the material when the lower critical field $H_{c,1}$ is reached. A mixed phase occurs between $H_{c,1}$ and $H_{c,2}$. All magnetic flux enters the material at $H_{c,2}$ [4, pp. 96-97].

cooled to $T < T_c$ with the presence of an external field, then the magnetic flux penetrates the material and is not expelled after surpassing T_c. This difference shows that the final magnetic characteristic within the superconductor depends on the path of transition through the critical temperature. In the real world, superconducting materials do not behave as an ideal superconductor due to the Meissner effect described in section 2.3 [4, pp.80-82]. The Meissner effect describes the phenomenon of expelling magnetic flux from the material.

There is a difference between Type I and Type II superconductors regarding their magnetic behaviour. A type I superconductor remains in its Meissner state until it reaches the critical magnetic field H_c. Above H_c the superconductor is no longer in its superconducting state. A type II superconductor will expel magnetic flux until a lower critical magnetic field $H_{c,1}$ is reached. At this limit, flux vortices appear and start to penetrate the material. At this point, the material is no longer perfectly conducting but in a mixed phase. When a higher critical magnetic field $H_{c,2}$ is reached, the metal becomes normal conducting. Niobium, which is used for the SRF cavities in this project, is a type II superconductor. The different magnetic behaviour of a type I and type II superconductor is demonstrated in the following figure [4, pp. 96-97].

2.2 Superconducting Radiofrequency Cavities

Superconducting Radiofrequency (SRF) cavities are a pivotal aspect of modern particle accelerators - they are the resonators that supply the charged particles with energy. Specifically, SRF cavities resonate at microwave frequency. The electrons moving through the cavity will be continuously accelerated. This is achieved by the electrons pointing in the same direction as the electromagnetic field at half a wavelength $\lambda/2$ in every half a radio-frequency (RF). The optimal radiofrequency depends on the geometry and aperture of the cavity. The length of the cavity always consists of half a wavelength. Thus, cavities with shorter lengths perform at lower radiofrequency [4, p.3].

2.3 Meissner Effect

The cavity reaches its superconducting state when it is cooled through the critical temperature T_c at which the Meissner effect occurs. At this temperature, with an external magnetic field, the magnetic flux in the system is abruptly expelled from the material and the electrical resistance goes to nearly zero. The Meissner effect causes the magnetic flux to be actively expelled from the material when reaching the critical temperature even though the external field is present before this temperature transition. [4, pp. 66,82]

Impurities in the niobium material limit the maximum magnetic surface field. The higher the impurity in the material, the sooner a thermal breakdown occurs. Also crystal grain boundaries and their orientation in the niobium material impact its interaction with magnetic flux distribution. Moreover, niobium is a type II superconductor,

characterized by a lower critical magnetic field that can be surpassed by the ambient magnetic field. This allows magnetic flux vortices to be trapped inside of the bulk material inside so-called pinning centres. This trapping happens even when the material is in the Meissner state, as these pinning centres remain normal conducting. The trapping of magnetic flux is intensified by material impurities and grain boundaries [3, p.731][[5, 1]

2.4 Measurement Parameters

An important figure of merit of SRF cavity performance is the quality factor Q_0 as a function of the average accelerating field E_{acc}. The surface resistance R_s shows the dissipated power over the cavity surface. R_s is defined as the inverse quality factor with a geometry factor G specifically determined for TESLA-shaped cavities [6, p.297]. The surface resistance can be calculated with equation 2. The difference of the surface resistance ΔR_s of two different measurement modes that each have a different surface resistance R_s, contribute to the sensitivity of the material. The sensitivity showcases the increase of the surface resistance per trapped magnetic flux within the cavity when surpassing T_c. For a higher R_s a higher amount of magnetic vortices are trapped into the bulk material [4, 44-45].

2.4.1 Quality Factor and Accelerating field

Generally, a cavity is assessed in terms of its quality factor Q_0 as a function of the accelerating gradient E_{acc}. The accelerating gradient is measured in megavolts per meter (MV/m), whereas the quality factor Q_0 is a dimensionless quantity. E_{acc} determines the power of the accelerating field the cavity can induce on the electrons. The quality factor Q, on the other hand, is an intrinsic figure of merit for resonators and is defined as [4, p.44]

$$Q_0 = \frac{\omega_0 U}{P_c}, \tag{1}$$

where U is the stored energy and P_c is the dissipated power within the cavity walls. The goal for achieving high performances is to achieve as high a quality factor and as high an accelerating field as possible [4].

In this work, a number of equations are used to calculate the sensitivity. As mentioned afore, the quality factor Q_0 and the accelerating field E_{acc} are measured indirectly through the dissipated power in the cavity and then obtained through calculation. Furthermore, the corresponding surface resistance is calculated as the inverse function of Q_0 with a geometry factor for the cavity of $G = 271.5\Omega$ included. The factor of 271Ω was personally communicated by [7] and is slightly different from the used factor. The difference is due to a variation in the SRF simulation software but exhibits no practical difference in regard to data analysis.

It is to mention that the surface resistance of the material consists of three individual resistances, the resistance contribution by the Bardeen Cooper Schrieffer (BCS) theory $R_{BCS}(\mathrm{T})$, the residual resistance R_{res} and the constant residual resistance $R_{flux}(\mathrm{B})$. Only R_{flux} is dependent on the magnetic flux and is therefore influenced by the normal conducting pinning centres when applying an external field B_{ext} to the system. However, the temperature-dependent contribution is negligibly small for 1.5 K and it is therefore estimated that $R_{const.} = R_{S,1.5K}$. Because all magnetic field measurements in this work were taken at 2 K it can be approximated that $R_{BCS}(\mathrm{T}) = R_{S,2K} + R_{S,1.5K}$. While considering this approximation for R_{BCS}, the surface resistance can be expressed as $R_S(T, B) = R_{BCS}(\mathrm{T}) + R_{const.}$ [2, p.4].

The surface resistance used for the calculations of the sensitivity is a function of the accelerating field and shown in the following equation.

$$R_s(E_{acc}) = \frac{G}{Q_0(E_{acc})} \tag{2}$$

2.4.2 Sensitivity to Magnetic Flux

The sensitivity to magnetic flux describes the amount of surface resistance caused by the trapped magnetic flux within the cavity in its superconducting state. The sensitivity parameter is crucial to understand the performance of cavities in high magnetic fields. Another relevant parameter is ΔB_{ext}, which describes the difference in magnetic field inside the cavity between its normal conducting (NC) state and its superconducting (SC) state. In order to

determine the value of ΔB_{ext}, two different magnetic field values were used and the difference of both was taken. The first magnetic field value is taken before the application of the external field B_{ext}. After applying the field, the magnetic field increases, the cavity surpasses T_c and at 4 K the external field B_{ext} is removed again. After removal, some additional field higher than the original background field, before the application of the external field, is present. It is expected that this additional field represents the amount of trapped magnetic field and is named ΔB_{ext}. For instance, if the measured background field is about 0μT and the field after going through the described process is 4 μT, that results in $\Delta B_{ext} = 4$ μT. This ΔB_{ext} is material-dependent and is influenced by external factors, such as the temperature gradient during cooldown and material properties. ΔB_{ext} can expressed as

$$\Delta B_{ext} = B_{sc} - B_{nc}, \tag{3}$$

where B_{nc} describes the measured field in the NC state before applying the external field and B_{sc} describes the measured magnetic field in the SC state of the cavity after the removal of the external field. The magnetic field is applied with a Helmholtz coil, which is introduced in section 4.2.

It is assumed that this ΔB_{ext} represents the amount of magnetic flux that is trapped during T_c transition of the cooldown process. The amount of total magnetic flux measured in the system with B_{ext} consists of the part of the magnetic flux that is trapped into the cavity surface and another part that is expelled. In an ideal superconductor all magnetic flux would be expelled from the material. However, in reality data for this ideal case can only be achieved by simulation. Measurements show that some amount of magnetic flux are expelled from the material. The goal of SRF research is to achieve higher quality factors and therefore lower sensitivity to magnetic flux trapping into the material surface.

In order to calculate the sensitivity, the calculated surface resistances R_s and with it ΔB_{ext} are required. $Q_0(E_{acc})$ and thus equally $R_s(E_{acc})$ are retrieved for two different test modes. One of which is with an external magnetic field applied during cooldown (ΔB_{ext}) and one without it (baseline). During the magnetic field test at 2 K itself, the system is not exposed to B_{ext}. The exposure to B_{ext} only takes place during T_c transition. The field is removed again before the magnetic field test at 2 K is performed. The difference in R_s, measured for both of these test modes, is taken and named ΔR_s. A definition of this variable is the following.

$$\Delta R_s(E_{acc}) = R_{s,B_{ext}} - R_{s,baseline}, \tag{4}$$

$R_{s,B_{ext}}$ represents the surface resistance taken for the measurement in which B_{ext} is applied during T_c transition, and $R_{s,baseline}$ represents the surface resistance for a test with only the magnetic background field in the cryostat. Consequently, the sensitivity parameter can be calculated with [3]

$$S(E_{acc}) = \frac{\Delta R_s(E_{acc})}{\Delta B_{ext}}. \tag{5}$$

Cavities with mid-T heat treatment and impurities in their crystal lattice show a higher sensitivity to trapped magnetic flux [3, p.731].

2.5 Cavity Treatments

Depending on what characteristics are required on the cavity, different surface treatments are available.

After fabrication, all cavities receive a surface polishing to counteract the rough surface from the welding process during production. Surface polishing methods aim to remove the outer layer of a few hundred micrometers of impurities from the cavity surface. The polishing procedures dissolve Niobiumpentoxide Nb_2O_5 by using Hydrofluoricacid HF. Additionally, the electropolishing (EP) procedure uses the chemical sulfuric acid H_2SO_4. In this electropolishing procedure an electric field is applied and enables homogeneous removal of all particles among the whole surface material.

All chemical treatments must be followed by two mechanical cleaning procedures to remove dust and other contaminants from the cavity. Contaminations reduce the performance of the cavity. In the high pressure rinsing

(HPR) ultra pure water jets of 100 bar are used to rinse off the abundant particles inside the cavity. Additionally, an ultrasonic cleaning procedure is used to remove remaining particles with vibrations by ultrasonic waves.

After the cavity has undergone these cleaning procedures, it has to be handled in clean room environments only. After mechanical cleaning the cavity is mechanically stressed and therefore receives a thermal treatment of 800 °C. In high vacuum furnaces, hydrogen contamination can be counteracted and reduce the lower Q_0 behaviour at lower accelerating gradients that would be measured otherwise. Also, a high field Q-slope occurs at higher accelerating gradients and can be eliminated by heating the cavity to 120 °C for up to 48 h [8, pp.19-21].

2.5.1 EuXFEL Standard Treatment

All the different treatment types can be used in different order and with different parameters. These variations within the overall treatments are called a recipe and can be reproduced. A standard recipe for the current European XFEL cavities exists. This EuXFEL standard treatment consists of an EP of 110 µm to 140 µm and an HPR. After that a thermal treatment of 800 °C is conducted. Finally, a low temperature treatment of 120 °C is applied within this recipe [8, pp.19-21].

2.5.2 Medium Temperature Heat Treatment

Medium temperature (mid-T) heat treatments between 250 °C and 350 °C ranging from three to twenty hours have shown to impose a significant enhancement to the performance of 1.3 GHz SRF single-cell niobium cavities. Mid-T heat treated cavities show enhanced quality factors, an anti-Q slope with a maximum of the measured quality factor at E_{acc} values of around 25-35 MV/m. This reduced accelerating field has been observed for mid-T heat treated cavities [2, p.14]. It has been shown that heat treatments significantly impact the interstitial oxygen in niobium [2, p.5, 10]. This higher concentration of interstitial oxygen after a mid-T heat treatment leads to a reduced BCS surface resistance R_{BCS} compared to the baseline performance [2, p.6-8]. At temperatures between 200 °C and 300 °C the pentoxide layer decomposes but not the monoxide layer on the niobium surface. It is therefore approximated that only oxygen from this monolayer diffuses into the niobium surface. This oxygen diffusion is described by the parameter of the oxygen diffusion length l. Grain boundaries function as higher diffusivity areas and therefore the oxygen diffusion occurs faster. At first it was not known whether large grain cavities would be sufficiently impacted by mid-T heat treatments or if fine grain cavities were necessary for faster oxygen diffusion processes. Eventually, the oxygen diffusion length l does not appear to be related to large grain or fine grain niobium. A 300°C treatment consistently results in very high quality factors for both large grain and fine grain cavities and a characteristic anti-Q-slope [2, p.6-9]. In this work, three fine-grain and one single-crystal niobium cavity are analysed.

Some of the advantages of performing mid-T heat treatments are the absence of needing post-heating chemical surface treatments and it has the benefit of highly reproducible recipes. Thus, it eliminates the necessity of using additional gases such as nitrogen for the treatment. Cavities with a medium temperature heat treatment are observed to exhibit higher quality factor than cavities without this temperature treatment [2, p.1].

2.6 Accelerator Module Test Facility

With the advent of the EuXFEL at DESY a facility for testing SRF cavities and modules for this linac became necessary. All SRF cavities and modules require cryogenic testing before implementation in the accelerator. For this reason, the Accelerator Module Test Facility (AMTF) was built. The facility consists of one test stand for magnets, two vertical test cryostats (XATC1 and XATC2) for cavities and three test stands for the horizontal accelerator modules [9]. During four years, 832 SRF superconducting 1.3 GHz SRF cavities and 102 cryomodules were tested for their performance in the AMTF for the EuXFEL [10].

In each R&D test cryostat (XATC), a maximum of four cavities can be simultaneously tested. However, for this project, only one single-cell cavity was tested at a time. After preparing the test cavity and before performing the vertical test, the cavity is mounted to one of the inserts in the preparation area. For the cavity test, the insert with the cavity is craned into the cryostat. For the conducted tests in the scope of this project, only insert 2 with a single-cell cavity was used. The cryostat is placed inside a hole drilled in the AMTF ground and is covered by a concrete shield. In figure 2 a technical drawing of the cryostat structure (a) and an image of insert 2 (b) is shown. Vaporous helium is pumped into the cryostat with a diameter of 1725 mm and is 3950 mm in length. The cryostat

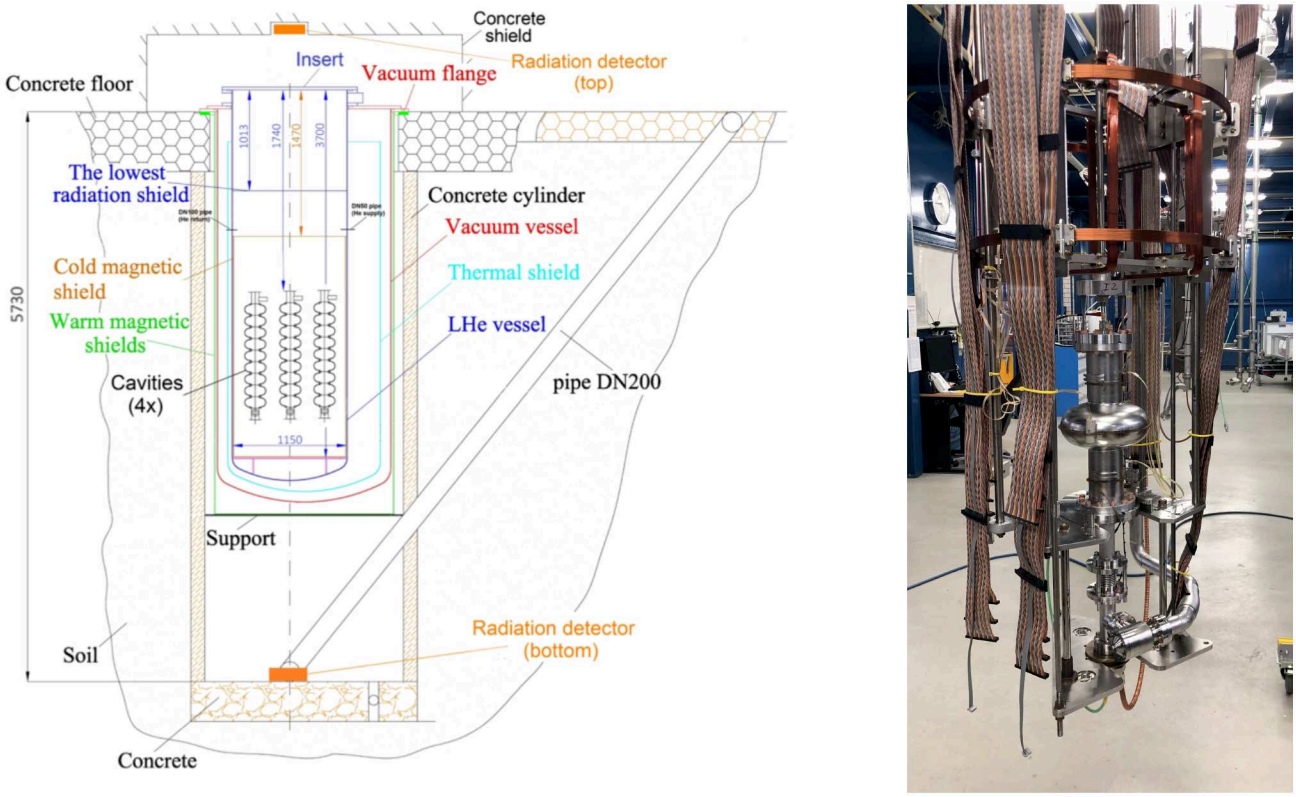

(a) (b)

Figure 2: Technical drawing of the test cryostat in the AMTF at DESY with four cavities [10, p.6] (a), and image of insert 2 with one single-cell SRF cavity (b).

is protected against overpressure with a pressure relief line. The basic components of one cryostat are the vacuum vessel, the liquid helium cryogenic tank and an active cooled thermal shield. When performing tests, the top of the insert marks the lid of the cryostat and contains the feedthrough with several connection components [11, p.1215].

Different shielding systems exist surrounding the cryostat inside the underground concrete hole. In order to reach a suppression background field from the geomagnetic field as low as $1 - 2$ μT, two inner shielding systems were necessary. One of which was made from μ-metal, the other one from Cryoperm™. The movable radiation shielding outside the cryostat, made of steel-reinforced concrete, can be placed above or be removed from the top of the cryostat by a control panel [10].

3 Motivation

Within the development of next-generation accelerator technologies such as the planned future upgrade of the European X-ray free electron laser, the optimization of superconducting radiofrequency cavities remains a fundamental challenge. Ensuring that these SRF cavities meet the demands of high quality factors at high accelerating fields requires further advances in the field of cavity treatments. Recent insights into medium temperature (mid-T) heat treatments have shown significant improvements in the quality factor of the cavity, which could potentially revolutionize the efficiency of these systems. However, these promising revelations come with a trade-off: while the sensitivity increases it also leads to a higher surface resistance and thus results in a lower quality factor.

Driven by this challenge, this study delves into the sensitivity parameter of the cavity to trapped magnetic flux. The first step to forging new state-of-the-art solutions to these current limitations is to comprehend in which way the enhanced sensitivity affects cavity performance and their magnetic behaviour. Not only are these findings crucial

for refining existing cavity processing techniques but also pave the way for the design of new cavity cryomodules while taking into account the risk of flux trapping, which would reduce the quality factors. Hence, quantifying the magnitude of the sensitivity effect defines the effort that needs to be made to ensure adequate magnetic hygiene. Ultimately, this work helps to make future accelerators such as the EuXFEL after its planned upgrade to be more efficient and be able to provide new operation modes for the users in order to cover wide-range applications within the broad field of scientific research disciplines.

4 Methods and Measurement environment

In the following section, the measurement arrangements with which magnetic field measurements are conducted are explained.

First of all, it is important to gain a general understanding of the magnetometer measurement instruments for magnetic field tests. As for data retrieval during magnetic measurements, three single-axis CryoMag® Bartington sensors and two three-axis CryoMag® Bartington sensors are used. The first are able to measure the magnetic field in the z axis only and the latter, each one consisting of three channels in the x, y, and z axis, are provided. An elaborate description of the performance and the test run characteristics of each investigated cavity is further discussed in section 6.

Before using the sensors for magnetic field measurements, tests to determine the offset and difference between the sensors were additionally executed. These tests are further discussed in section 4.1.4.

4.1 Bartington CryoMag® Sensors

Obtaining valid magnetic field data from the cavity in the cryostat depends on precise measurement and read-out processes. It is crucial to use reliable sensors wherefore the three-axis and single-axis CryoMag® Magnetic Field sensors by Bartington were chosen. The measuring methods and corresponding data results of these sensors were researched and evaluated in [12].

4.1.1 Three-Axis Magnetic Field Sensors

The CryoMag® Three-Axis Magnetic Field Sensors allow measurements of static and alternating magnetic fields in three axes. They can be placed into areas of temperatures as cold as 2 K and convert magnetic flux density into bipolar analogue voltages in x, y and z direction.

The sensing device contains three fluxgate sensor elements that are positioned orthogonally inside the probe part of the sensor. The fluxgate magnetometer is included in the sensor. This probe part is connected to a PCB (Printed Circuit Board) via a copper loom. This copper loom is designed to be suitable for cryogenic and room temperature, making it ideal for cryogenic measurements in the AMTF. The interconnection PCB forms the connection between the feedthrough and the probe part [13, p.5].

The general operation of a fluxgate magnetometer is as follows: it uses a magnetically sensitive core that is wrapped by two other coils. The excitation coil drives the core into magnetic saturation with an alternating current, the sensing coil detects the resulting magnetic response. When there is a magnetically neutral background, the response signal of the sensing coil is symmetrical over each electric cycle by the excitation coil. When a magnetic field is present within the fluxgate environment, the field alters the saturation behaviour and a measurable phase and amplitude change occurs in the detected signal. This change reflects the strength and direction of the magnetic field [14].

According to instructions by the company Bartington®, the PCB is to be placed inside of the feedthrough of the cryostat. It was privately communicated by Bartington® that this recommendation stems from the insufficiency of official cryogenic testing. For this project, this part is placed, contrary to recommendations, at the upmost thermal shielding of the cryostat. The cable from the probe and interconnection PCB further connects to the read-out device, which is introduced in section 4.3.2. On the probe part of the magnetic sensor, three arrows show the axis-direction and indicate proper positioning of the probe. The probe also contains the product code, measuring range and a serial number. The three-axis sensors measure in mV, a conversion factor provided by Bartington® converts ± 10 V to $\pm 70 \mu$T [15, p.4] to deduce magnetic fields. The names of the two three-axis sensors on the

equator of the cavity are $3D_1$ and $3D_2$. The positioning of each of the two sensors on the equator is slightly different for each cavity test and is not documented.

4.1.2 Single-Axis Magnetic Field Sensors and Fluxgate Magnetometer

The single-axis magnetometer consists of the Mag-01 sensors and the Mag-01H separate fluxgate magnetometer, but functions together as one measurement system. This magnetometer system converts signals measured by the sensor probe into a measurement of flux density. These data are then displayed on the front panel of the fluxgate magnetometer connected to each of the sensors in the form of the voltage output signal [16, p.7].

While the exact range of the sensors depends on the probe type, the single-axis sensor is able to quantify data with high precision. There are different probe types for different temperature and magnetic field ranges. For all conducted tests, probe type F was used as it functions at cryogenic temperatures and in the required field range of 0 to 0.2 mT. The cryogenic probes can only operate in close proximity to each other if they are mounted in an orthogonal manner. If the sensors are not mounted orthogonally to each other, they should be located farther in proximity than 10 mm to avoid interactions [16, pp.13-14].

A further feature of the Mag-01H fluxgate magnetometer is a sensitivity control of an increased resolution by a factor 10. This works with an attenuator which reduces the feedback to the probe and therefore increases measurement precision by a factor 10. The fluxgate magnetometer includes a switch to choose the precision range [16, p.7]. However, for all single-axis measurements, the precision was not set to the higher precision but kept at its original precision.

In this work, three of these single-axis sensors were used for testing. Mostly one of the three sensors positioned at the equator of the cavity is discussed to compare test results. Two other single-axis sensors are located at the lower and upper beam pipe of the single-cell cavity. The naming of the sensors is therefore $1D_{eqt}$ for the sensor at the equator, and $1D_{top}$ and $1D_{bot}$ for the locations at the upper and lower beam pipe. All single-axis sensors measure only in the z axis.

The fluxgate magnetometer directly displays data in the unit of µT but is then converted to mV by the Mobile Interlock (MI) read-out device. The company Bartington® provides a conversion factor of 100 from V to µT. In all read out data presented in this work, this conversion factor is used in order to present data in µT [16, p.7].

4.1.3 Low-pass Filters for Three-axis CryoMag® Sensor

Preceding measurements of several cavities showed the appearance of interruptive signals and inexplainable spikes in the retrieved measurement data by the three-axis sensors. These results can be seen in [12]. Although the origin of these signals could not be determined with certainty, it is assumed that they are caused by electrical components within the connections between the sensors and the read-out devices. As a result, six passive low-pass filters, one for each channel of the three-axis sensors, were prepared by the electrical lab of the DESY MSL group. The filters consist of a resistor of 2 MΩ and a capacitor of 1 µT. These filters prevent aliasing which can be caused within the data measuring process according to the Nyquist–Shannon sampling theorem, which states that the sampling frequency needs to be the same or more than the frequency than the maximum signal.

4.1.4 Comparative Analysis of Sensor Signals

Different magnetic field tests were conducted at room temperature in test stand XATC2 to confirm the validity of the signals produced by the three single-axis and the different three-axis magnetic sensors. The two sensor types, although both manufactured by Bartington®, have different characteristics and calibration. Testing served the purpose to determine whether the sensors measure the same signal in the same magnetic field environment.

Firstly, it had to be determined whether the magnetic sensors display correct absolute values of the magnetic field inside of the cryostat. This required tests with the sensors and to exclude as many surrounding components inside the cryostat as possible. For that purpose, a mobile magnetoscope by Förster with the probe PF-1000 was used and positioned alongside the sensors in a parallel manner in order to compare their absolute values. Thus, the probe parts of both, the single-axis sensors and the Förster probe PF-1000 of the mobile magnetoscope, were

mounted on a probe stick with a length of approximately 4.5 meters as shown in figure 3 [17, p.4].

As mentioned in section 2.6, the concrete shielding above the cryostat is movable. In the high precision measurements conducted with the sensors, the steel-reinforced concrete material is expected to have a minor influence on the magnetic signals inside the cryostat. To compare and test the signals produced by the different sensors, tests with open and closed concrete shielding were performed.

In [10, p.8], reference values for the magnetic field in the range of about 0.1 µT - 0.5 µT were measured. These values were taken for different cavity axes inside of the cryostat without any insert during data retrieval.

For the first tests conducted with this arrangement in the scope of this work, cable binders were used to mount the sensors on the probe stick. Afterwards it turned out that a small metallic component had falsified the measurement results. The absolute magnetic field had then be determined to be 800 nT by the Förster magnetoscope. After removal of this metallic components, the absolute value changed to 220 nT. This result lies within the range of the expected magnetic background field when comparing to the tests conducted in [10, p.8]. However, the metallic object used by accident here emphasizes the sensitivity of the sensor measurements. The lower precision limit of the Förster magnetoscope is 10 nT and thus negligible in the measurement range here [17, p.4].

(a) (b)

Figure 3: First measurement arrangement for tests of absolute values of single-axis sensors marked 1, 2 and 3.(a) Three single-axis sensors and one Förster magnetoscope probe mounted on probe stick of 4.5 metres in length. (b) Probe stick inserted through the lid of the empty cryostat at room temperature.

The Förster magnetoscope along with the single-axis sensors was used to calibrate the single-axis sensors for the absolute field inside of the cryostat. The sensors were placed 125 cm above the ground of the cryostat, which represents the exact placement of the sensors on the cavity equator on insert 2. This absolute field was determined by the magnetoscope and is about 220 nT.

By horizontal and vertical rotation an ambient magnetic field inside the warm cryostat of about 300 nT was calculated for the sensors placed 125 cm above the ground of the cryostat. As the sensors were last calibrated in 2023 showing an offset of about 32 nT [18], an increase of the measured ambient field to 300 nT is improbable. The tests with which the 300 nT were determined, were among the first tests on the probe stick conducted. Due to systematic and practical limits, it was not possible to align the sensors exactly in the horizontal or vertical di-

rection on the stick. Measurement uncertainties are therefore likely and the test was repeated with a more reliable measurement system with values in table 1. In order to achieve a reliable offset of the sensors, the sensors require re-calibration by the company Bartington®.

However, an additional issue was determined in the electronic structure of the read-out arrangements for the three single-axis sensors. Each of the single-axis sensors is connected to a fluxgate magnetometer for read-out, which is then connected to a self-made powermeter. The single-axis sensors result in reliable data and then send the data via the fluxgate magnetometers to the powermeter. The reading precision of this powermeter, which also transfers all data to the server, does not fulfill the precision requirements of this measurement. Up to that point, reliable data of the single-axis sensors could only be manually read out from the fluxgate magnetometer and not be sent to the server for accurate data analysis. All tests of the sensor signals were first performed with this unreliable read-out system. Due to the lack of precision by the powermeter device for the signals of the single-axis sensors, it was eventually exchanged by a modified mobile interlock device (MI) with the ability to record data with higher precision. Details regarding this device are discussed in section 4.3. This MI was used for all ensuing cavity measurements at 2 K recorded by single-axis sensors. The tests of the sensor signals were repeated with more interconnected and reliable measurement systems where data could be directly read out from the server. Only the results of the repeated tests are presented in this section and matched the results of the first time of testing with manual read-out.

For the next test run, again three single-axis sensors were mounted on the probe stick with non-magnetizing tape. The magnetoscope was not used again and the updated read-out system with the mobile interlock instead of the powermeter was used. The measured values for the single-axis sensors and one three-axis sensor marked C are presented in table 1 and were measured with open concrete shielding.

Table 1: Measured magnetic field values for test with probe stick in cryostat without concrete shielding.

Sensor	B [μT]
$1D_{top}$	0.110
$1D_{eqt}$	0.081
$1D_{bot}$	0.085
$3D_C$	0.090

The values in table 1 are comparable for all four sensors which proves the functionality of the sensors to a common reference environment. The ambient magnetic field inside the AMTF was measured to be 20 - 40 μT in the AMTF. Considering the shielding in the cryostat environment, a significantly lower value is expected and fits the range of magnetic field values measured by the sensors in table 1. The values in the table are mean values of several data points within the probe stick test run. These values show the ambient magnetic field inside the warm cryostat with the open movable concrete shielding.

In an additional test series for the sensors, three single-axis sensors ($1D_{top}$, $1D_{eqt}$ and $1D_{bot}$), and two three-axis sensors $3D_1$ and $3D_2$ (A and B) were mounted on cavity 1RI02 on insert 2. The exact placement of the sensors was performed as is described in section 4.2. During the whole test series, the cryostat was at room temperature. For both of the two different test conditions, which consists of the open and closed movable concrete shielding, data was acquired. Corresponding results are presented in table 2 and 3. The magnetic field values B presented in the tables were determined by taking the mean value of several data points over a time range with constant temperature. All data of the single-axis and three-axis sensors were taken for the z axis.

Table 2: Magnetic field tests with open concrete shielding on insert 2.

Sensor	B [μT]
$1D_{top}$	0.01
$1D_{eqt}$	0.04
$1D_{bot}$	0.30
$3D_1$	0.04
$3D_2$	0.30

Table 3: Magnetic field tests with closed concrete shielding on insert 2.

Sensor	B [μT]
$1D_{top}$	0.03
$1D_{eqt}$	0.06
$1D_{bot}$	0.31
$3D_1$	0.06
$3D_2$	0.13

These data were taken from the server and converted with an individual conversion factor for each sensor type to enable comparison. The conversion factor from V to μT for the three-axis sensors is 7 and for the single axis sensors is 100, both provided by Bartington®. The values of all three-axis and single-axis sensors for both measurement conditions of the opened and closed concrete shielding are in the expected range of the ambient magnetic field and lie within expectation when taking into account the shielding systems of the cryostat.

In table 2 for the open concrete shielding variations of the magnetic signal between 0.01 μT and 0.30 μT can be seen. That means the difference lies between 1 nT and 300 nT. In table 3 for the closed concrete shielding the magnetic field signal range between the sensors is within 0.03 μT and 0.31 μT. This is about the same upper and lower range limit as for the magnetic values at the open concrete shielding. These magnetic field values are expected with the insert and therefore higher than for the probe stick in table 1 due to increased magnetization from the insert and the cavity components. The different values measured by the same sensor for the test conditions of the open and closed concrete shielding suggest different magnetization by different components. Influences on the magnetization can be caused by inhomogeneous magnetic properties of the cavity and other surrounding magnetizing components in the insert.

Nevertheless, the difference of magnetic field of each sensor between the open and the closed concrete shielding conditions can not definitely be seen in data. The reason for this is the very low increase of about 25 nT in magnetic field in the z axis by the concrete shielding. The low influence is expected and required in order to have an impact as small as possible on the magnetic field tests conducted below the concrete shielding. This behaviour is rooted in the magnetizing steel components inside the concrete material. The signals for the magnetic field change between the cryostat with or without the concrete shielding were retrieved with cavity 1DE9 which was different from cavity 1RI02 with which the sensor signals were determined previously. However, the impact of the concrete shielding is expected to be comparable.

Supporting data of the influence of the concrete shielding on the magnetic field are presented in figure 4.

The magnetic field measured responds only in the direction of the z axis. The graph of the z axis sensor component shows an increase in magnetic field when closing the shielding (B). The field remains elevated during the presence of the concrete shielding (B). The magnetic field is measured higher by about 25 nT during the test of the closed concrete shielding. When the concrete shielding is opened again, the magnetic field declines to its original state and reaches its original ambient field (A and C) . This change of 25 nT is comparable to the lowest limit of the range in magnetic field tests among the sensors on the cavity in tables 2 and 3. The different values within these two tables for the two different test conditions do not show significant differences due to the minor change of magnetic field induced by the concrete shielding.

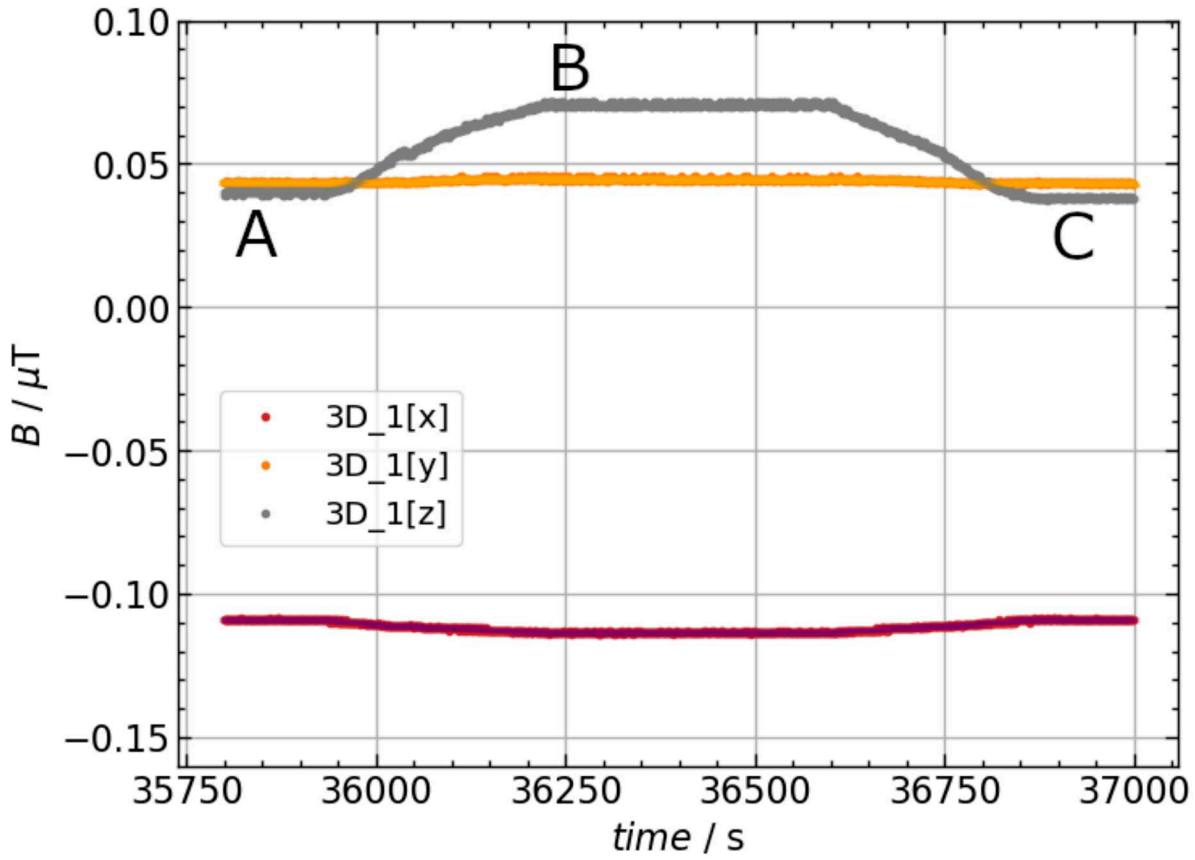

Figure 4: Magnetic field as a function of time. The signals are taken at room temperature and with no applied magnetic field. Seen is the change in magnetic field of the closing and opening of the external concrete shielding for the x, y and z axis of one of the three-axis sensors.

4.2 Measurement Infrastructure and Cavity Setup

The measurement arrangements of the single-cell cavity and the sensor positions were developed over the course of the measurements and are described in this section alongside the characteristics of the Helmholtz coil.

Before starting cavity tests for this project, only one three-axis magnetic sensor and the three single-axis sensors were used for magnetic field measurements. For more comprehensive comparability it was then decided to upgrade to two three-axis sensors. During all magnetic field measurements on cavities, the two three-axis sensors (A and B) together with one single-axis sensor are placed around the equator of the cavity. The two three-axis sensors are placed approximately opposite of the cavity equator whereas the single-axis sensor is placed between them as can be seen in figure 5. The other two single-axis sensors were mounted on the upper and lower beam pipe of the single-cell cavity. The exact placement of the three-axis and single-axis sensors slightly varied each time the cavity was replaced and a new vertical test was conducted. The variations in their positions are assumed to be in the millimeter range and are not documented. The difference between the sensor of the upper and lower beam pipe was manually measured of approximately d = 225 mm and is confirmed in [2, p.12]. Figure 5 represents an exemplification of the sensor arrangements of all magnetic field measurements on the cavities.

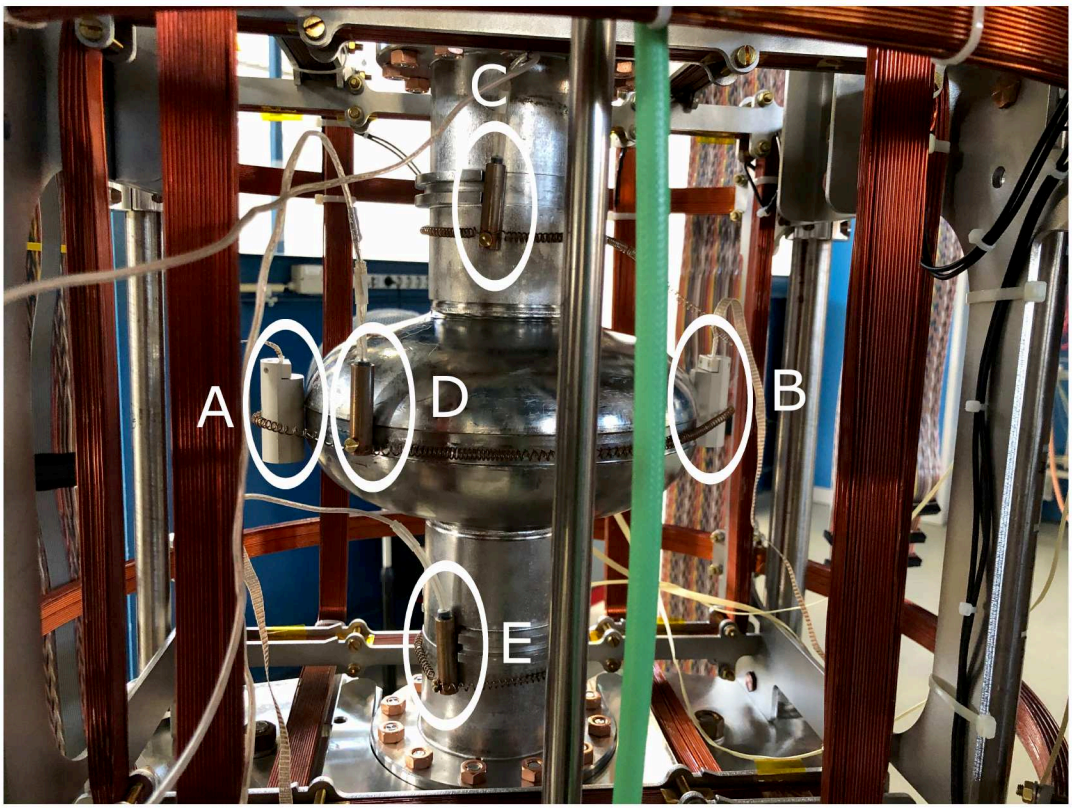

Figure 5: Positions of the two three-axis (A and B) and three single-axis sensors on the cavity equator (D) and on the upper (C) and lower (E) beam pipe. Also visible are the surrounding Helmholtz coils.

Measurements with an external magnetic field B_{ext} are required for data needed for sensitivity calculations. To perform magnetic field measurements with an externally applied magnetic field B_{ext} a copper Helmholtz coil is used. The coil consists of 100 windings, the radius and distance to the middle point of the coil measures d = 280 mm. A homogeneous magnetic field induced by the coil is expected. With the following equation 6 the expected magnetic field can be theoretically determined [19].

$$B(z) = \frac{\mu_0 N I}{2}\left(\frac{R^2}{R^2 + (\frac{z-d}{2})^2)^{3/2}} + \frac{R^2}{R^2 + (\frac{z+d}{2})^2)^{3/2}}\right)\vec{e_z}. \tag{6}$$

where N describes the number of windings, R the radius, d the distance between the coil and the middle point where $z = 0$ mm, and z the position on the z axis and μ_0 the vacuum magnetic permeability. The magnetic field was calculated for the position at the circumference of the cavity equator, which is a radius of $z = 105$ mm from the centre point of the cavity. In the measurement process, a current of 23 mA and an upper voltage limit of 2 V is applied on the coil.

The orientations of the magnetic fields induced by the Helmholtz coils are described through the axis elements in the three-axis and single-axis sensors and its position. The axis elements of the three-axis sensors are seen in the following figure and can be compared to the sensor positions of figure 5.

Figure 6: Axis orientations of the x, y and z axis on the three-axis sensor.

The Helmholtz coil consists of three times two opposite facing copper coils to induce the magnetic field in the corresponding axis direction. The x axis is oriented horizontally, pointing through the left and right side when viewed from the front as in figure 6. The y axis is oriented between the back and the front of the sensor, passing through its central point. The z axis is oriented vertically, pointing downward and upward through the centre point of the sensor. In this work, the magnetic field is applied only to the z axis.

Despite the calculated magnetic field, reality shows some deviation from the theoretical value. The calculated magnetic field results in about 7.2 µT, whereas measurement data shows magnetic fields in the approximate range between 8 µT and 10 µT. The underlying cause for this variance is likely due to the locations of where the electric current is measured after surpassing a filter system with a resistor. The locations between the two measurement points also have a spatial distance of about 5 meters. The magnetic field results presented in the data were measured by the sensors inside the cryostat. The reason for the difference in the calculated magnetic field and the actual measured field in the cryostat may be attributed to the filter systems and resistances within the cable connections.

The magnetic flux value of about 10 µT induced by the Helmholtz coil is chosen according to a commonly used value within the SRF community, as was also used in [3, p.733]. In the practical realization, the chosen current of 23 mA was determined with the help of the measurement system, where the measured magnetic field was directly read out. By this direct read-out of different currents applied to the coil, the required current of 23 mA to reach a magnetic field of about 10 µT could be determined. A higher magnetic field causes higher magnetization of the surrounding components. A lower magnetic field would lead to a higher impact of the offset and background field inside of the cryostat.

4.3 Data Acquisition

The data acquisition and measurement system consists of several components, which are presented in a schematic presentation for a better overview. This section provides a more detailed description of these components.

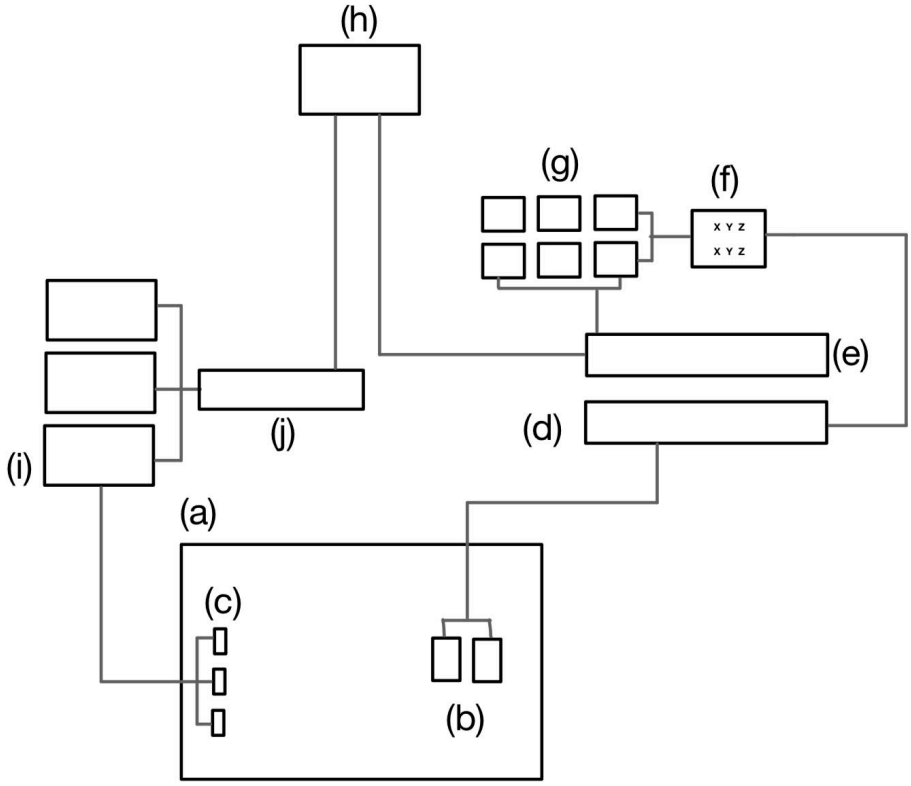

Figure 7: Schematic presentation of measurement and read-out components: (a) cryostat in XATC2, (b) two three-axis sensors, (c) three single-axis sensors, (d) Power Supply Unit, (e) Panelmeter, (f) Dispatcher Box for the x, y and z axis channels, (g) Low-pass filters, (h) Server AV2, (i) Fluxgate magnetometers of the single-axis sensors, (j) Mobile Interlock (MI). All five sensors are placed on a single-cell cavity that is placed in the cryostat.

4.3.1 Powermeter

The powermeter, also named panelmeter, was built from different components in-house. It records an analogue measurement signal and transfers it into a RS232 signal. Afterwards, this signal is converted into another signal that can be sent through the USB port in the device and connect it to another device, in this case to the server for remote data read-out.

4.3.2 Power Supply Unit

The DecaPSU device by Bartington® acts as a power supply unit of ± 15 V DC for each connected three-axis magnetic field sensor. The sensors are placed inside of the cryostat on the cavity and are connected to the DecaPSU via the feedthrough. The DecaPSU reads out the output of the sensors. In the conducted tests, two out of the ten outputs available were in use. In addition, the DecaPSU device includes a low-pass 4-pole filter that removes high frequency noise and other types of signal interference breaking through from the incoming signal. The DecaPSU device then sends data through the low-pass filters and to the powermeter, from where data is sent to the server for storage and read-out [20, p.7].

4.3.3 Mobile Interlock

For the read-out of the single-axis magnetic sensors a Mobile Interlock (MI) device was installed. The MI translates analog measurement signals and sends it to the server. This device can read data with very high precision compared to other read-out systems. The original MI voltage measuring systems had a range between ± 1 V and ± 10 V, which were then measured with a 12 bit ADC device. This causes the precision with approximately 488μT to be insufficient for the magnetic field tests.

For this reason, the device read-out systems were adjusted for lower voltage ranges required for the tests. This was realized by mounting two temperature sensors. These temperature sensors function as voltage measurement systems. Thus, the inputs of the MI were adjusted for lower voltage ranges with an electric trimmer. After this modification, the read-out of the magnetic signals by the MI had adjustable precision. The precision can be switched between a maximum range of about 250 mV which converts to 12.2 µT or to 25 mV which converts to 12.5 µT. The conversion between the units V and µT was done with the conversion factor of 100 provided by Bartington®. The lower precision rate measures the signal with a precision of up to 12.2 nT and when switching a higher precision of up to 1.2 nT is possible. All magnetic measurements for cavities 1DE9, 1DE19, 1AC8 and 1RI02 were taken with this modified MI device for the single-axis sensors. Due to the higher magnetic field when the external field was applied during cooldown processes, a higher range was necessary and therefore had to be set to the lower precision of 12.2 nT. However, for all baseline tests and testing without the exposure to a strong field, the total magnetic field range was sufficiently low and the MI read-out systems were set to the higher precision of 1.2 nT.

5 Determination and Propagation of Uncertainty

The uncertainty determination for all data in the upcoming sections is explained here. Data of two three-axis sensors and one single-axis sensor are used for analysis and further calculation. First of all, statistical uncertainties are discussed.

For the three-axis sensors by Bartington®, a root mean square noise value at 1 Hz of the device was given with about 14 pT according to the data sheet of [15, p.4] The 14 pT were calculated by using a sampling frequency of 1 Hz with 0.5 used for the upper and lower limit of the signal oscillation.

This noise provided by Bartington® is negligible here since the values are of the order of some tens or hundreds of nanoteslas. Also, there is the standard deviation of the three-axis sensors. As this standard deviation is calculated from data that is retrieved from the last step of the data processing chain, this deviation includes several uncertainties from read-out devices, electronic connections and the background field in the cryostat discussed in section 4.1.4. The standard deviation was determined using the `numpy.std` function of the `numpy` library in python over several data points. To determine the standard deviation, data of several days and at different temperatures between 2 K and 30 K were used to calculate the mean value. With this `numpy.std` function, the standard deviation σ_{3D} of $3D_1$ was determined to be about 0.9 nT and of $3D_2$ with about 1.0 nT. The higher standard deviation of about 1.0 nT was used in all ensuing data presentations of the three-axis sensors.

Regarding the single-axis sensor, the maximum resolution of the sensors is given with 0.1 nT by Bartington® [21, p.3] and is therefore also negligible in the range of the conducted tests. The standard deviation σ of the single-axis sensor placed at the equator is calculated from several magnetic field data points of several cavity tests at different temperatures between 2 K and 30 K. For the sensor $3D_{eqt}$ the standard deviation is about 90 nT. This σ_{1D} is used in all ensuing data for this sensor. For all measurement results, the standard deviation of the three-axis and the single-axis sensors is used as 1/2 σ_{3D} and 1/2 σ_{1D} into each axis direction of the magnetic field, resulting in σ in total. The uncertainty of the magnetic field data was included in all ensuing magnetic plots at 2 K. Due to the lower resolution in the wider magnetic field data range during the cooldown plots, the error bars were omitted here. The error bars in the cooldown plots would distort the image without providing additional information.

In addition, an uncertainty propagation of the quality factor Q_0 as a function of the accelerating field E_{acc} had to be performed. The complexity inherent to these specific measurement types makes it difficult to determine reliable uncertainties. Referring to previous tests regarding this matter as presented in [10, p.9] the uncertainty is about 10 % for Q_0 and about 20 % for E_{acc}. When comparing two test runs between each other, then this uncertainty is an overestimation. These uncertainties were determined for independent RF measurements with the reconnection of

cables, uncertainties of the test devices and the finite directivity of the directional couplers. Within a single vertical test the uncertainty is significantly lower with 3 % for Q_0 and 1 % E_{acc}. Despite this overestimation, the higher uncertainty factors are used to enable comparison with external results of different vertical tests. Although the uncertainty of 10 % and 20 % is not valid for the same vertical test, they are plotted and presented as such. Thus, they are not valid for quality factor comparison within the same vertical cavity test. The uncertainty propagation was performed using the following equation from [22, p.14].

$$E_G = \sqrt{\left[\sum_{j=1}^{n} \left(\frac{\partial G}{\partial x_j}\right)^2_{\bar{x}_j} \sigma^2_{x_j}\right]} \tag{7}$$

where G is the uncertainty of the function to be determined, x_j dependent variable of function G, E_G is the uncertainty of the variable G, and σ_{x_j} is the standard deviation of the directly measured variable x_j.
The uncertainty of Q_0 and E_{acc} was propagated through the surface resistance R_s, the difference of the surface resistance of the two measurement modes ΔR_s and through the sensitivity S. All ensuing data are presented with this uncertainty. The propagation for E_R and E_S was conducted according to the following two equations 8 and 9. The equations of the surface resistance R_s and the sensitivity S that are used for the uncertainty propagation are seen in equations 2 on page 5 and equation 5 on page 6. For determining the uncertainty of S,the standard deviation σ_{3D} for the three-axis sensors was applied to the value for ΔB_{ext}.

$$E_R = \sqrt{\left(\frac{\partial \Delta R(Q_0)}{\partial Q_0}\right)^2 E^2_{Q_0}} = \frac{\Delta R(Q_0)}{Q_0^2} E_{Q_0} \tag{8}$$

$$E_S = \sqrt{\left(\frac{\partial S(R,\Delta B)}{\partial R}\right)^2 E^2_R + \left(\frac{\partial S(R,\Delta B)}{\partial \Delta B}\right)^2 \sigma^2_{3D}} = \sqrt{\frac{1}{\Delta B^2} E^2_R + \frac{R^2}{\Delta B^4} \sigma^2_{3D}} \tag{9}$$

The uncertainty of E_{acc} remains constant at about 20 % during the complete uncertainty propagation. For this reason, the uncertainty of E_{acc} is not shown in data representation and no horizontal error bars are shown for this variable.

Additionally, there are systematic uncertainties such as the placement of the sensors on the cavity. The precise positioning was not determined for the different measurements and therefore causes a small uncertainty in the millimeter range when comparing different cavity tests among each other. Nevertheless, the three sensors on the equator were also placed in differing distances of several centimeters on the azimuthal locations on the equator. The placements of the single-axis sensors on the upper and lower beam pipe are also assumed to have differences in the millimeter range but are not considered in data results due to their different spatial location. The different angular or axial position of the sensor can lead to the sensing elements to measure the magnetic field with a minor offset.

In order to get rid of this uncertainty factor, it is suggested to mount defined holding devices for each sensor on the cavity. With this method, the placement of the sensors would be comparable between vertical tests of different single-cell cavities.

Moreover, all magnetic field data for the magnetic field tests with an external field during cooldown and also for all baseline tests were taken at 2 K with a small deviation from the exact temperature value. The magnetic field data were taken at 2 K at the same time of the quality factor tests. The average of the different temperature values was taken. The sum of all values is divided by the number of values as seen in the following equation and results in an approximate temperature value of $\bar{T} = 1.997$ K. In this equation $\bar{T}$ is the average temperature value, n is the number of values and T_i are the individual values.

$$\bar{T} = \frac{1}{n} \sum_{i=1}^{n} T_i \tag{10}$$

For all temperature data points in ensuing data, always the temperature sensor mounted on the equator of the cavity was used and not the temperature sensors on the upper or lower beam pipe. The temperature sensor on the equator enables more precise correlation of the temperature and magnetic field data measured also at the equator of the cavity.

6 Results of Magnetic Field Measurements and Sensitivity

In this section the results of different magnetic field measurements on cavities 1DE9, 1DE19, 1AC8 and 1RI02 and the according data interpretation are presented and discussed. All magnetic field tests with an external field (B_{ext}) applied during cooldown and all baseline test data are shown for the same time at which the quality factor test is performed. That means that for each test run the magnetic field data matches the time of the corresponding quality factor data.

6.1 Fine Grain Cavity with Electropolishing

Cavity 1DE9 was manufactured from Heraeus fine-grain niobium. Although it has undergone multiple treatments since its production, the most recent was a 20-micron electropolishing (EP) treatment in order to reset the surface.

The measurement conducted on cavity 1DE9 consists of two test modes: one with an external magnetic field (B_{ext}) of about 10 μT applied by the Helmholtz coil and one without any external field (baseline). These definitions are chosen for all ensuing measurements. For 1DE9 each test was performed two times, each round consisting of both test modes is referred to as a test run (TR). The uncertainty of the temperature value is explained in section 5. For the tests with B_{ext} the voltage by Helmholtz coil was always applied at a temperature at about 30 K and was removed at 4 K. That means, B_{ext} was always removed from the system before the 2 K measurement started. The precise orientation of the applied magnetic field is explained in section 4.2.

Due to the magnetic field in the system applied only on the z axis, the field of all tests was only determined on the z axis. In order to compare to the x and the y axis of the three-axis sensors, according data is shown in figure 8. This exemplification serves a more complete overview of the whole measurement instrument and capabilities of the two three-axis sensors.

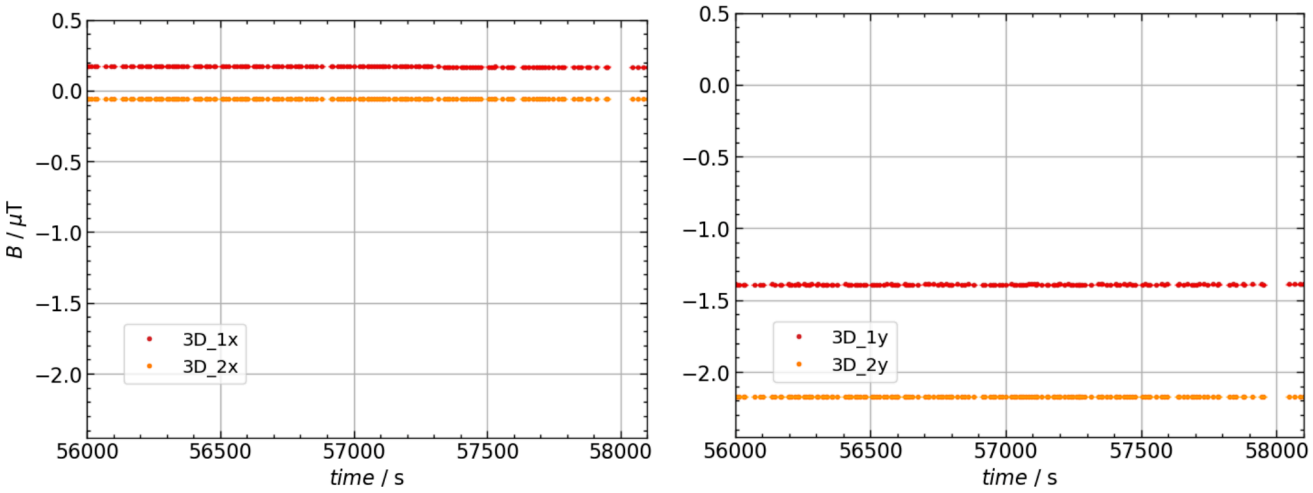

Figure 8: Exemplification of the magnetic field as a function of time measured at the x and y axis for TR 1 of cavity 1DE9. The test was performed at 2 K with B_{ext} = 10 µT. The three-axis sensor $3D_1$ is located at the equator of the cavity.

The difference between the two three-axis sensors on the equator $3D_1$ and $3D_2$ sensor is lower for the x axis and larger for the y axis as can be seen in figure 8. The measured field is low for both of the axis directions. That is due to the external magnetic field applied only on the z axis. The magnetic field signals of the x axis show an absolute value of nearly 0 µT. The absolute value for the y axis is higher with about 1-2 μT. The negative scaling of the magnetic field is due to the field applied through the centre point of the cavity. Also, the magnetic field by the Helmholtz coil is not perfectly uniform around the centre. Considering the high precision of the measuring instruments, this can cause some magnetic flux to be measured also in the x and y direction of the coil. Besides, it is possible that the sensors were not placed in ideal alignment with their assigned axis directions on the coil and

therefore cause values deviating from the expected background field.

The magnetic signal between TR 1 and TR 2 of cavity 1DE9 in regard to their x and y axis is comparable. These signals in x and y are also comparable to the cavity test of 1DE19. For all three of these tests of 1DE9 and 1DE19 the x axis shows a field near 0 μT whereas the y axis shows a field of about $1 - 2\mu T$. This implies non-uniform magnetization of the three-axis sensing elements differently.

A better correlation of influences on magnetic field data provides the temperature gradient during cooldown. Two different types of temperature gradients were used in this work, which contribute to measurement uncertainties when comparing magnetic field data. The time-dependent cooldown gradient is calculated with $\Delta T/\Delta t$ for each cooldown and is taken from a temperature value above and below $T_c = 9.2$ K. For this type, only the temperature sensor on the cavity equator is used to determine the cooldown gradient. An exemplification of how this cooldown gradient is determined is presented in figure 9 (a). A spatial temperature gradient ΔK is also calculated by using the temperature difference between the two spatially different temperature sensors on the cavity, that are located at the upper and lower beam pipe. The methodology with which this spatial temperature gradient is determined is shown in 9 (b).

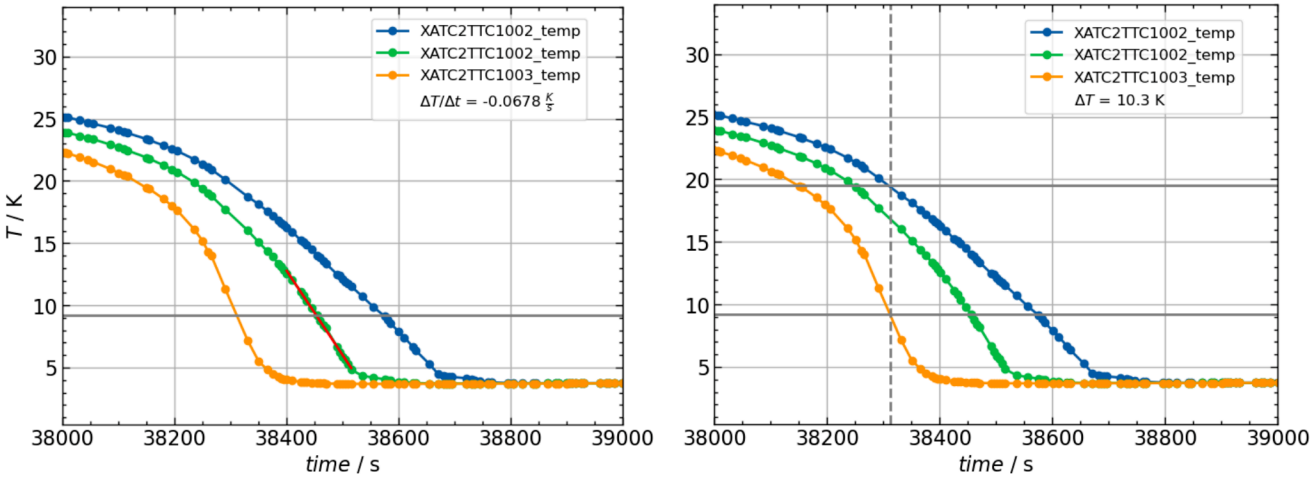

Figure 9: Temperature as a function of time. Methodology of determining the cooldown and spatial temperature gradient exemplified on cavity 1DE9. Data are taken during cooldown from 30 K to 4 K and a magnetic field of 10 µT is applied during this procedure. (a) The slope of the temperature difference is taken as shown by the linear regression (red line). (b) The spatial temperature gradient is determined by taking the difference in temperature at the same time between the temperature sensor of the upper and lower beam pipe (grey lines).

The methodology of determining the spatial temperature gradient is taken from [2, p.12]. [23, p.1201-1202] has shown that larger temperature gradients during cooldown lead to lower magnetic flux trapping.

It is important to observe magnetic field behaviour during the transition of the critical temperature T_c during cooldown in order to understand the response of the cavity to its superconducting state. In figure 10 the transition of T_c during cooldown is shown for TR 1 and TR 2 of 1DE9. Due to the expulsion of magnetic flux when the cavity enters a superconducting state, an increase in measured magnetic flux is expected. In figure 10 the magnetic field starts with a low background field (A). Then it changes to a value of 8-10 µT after the application of the external magnetic field B_{ext} of about 10 µT (B). The unrelated data points that appear at the time of the magnetic field application are assumed to be due to disturbance in the power supply of the coils. These data points are no longer present in TR 2 or at any other cavity test of this work. At the later T_c crossing (C) during cooldown, an additional change of field is measured and reaches an absolute value of about 10-12.7 μT for the different sensors (D). This further change suggests the expulsion of magnetic flux due to the state transition to superconductivity of the cavity. The Meissner effect takes place here. The magnetic field remains at this order until the temperature is as low as $4K$ and the external magnetic field is removed (E). Removing B_{ext} is observed as a change in magnetic field back

to the background field and a further change in the other axis direction. The difference in magnetic field before applying the external field (A) and the measured field after removing the external field (E) is referred to as ΔB_{ext}, which is used to calculate the sensitivity. This suggests the appearance of the field that was first trapped inside of the cavity and remains present during the state, in which the system is exposed only to its background field. ΔB_{ext} values of TR 1 and TR 2 of cavity 1DE9 are presented in table 4 later in this section.

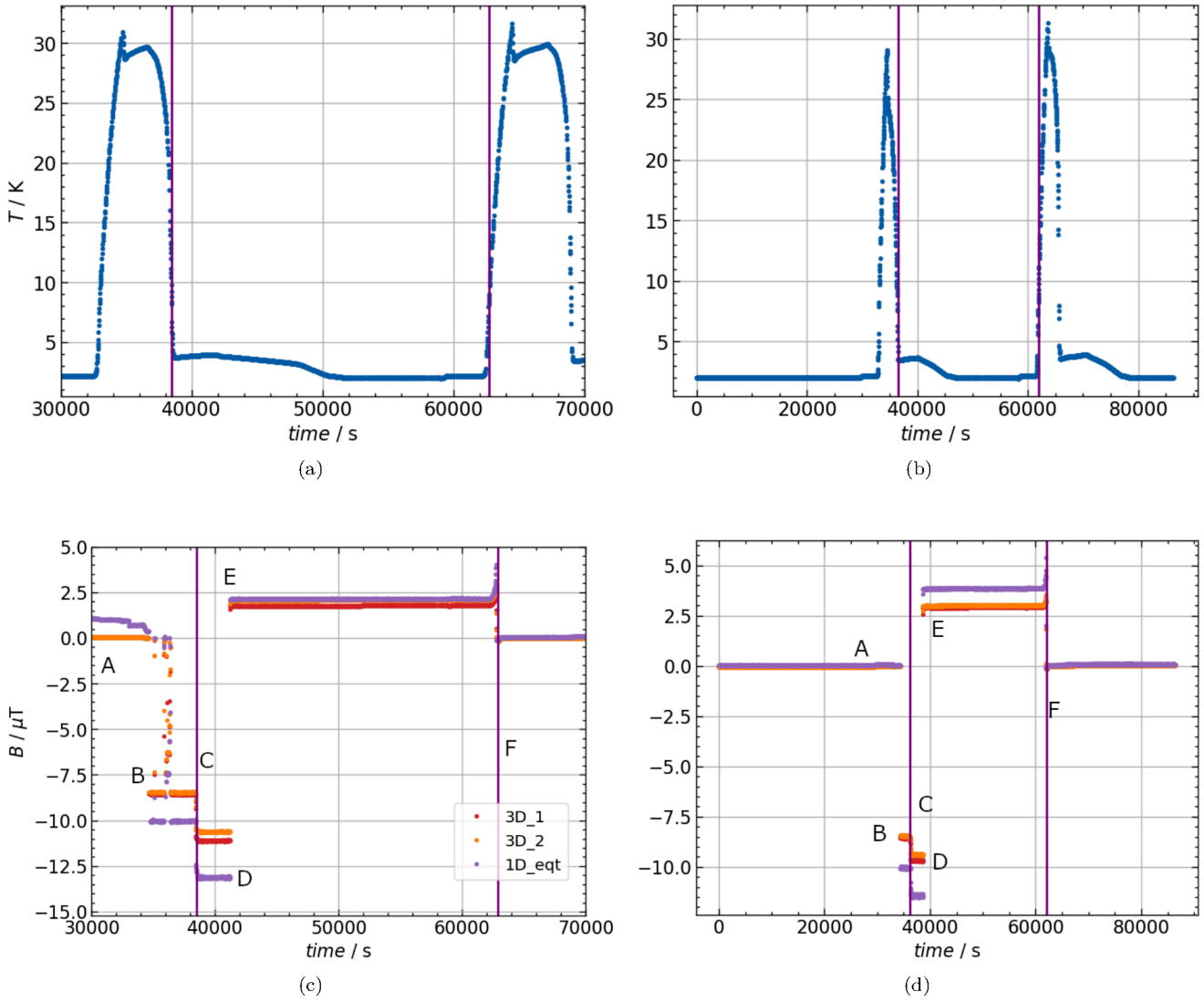

Figure 10: Comparison between T_c transitions of cavity 1DE9. The tests show the cooldown from 30 K to 4 K and an external magnetic field of 10 µT applied at 30 K and turned off at 4 K. (a) and (b) show the temperature as a function of time and represent two warmup and cooldown periods. The magnetic field behaviour as a function of time corresponding to the T_c crossing during cooldown and warmup is shown in (c) and (d). The first purple vertical line in all four plots represents the time stamp at which T_c is crossed during cooldown. The second purple vertical line represents the time in which T_c is crossed during the followed warmup. (a) and (c) show data of TR 1 whereas (b) and (d) show data of TR 2.

Additionally in figure 10 a further warmup following at a later time is shown. This repeated transition through T_c during warmup (F) causes the previously measured ΔB_{ext} to decline back to its original background state. This supports the theory of ΔB_{ext} to be the magnetic field trapped in the cavity in its superconducting state. This

trapped field is expected to disappear once the cavity transitions from its superconducting (SC) state to its normal conducting (NC) state. This happens due to the characteristic of a superconductor of expelling the magnetic flux outside of the material surface. When the material is in its NC state, magnetic flux is expected to fully penetrate the material again.

The magnetic field data are measured along each axis in both the positive and negative directions. This is due to the sensor being placed in the centre point of the Helmholtz coil, leading to a negative measured field in the one direction and a positive measured field in the other direction. The time scales on the magnetic field plots and on the temperature plots are irrelevant because they only describe the test procedure of different test runs which happened at different times.

The external magnetic field was applied only during the cooldown procedure and removed before the magnetic field test. The magnetic field tests taken at 2 K after cooldown for TR 1 and TR 2 are presented in figure 11. These data are a magnified segment of magnetic field data in figure 10 after the external field had been removed.

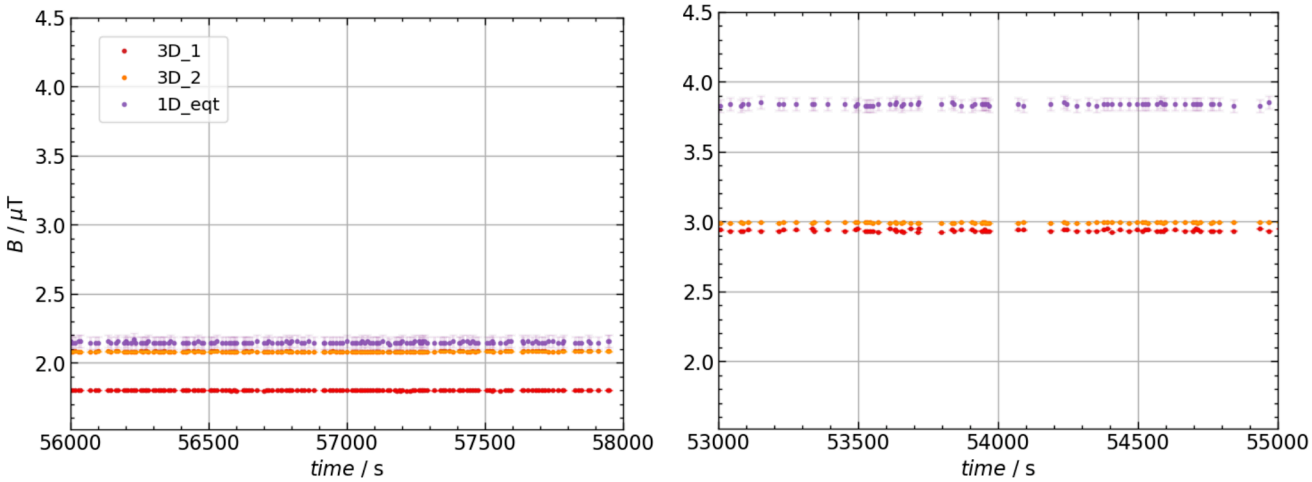

(a) (b)

Figure 11: Comparison of magnetic measurements as a function of time at 2 K. The external magnetic field B_{ext} of 10 µT is applied during T_c of TR 1 (a) and TR 2 (b) of cavity 1DE9. The external magnetic field was removed before taking the data of both tests in (a) and in (b).

For all tests, data were also taken for the two single-axis sensors $1D_{top}$ and $1D_{bot}$ located at the upper and lower beam pipe of the single-cell cavity. The magnetic field data measured by these sensors significantly deviates from the magnetic field data on the equator due to their very different spatial positions and are therefore not further discussed.

Variations between sensor signals are observed in magnetic field tests of all cavities and in all data. Reasons could be due to different temperature gradients during T_c transition, individual calibration of each sensor or spatial properties of the bulk material of every cavity. The single-axis sensor oftentimes show a larger magnetic field signal than the two three-axis sensors. This difference may be attributed to the reduction of the signal of the three-axis sensors due to the filtering system. Nonetheless, the signal difference between the two three-axis sensors is larger in TR 1 than it is in TR 2. In TR 1 sensor $1D_{eqt}$ is comparable to the data recorded by $3D_2$. In TR 2 the sensor $1D_{eqt}$ is deviating from the two sensors $3D_1$ and $3D_2$. For a more complete overview, more precise ranges and possible causes of signal variations observed in all tests are discussed in section 7.1.2.

Results in figure 11 show differences not only in sensor signal variations, but also a fluctuation of data points. The fluctuation of data points of each sensor is described by the standard deviation characteristic of each sensor type as is discussed in section 5. The uncertainty of approximately 1 nT can mainly not be seen in data due to its low significance.

In Fig 12 the magnetic field is shown as a function of time. The baseline test is comparable between both test runs in both the magnetic field values and variation between sensor signals. The two baseline tests presented were each following the test with the applied external field B_{ext} and a warmup and cooldown procedure to about 30 K lies between the two test runs. These results correspond to the expectation of the background field inside XATC2 with an insert installed of about 0.1 µT as is determined in section 4.1.4. There is no significant difference between the two baseline tests which shows that the measurement conditions remained unchanged.

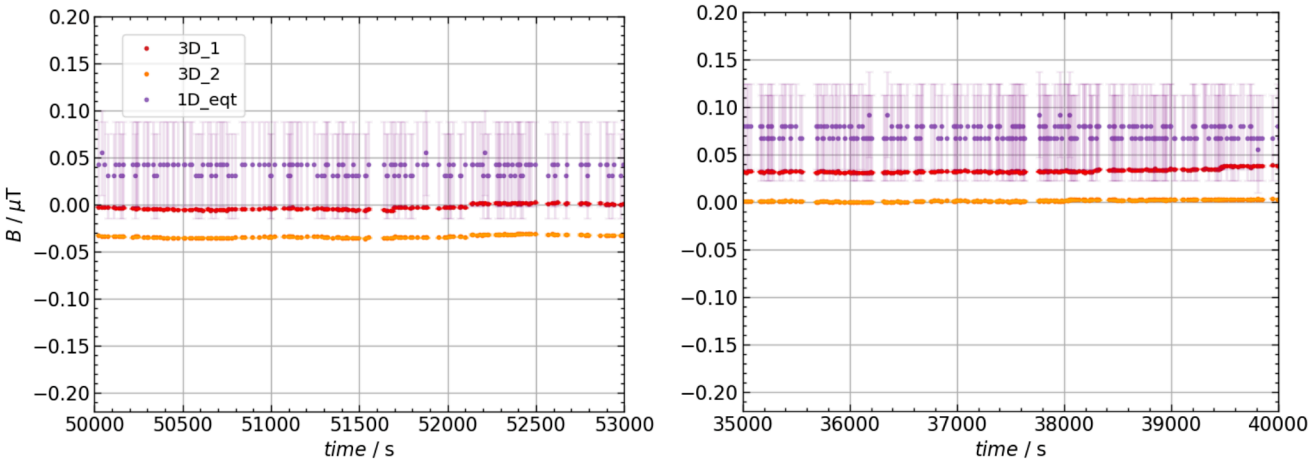

(a) (b)

Figure 12: Comparison between baseline tests for TR 1 (a) and TR 2 (b) of cavity 1DE9. Magnetic field as a function of time. The tests were taken at 2 K with no external field applied during cooldown.

One important figure of merit of the performance of a cavity is the quality factor Q_0. Q_0 is presented as a function of E_{acc} in figure 13 for the tests of cavity 1DE9. The operator generally repeats the $Q_0(E_{acc})$ curve for confirming its validity. In all presented data, only the second taken curve was used for analysis purposes. Data of Q_0 were retrieved for TR 1 and TR 2, each containing one B_{ext} and one baseline test. The expectation for Q_0 for this cavity that was electropolished is a high-field-Q-slope. This high field Q-slope can be seen as a fast drop in the quality factor for TR 1 and TR 2. The high-field-Q-slope disappears when a low-T heat treatment is conducted. This drop happens faster when no external field is applied during the test.

In figure 13, the quality factor of the baseline test of TR 2 (pink filled triangles) is comparable to the baseline results of TR 1 (blue filled circles). The curve for the baseline test of TR 2 (filled pink triangles) lies below the baseline test of TR 2 (filled blue circles). However, Q_0 for TR 2 (blue open circles) with about 10 µT during T_c shows a significant deviation of the curve in TR 1. The temperature gradient during cooldown for both TR 1 and TR 2 is assumed to be the cause of these difference in Q_0. The different temperature gradients of -0.068 [K/s] in TR 1 and -0.024 [K/s] in TR 2 influence the amount of trapped and expelled magnetic flux and thus directly affect Q_0. Cooldown gradients and differences in the external magnetic field ΔB_{ext} are shown in table 4. The cooldown procedure in TR 1 has a larger cooldown gradient than in TR 2. This indicates that the larger temperature gradient causes higher Q_0 values. Thus, a lower temperature gradient causes lower Q_0 values. Data reveals that the influence on Q_0 is only measurable when a strong external field is applied upon the system during T_c transition. Q_0 of the baseline test is not noticeably influenced due to the low ambient magnetic field. [23, p.1201-1202] has shown that larger temperature gradients decrease the amount of trapped flux. This behaviour can be seen in the larger quality factor for the larger cooldown gradient. The larger quality factor signifies less magnetic flux trapping. In [2, p.5] was also measured that large grain cavities trap less flux than fine grain cavities. This is due to the higher diffusion permeability of grain boundaries. That indicates that cavity 1DE9 as a fine grain cavity would generally trap more flux than a large grain cavity with comparable treatment.

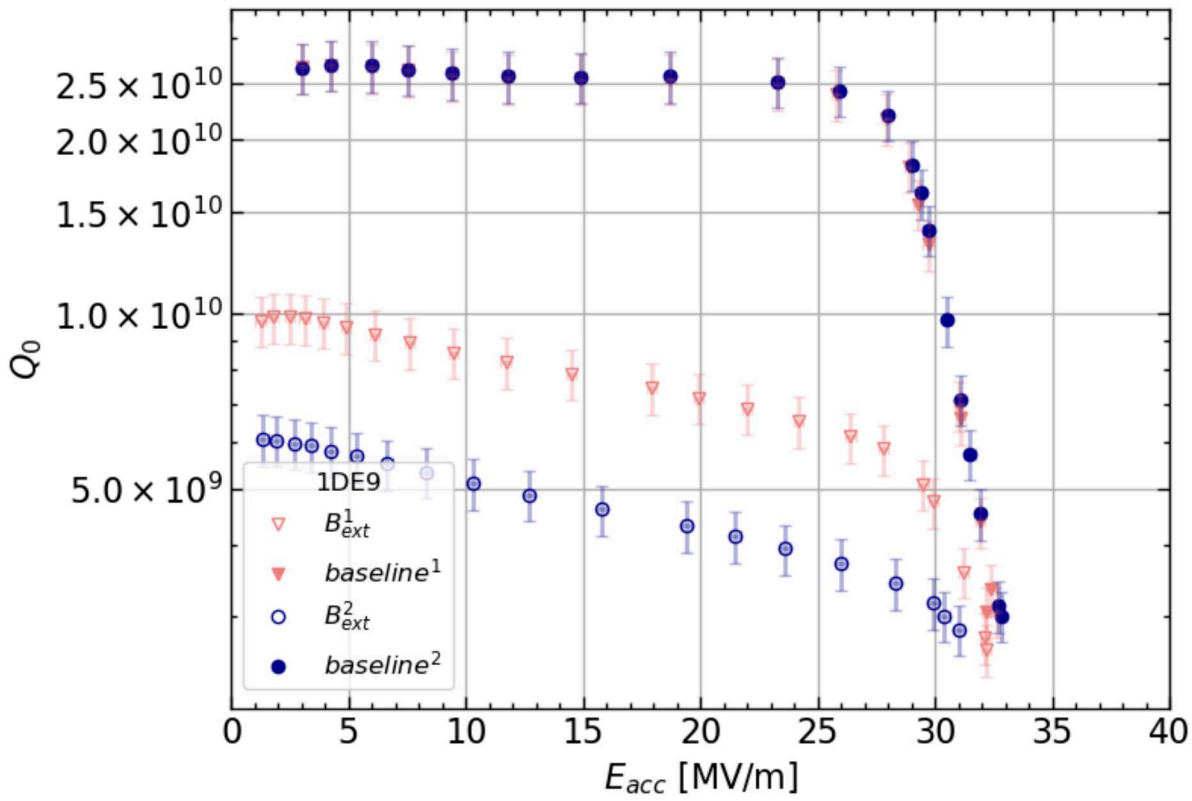

Figure 13: Quality factor Q_0 as a function of the accelerating field E_{acc} of cavity 1DE9 at 2 K. The four different curves of data points are of TR 1 and TR 2 each containing one B_{ext} and one baseline test. The number of the test run is displayed in the superscript of test definitions in the legend.

The calculated surface resistance R_s is based on data in figure 13 and calculated according to equation 2 on page 5. Additionally, ΔR_s is calculated from the difference of the interpolated curves between the surface resistance of the B_{ext} and the baseline tests. All R_s values were interpolated for a common accelerating field in order to compare different R_s as a function of E_{acc} of different tests between each other. The curves for R_s and ΔR_s are shown in figure 14 as an exemplification of the methodology and is not show again in ensuing sections.

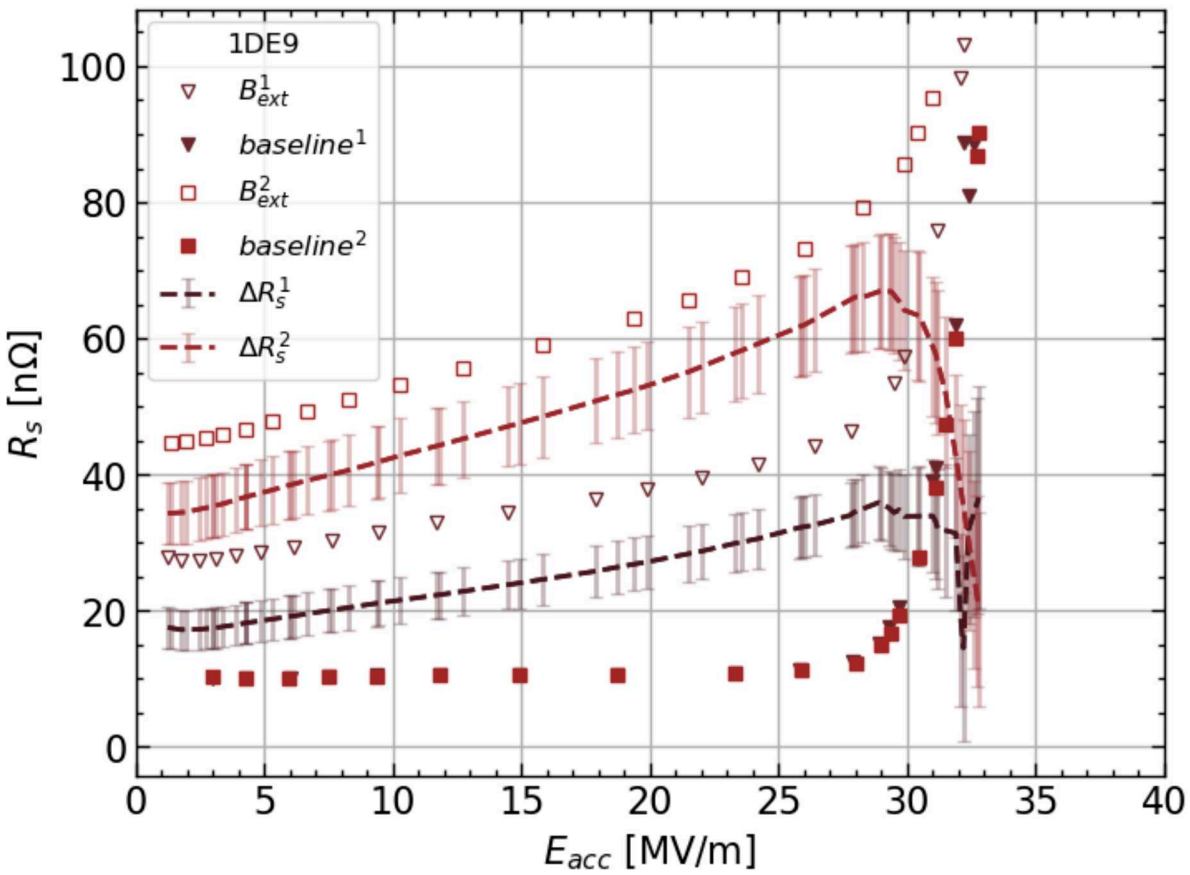

Figure 14: Surface resistance R_s of cavity 1DE9 as a function of E_{acc} of TR 1 and TR 2. The superscript number distinguishes between TR 1 and TR 2. ΔR_s is the calculated difference between the interpolated R_s curves of the B_{ext} and the baseline test of the corresponding test run.

To calculate the sensitivity of cavity 1DE9, difference in magnetic field ΔB_{ext} of each cooldown with the applied external magnetic field is required. Therefore, ΔB_{ext} of TR 1 and TR 2 are presented in table 4. Due to the absence of sensor re-calibration, it is not possible to determine with certainty which sensor provides the more reliable signal within the varying magnetic signals between the different sensors. The standard deviation σ_{3D} of the three-axis sensor signal is lower than of the single-axis sensor. For all ΔB_{ext} determinations, the sensor $3D_2$ is used.

Table 4: Difference in magnetic field (ΔB_{ext}) and calculated temperature gradients during cooldown for TR 1 and TR 2 of cavity 1DE9.

Parameter	TR 1	TR 2
ΔB_{ext} [μT]	1.73	2.95
$\Delta T/\Delta t$ [K/s]	-0.068	-0.024
ΔK [K]	10.3	4.9

Trapped magnetic flux is expected to be higher at the presence of more grain boundaries. The ΔB_{ext} is not as high for cavity 1DE9 as it is for cavity 1DE19 or cavity 1RI02, which are also made of fine-grain niobium. These differences can be attributed to the different cavity treatments. 1DE9 was only electropolished whereas the other three cavities within this work have received mid-T heat treatments.

To calculate the sensitivity, ΔB_{ext} and the ΔR_s function for each test run are inserted in equation 5 on page 6 and results in data presented in the following figure.

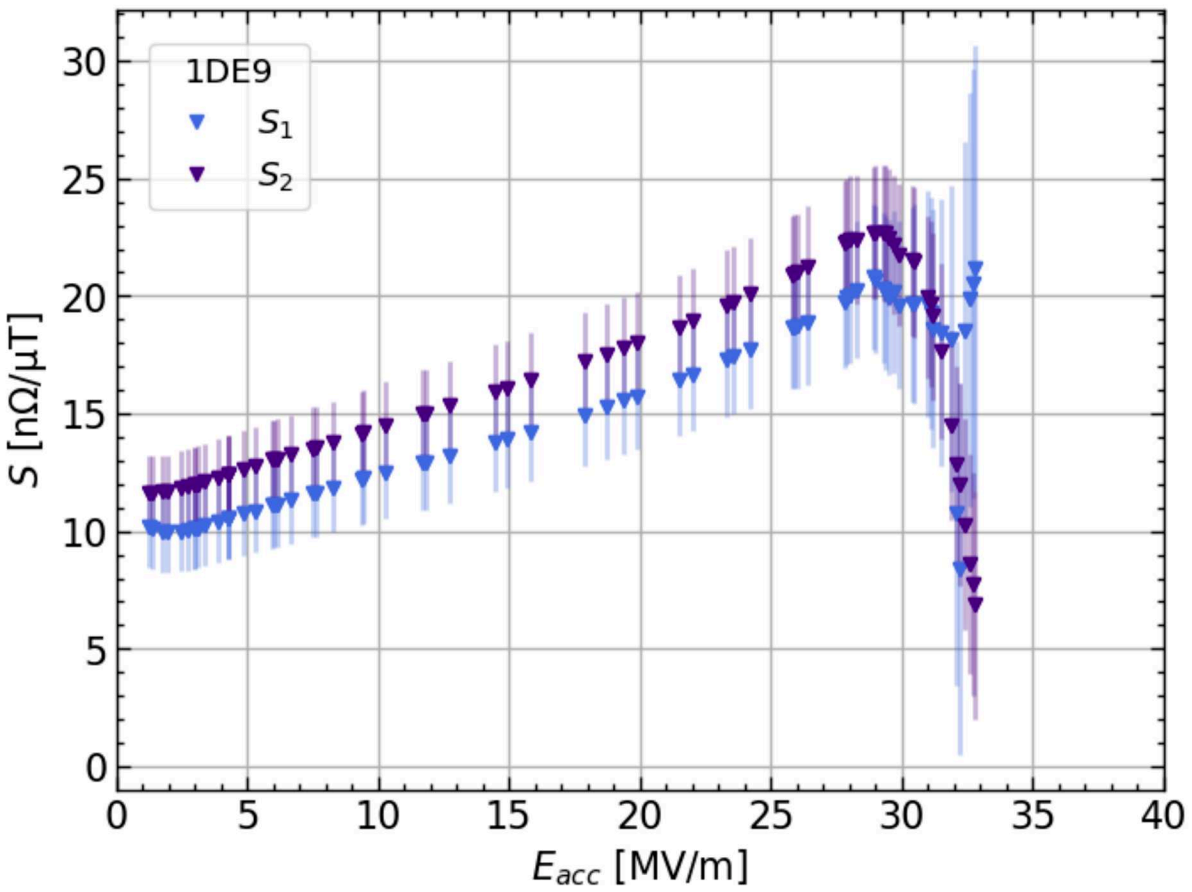

Figure 15: Sensitivity S as a function of the accelerating field E_{acc} of TR 1 and TR 2 of cavity 1DE9.

The sensitivity of TR 1 and TR 2 show different values as is also the case for the quality factors of the corresponding test runs. The larger temperature gradient in TR 1 results in lower sensitivity, whereas the lower temperature gradient in TR 2 results in higher sensitivity values. The S curve of 1DE9 gradually increases with increasing E_{acc} until it reaches a maximum point, where the expected high-field-Q-slope can be seen at about 27 MV/m.

6.2 Fine Grain Cavity with Mid-T Heat Treatment

Cavity 1DE19, manufactured from Ningxia fine-grain niobium from 2005, has undergone a medium-temperature heat treatment at 335°C for about 4.5 hours. For cavity 1DE19 only one test run (TR 1), consisting of one B_{ext} and one baseline test, was performed.

The magnetic field as a function of time during cooldown and T_c transition is presented in figure 16. The abrupt change in magnetic field from the background field of about 0 μT to about 8-10 μT for the different sensor signals shows the application of the external magnetic field B_{ext}. After the removal of B_{ext} from the system induced by the Helmholtz coil, the magnetic field returns to the background field and shows an additional change in the magnetic signal to about 4 μT. The purple vertical line represents the transition of T_c. During this test run, the temperature was first cooled down to about 4 K but then warmed up again to slightly above T_c. Afterwards it was cooled down to 4 K again. The reason for this is unknown. This explains the two purple vertical lines within the relatively low time difference on the x axis. Only a small change in field is observed at the time of the first T_c transition for this cavity. At the second transition of T_c this change in magnetic field is reversed again. This reversal is seen with the second purple vertical line. The field is expected to return to its previous state when transitioning through T_c during warmup but not during another cooldown, as it is the case in this test run. After the second cooldown

described by the second vertical purple line, the magnetic field does not show a larger signal but the same signal as when above T_c. The reason for the magnetic field not remaining in its changed level when below T_c is not clear but could be due to the double transition of T_c within a very short time.

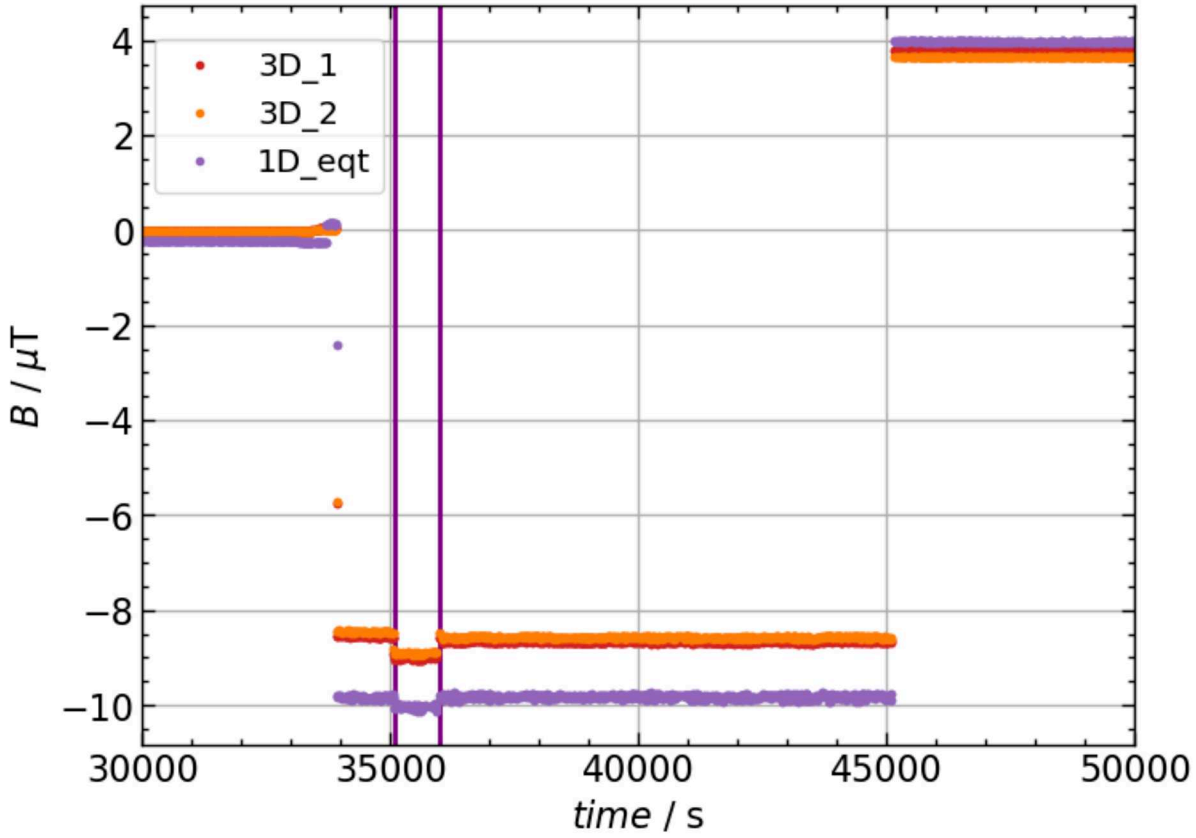

Figure 16: Magnetic field as a function of temperature during cooldown. Data was taken during cooldown from about 30 K to 4 K. The two purple vertical lines present the time of T_c transition. The magnetic field B_{ext} of 10 μ was applied at about 34000 s and removed at about 45000 s.

Figure 16 shows that, after removing the external field B_{ext} from the system, the measured field difference ΔB_{ext} is 3.82 μT. This suggests that a relatively high magnitude of magnetic field is trapped when transitioning into the SC state during the second cooldown (second purple vertical line). This assumingly high flux trapping may be a possible explanation of the low field expulsion during T_c.

The measurements taken at 2 K with an external field B_{ext} during T_c transition are presented in figure 17. These magnetic field signals are a segment of data in figure 16 after the external field was removed from the system. All three sensors measure a magnetic field of about 3.8 μT with a deviation of about 0.2 μT for the different sensor signals. These measured magnetic signals at 2 K support results presented in figure 16 where ΔB_{ext} is 3.824 μT.

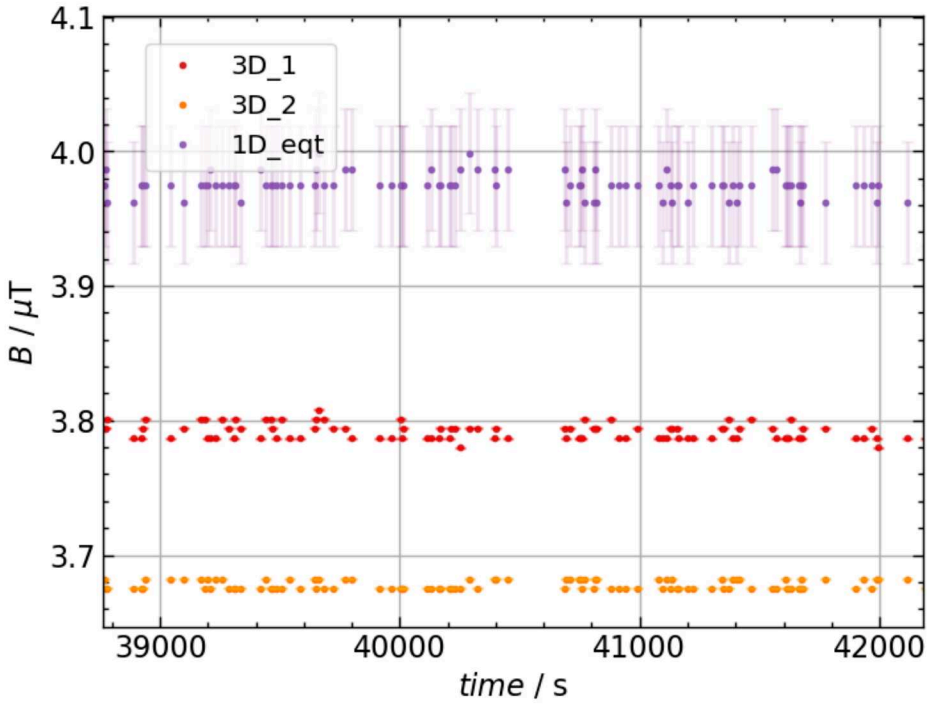

Figure 17: Magnetic field as a function of time with B_{ext} of 10 μ applied during cooldown of cavity 1DE19. Data was taken at 2 K after the removal of the external magnetic field.

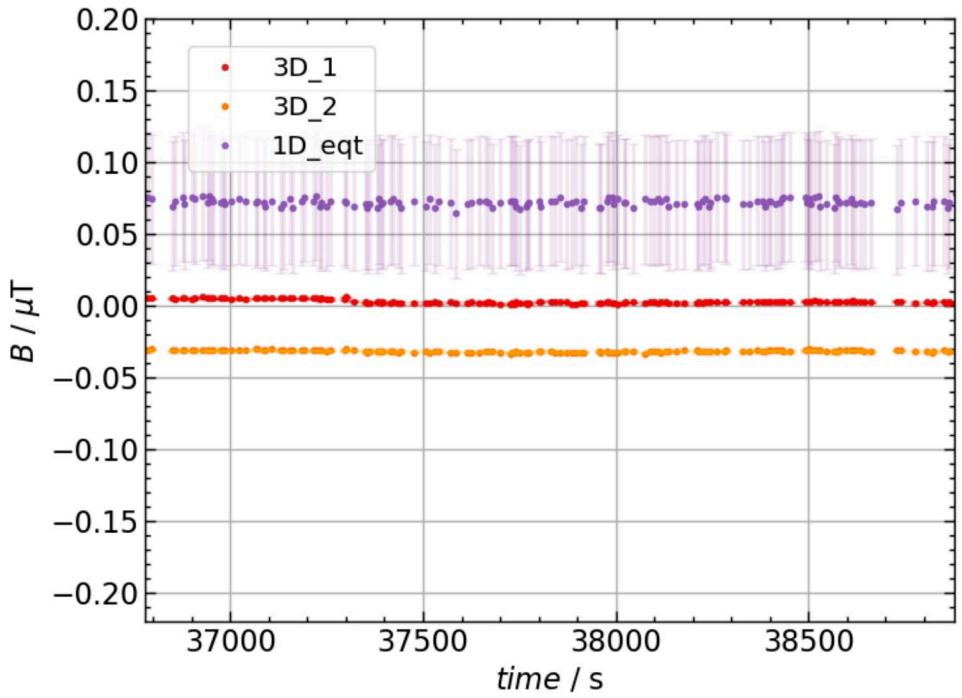

Figure 18: Baseline test for magnetic field as a function of time at 2 K of cavity 1DE19. Data were taken without an external field B_{ext} during cooldown.

Additionally, the baseline test of cavity 1DE19 is presented in figure 18. During this test no external field was

applied and therefore only the background field in the cryostat was measured. The baseline test followed the test with the external field applied during cooldown. The magnetic field measured within the baseline test aligns with the expected background field of about 0.1 µ. This shows that the test conditions remained unchanged. Next, the quality factor Q_0 is presented in figure 19 of cavity 1DE19.

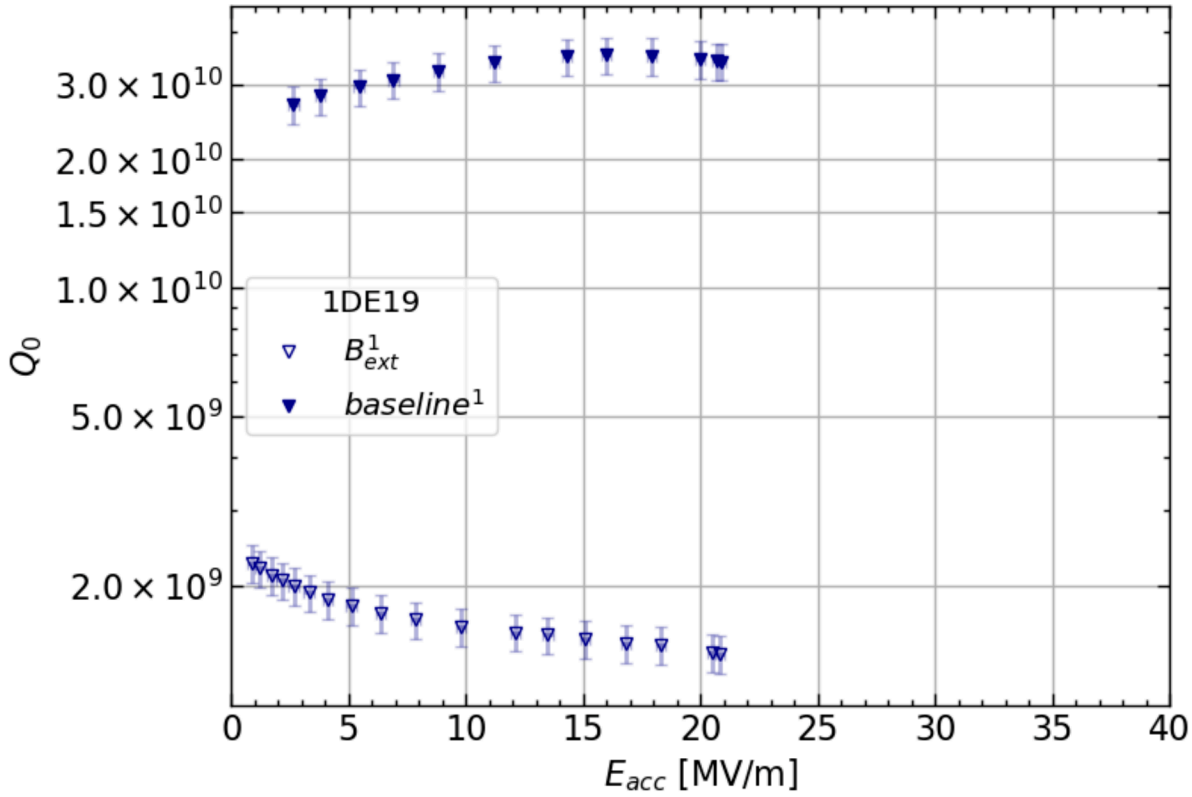

Figure 19: Quality factor Q_0 as a function of the accelerating field E_{acc} at 2 K for TR 1

The quality factor in figure 19 behaves differently than for cavity 1DE9 due to its different cavity treatment. Also, the thermal breakdown of the cavity is observed at low accelerating fields of about 20 MV/m. There is a difference in the trend that the quality factor follows at higher E_{acc}. When B_{ext} is applied Q_0 gradually decreases. In contrast, for the baseline test a slight increase of Q_0 is observed. Both of the Q_0 curves show a completely different shape and quench at relatively low accelerating gradients of about 21 MV/m. The reason for the opposite divergence of Q_0 with higher E_{acc} when comparing the B_{ext} and baseline test is not clear. This divergence in Q_0 for comparable E_{acc} behaves also different than of the other tested cavities within this work. As expected, the quality factor of this cavity does not show a high field Q-slope after undergoing a mid-T heat treatment. The gradual change of the quality factor describes an anti-Q slope.

The temperature gradients and the difference in magnetic field ΔB_{ext} is presented in the following table. Because only one test run was conducted, there is no comparison for another test run of the same cavity 1DE19.

Table 5: Difference in magnetic field (ΔB_{ext}), cooldown gradient, and spatial temperature gradient for TR 1 of cavity 1DE19.

Parameter	TR 1
ΔB_{ext} [µT]	3.82
$\Delta T/\Delta t$ [K/s]	-0.047
ΔK [K]	5.1

The relatively high value of ΔB_{ext} matches with the fine-grain niobium material and the mid-T heat treatment

of cavity 1DE19. Fine grain niobium is expected to cause a higher amount of trapped magnetic flux than large grain cavities. Cavity 1DE19 has the highest ΔB_{ext} among the fine-grain niobium cavities 1DE9, 1DE19 and 1RI02 within this work. The different cavity treatments may have an influence on the variable of ΔB_{ext}. Cavity 1DE19 has undergone a 4.5 hour mid-T heat treatment at 335 °C. The mid-T heat treatments of the other mid-T heat treated cavities within this work are of different temperature and different duration. The corresponding sensitivity values are presented in the following figure.

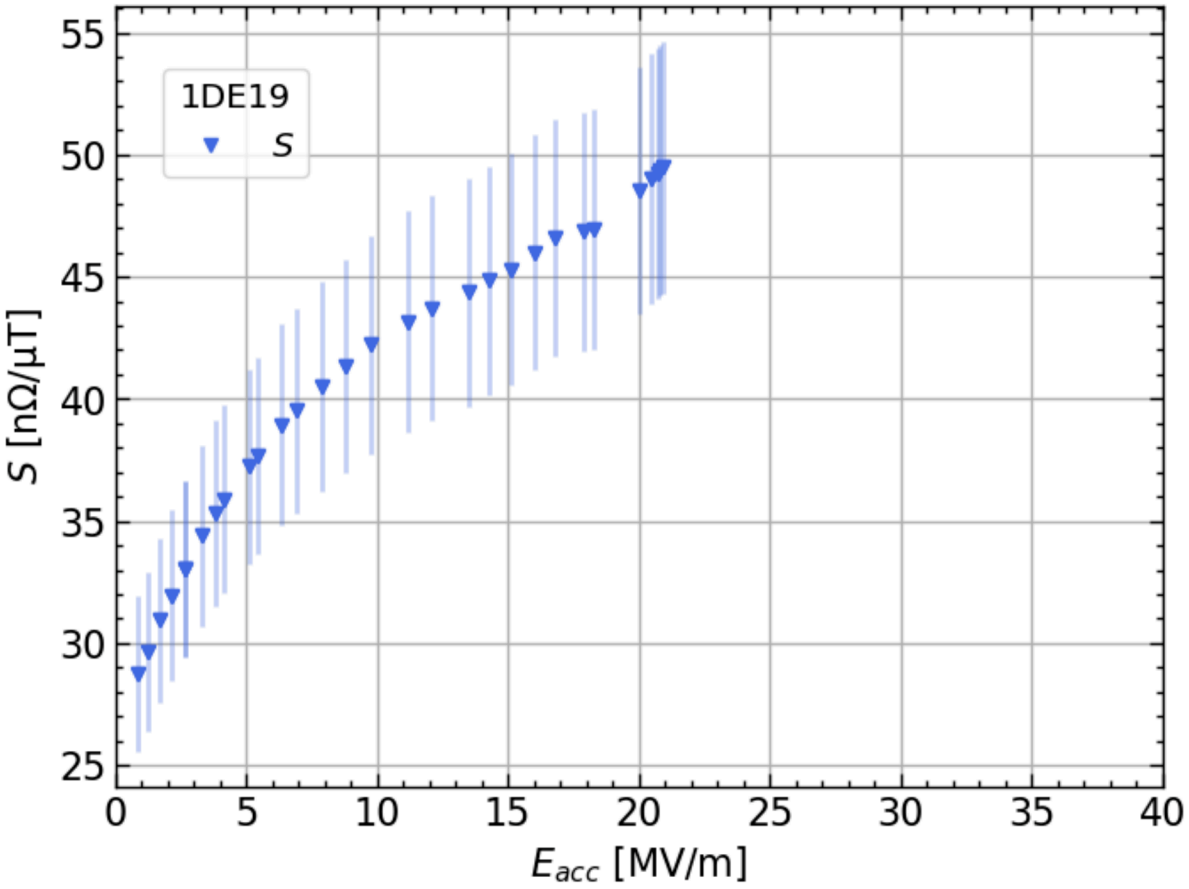

Figure 20: Sensitivity S as a function of the accelerating field E_{acc} of cavity 1DE19.

The higher sensitivity curve in figure 20 is expected considering the larger ΔB_{ext} of this cavity. In other words, higher values of ΔB_{ext} increase the values of sensitivity. The sensitivity curve increases steadily until it slightly flattens around 12.5 MV/m. It terminates near 20 MV/m due to thermal breakdown of this cavity.

6.3 Single Crystal Cavity with Mid-T and Low-T Heat Treatment

Cavity 1AC8 was subjected to a medium-temperature heat treatment consisting of 3 hours at 350°C and an additional low-T heat treatment at 130°C for 24 hours. Cavity 1AC8 is made of single-crystal niobium. This means that the crystal structure of niobium was stretched into one large crystal with the complete absence of grain boundaries. The absence of grain boundaries leads to the expectation of less trapped magnetic flux. It is known that grain boundaries serve as higher diffusivity parts of magnetic flux [2, p.5]. Two test runs TR 1 and TR 2 were performed for this cavity. Due to uncertain data distributions regarding the difference of the magnetic field ΔB_{ext} of TR 2, results of TR 2 are not used for sensitivity determination. Despite the unclear relationship of the notably low ΔB_{ext} in TR 2, data are presented briefly alongside all data of TR 1.

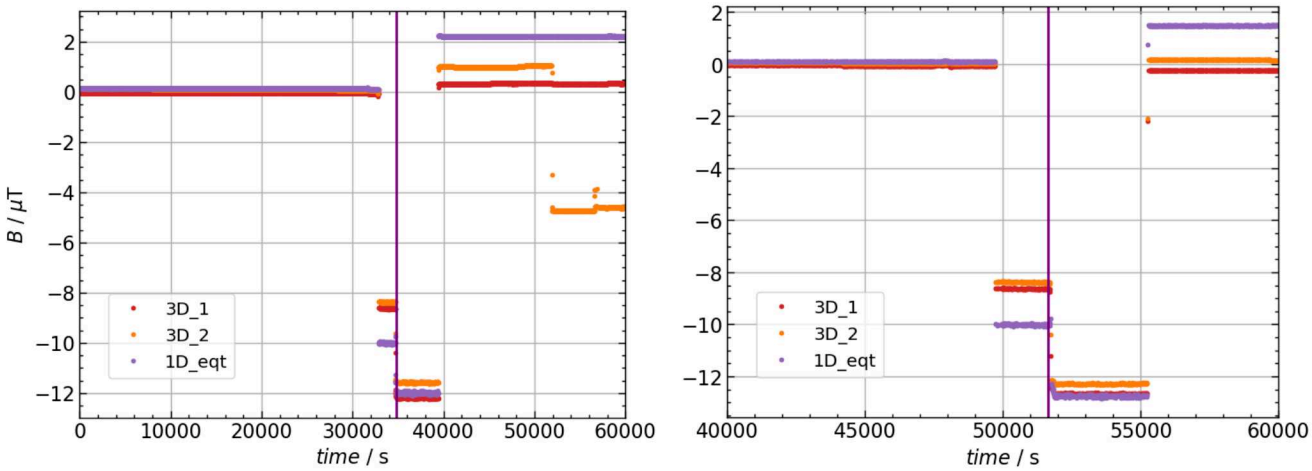

Figure 21: Magnetic field as a function of time. Application of an external field B_{ext} of 10 μT during cooldown from about 30 K to 2 K of cavity 1AC8. (a) and (b) compare magnetic flux behaviour during T_c transition between TR 1 and TR 2. The purple vertical line represents the time at which T_c is crossed during cooldown.

First, the transition of T_c, leading to magnetic flux expulsion and trapping behaviour, is shown in figure 21 for TR 1 and TR 2. For this cavity 1AC8, TR 2 shows a significantly lower ΔB_{ext} measured by the three-axis sensors. During the scope of this work, the cause of this deviation from all other ΔB_{ext} measured by the same sensors could not be determined. The sensor $3D_2$ measures a ΔB_{ext} of about 0.15 μT. Due to the unclear origin of this low value of 0.15 μT, the result is not considered for further calculation in this work. Nonetheless, ΔB_{ext} of TR 1 is comparable to ΔB_{ext} of the other cavities in this work. The values of ΔB_{ext} are presented in table 6 on page 35.

Cavity 1AC8 shows a unique difference in its magnetic field behaviour compared to the other tested cavities. After cooldown to 2 K, a sudden shift in magnetic field of of TR 1 is measured by the sensor $3D_2$ (orange) at around 50000 s. The same signal shift was also observed for TR 2 but can not be seen in figure 21 (b) because 2 K was reached in a different dataset. No warmup, cooldown or any other procedure was performed around this time of the signal shift. The cavity was at 2 K already before this sudden shift in the signal occcured. This sudden shift leads to a greater divergence between the sensor signal that cannot be explained yet. The 2 K test is normally taken at the same timestamps as the quality factor test. Due to this abnormality between the sensor signal by $3D_2$, the magnetic field data and corresponding variations between the sensor signal in the following figure 22 are taken at an earlier time range of, at which the cavity was also at 2 K. The magnetic field data of this range has a significantly lower divergence in the signals of the sensors but is still higher than the signal divergence in the other cavity tests. The signal variations between different cavity tests are discussed in section 7.1.2.

The magnetic field test at 2 K with an external field applied during cooldown is shown in the following figure 22. The two plots show magnetic field data, different from the other cavity tests within this work, of the same test run. Figure 22 (a) shows the divergence of the sensor signals after removing the external field from the system and shows magnetic field data between the time stamps at 2 K before the shift in sensor signal. Figure 22 (b) shows the magnetic field data after the sudden shift in the sensor signal measured by $3D_2$. The two magnetic field plots are two different segments of figure 21 (a). A similar behaviour of a sudden shift in the sensor signal of $3D_2$ is observed in TR 2 but not visually presented here.

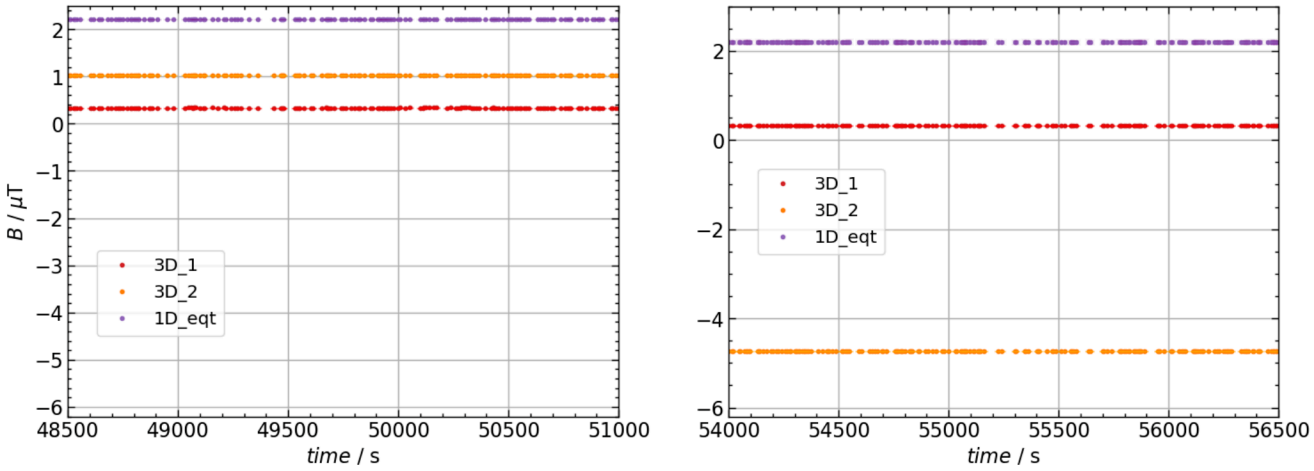

(a) (b)

Figure 22: Magnetic field as a function of time with B_{ext} of 10 μT applied during cooldown of TR 1 of cavity 1AC8 both taken at different timestamps at 2 K. The external field was removed before the magnetic tests at 2 K. (a) and (b) show magnetic field data of the same test run but at different times. A change in the sensor signal causes the differences in the signal between (a) and (b).

The overall order of the magnetic field is lower at this cavity 1AC8 than it is of 1DE9, 1DE19 or 1RI02. This can be correlated to the different material properties in single-crystal niobium. The absence of grain boundaries is likely to cause a lower amount of flux trapping [2, p.5].

The baseline test of TR 1 of cavity 1AC8 is presented in figure 23. The baseline test is the magnetic field test, where no external magnetic field was applied during cooldown. The baseline test was conducted after the B_{ext} test with the application of an external field during cooldown. The magnetic signals lie within the expected range of the background field in the cryostat.

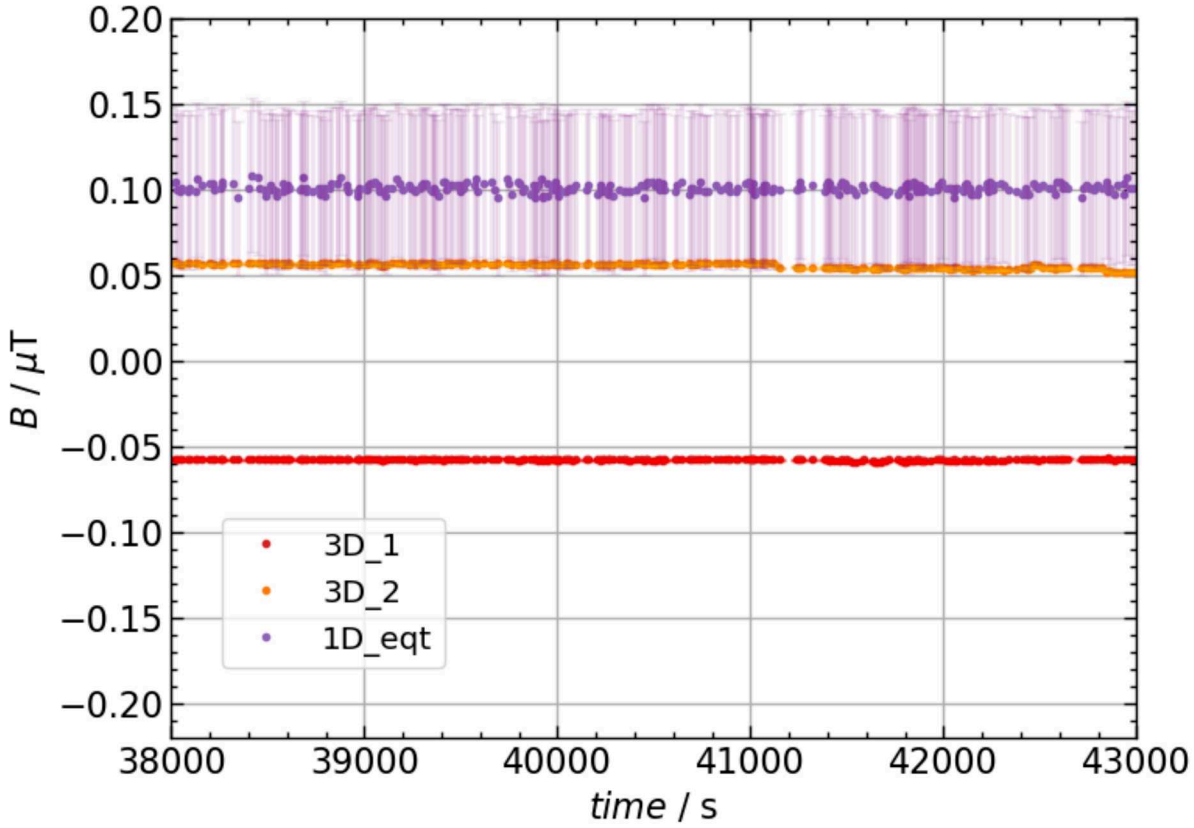

Figure 23: Magnetic field as a function of time of cavity 1AC8 for the baseline test of TR 1. Data were taken at 2 K without an external magnetic field B_{ext} applied during cooldown.

The quality factor Q_0 of TR 1 of 1AC8 is shown in figure 24. In the Q_0 curve can be seen that it does not show a high field Q-slope but decreases gradually with increasing E_{acc}. The Q_0 curve for the B_{ext} test is lower than the Q_0 of the baseline test. The quality factor reaches high accelerating gradients of up to 40 MV/m. These high accelerating gradients are not observed for the other cavities 1DE9, 1DE19 or 1RI02 due to thermal breakdowns at lower E_{acc}. The behaviour of the quality factor curve is comparable to 1DE19 for comparable E_{acc} of up to 20 MV/m. Until 20 MV/m the Q_0 of the baseline test slowly increases and after 20 MV/m it starts to gradually decrease. The trend of the already decreasing Q_0 curve of the B_{ext} test until 20 MV/m continues to decrease even faster at higher E_{acc}. To conclude, the quality factor behaviour of 1DE19 and 1AC8 are similar up to 20 MV/m. At this accelerating field, the quality factor of 1DE19 has a thermal breakdown whereas the quality factor of 1AC8 starts gradually decreasing until 40 MV/m. Cavity 1AC8 is subjected to a mit-T and low-T heat treatment, therefore there is no high field Q-slope seen for the quality factor of this cavity. The high-field-Q-slope would be a fast decrease in quality factor. Despite the different heat treatments of cavity 1AC8 with 350 °C/3 h followed by 130 °C/24 h and cavity 1DE19 with 335 °C/4.5 h, they show similarities in the shape of their quality factors up to 20 MV/m. However, the overall behaviour before and after 20 MV/m deviates from cavity 1DE9, which is only electropolished.

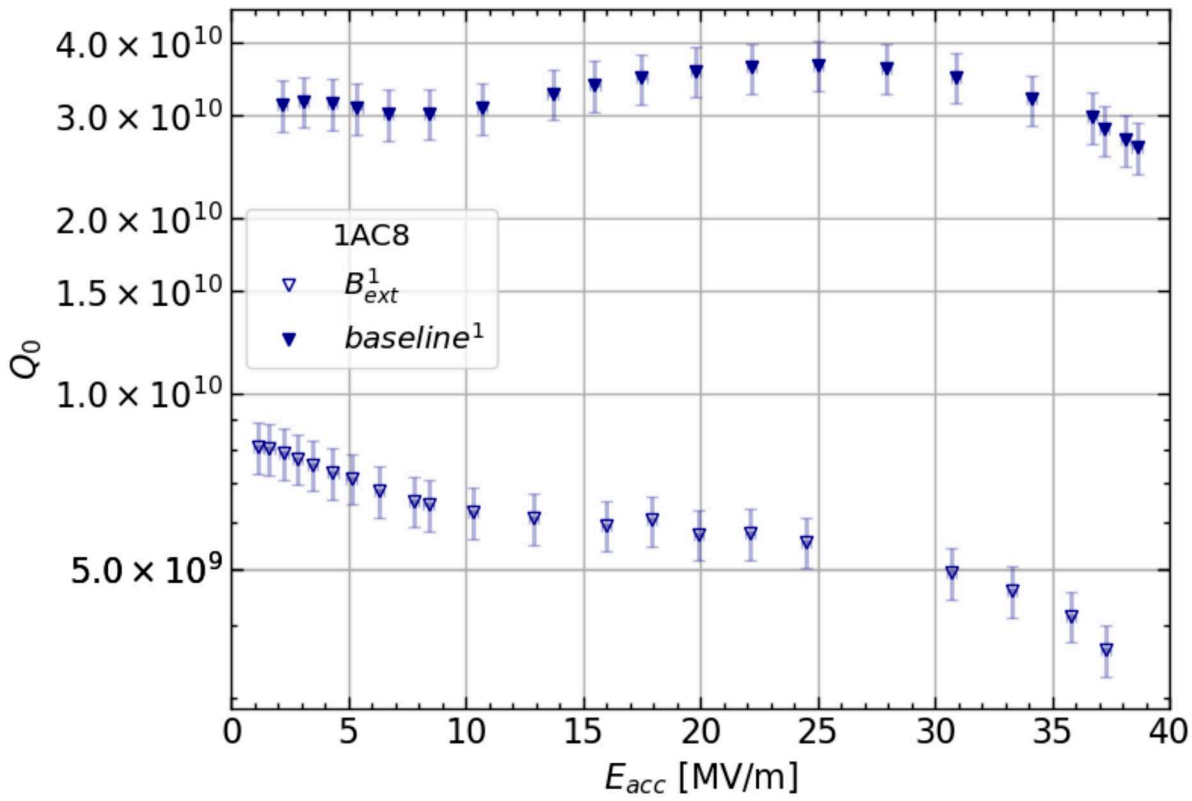

Figure 24: Quality factor Q_0 as a function of the accelerating field E_{acc} of cavity 1AC8 at 2 K for TR 1.

Temperature gradients and ΔB_{ext} are presented in the following table.

Table 6: Difference in magnetic field ΔB_{ext}, cooldown gradient, and spatial temperature gradient for TR 1 of cavity 1AC8.

Parameter	TR 1
ΔB_{ext} [µT]	0.93
$\Delta T/\Delta t$ [K/s]	-0.042
ΔK [K]	6.2

Cavity 1AC8 is made of single-crystal niobium and is therefore characteristic to a complete absence of grain boundaries. This matches with the measured result of the relatively low ΔB_{ext} of 0.93 µT, especially in comparison to the other cavity tests. This value is significantly lower than B_{ext} the other three cavities 1DE9, 1DE19 and 1RI02 within this work, which all three are made of fine-grain niobium.

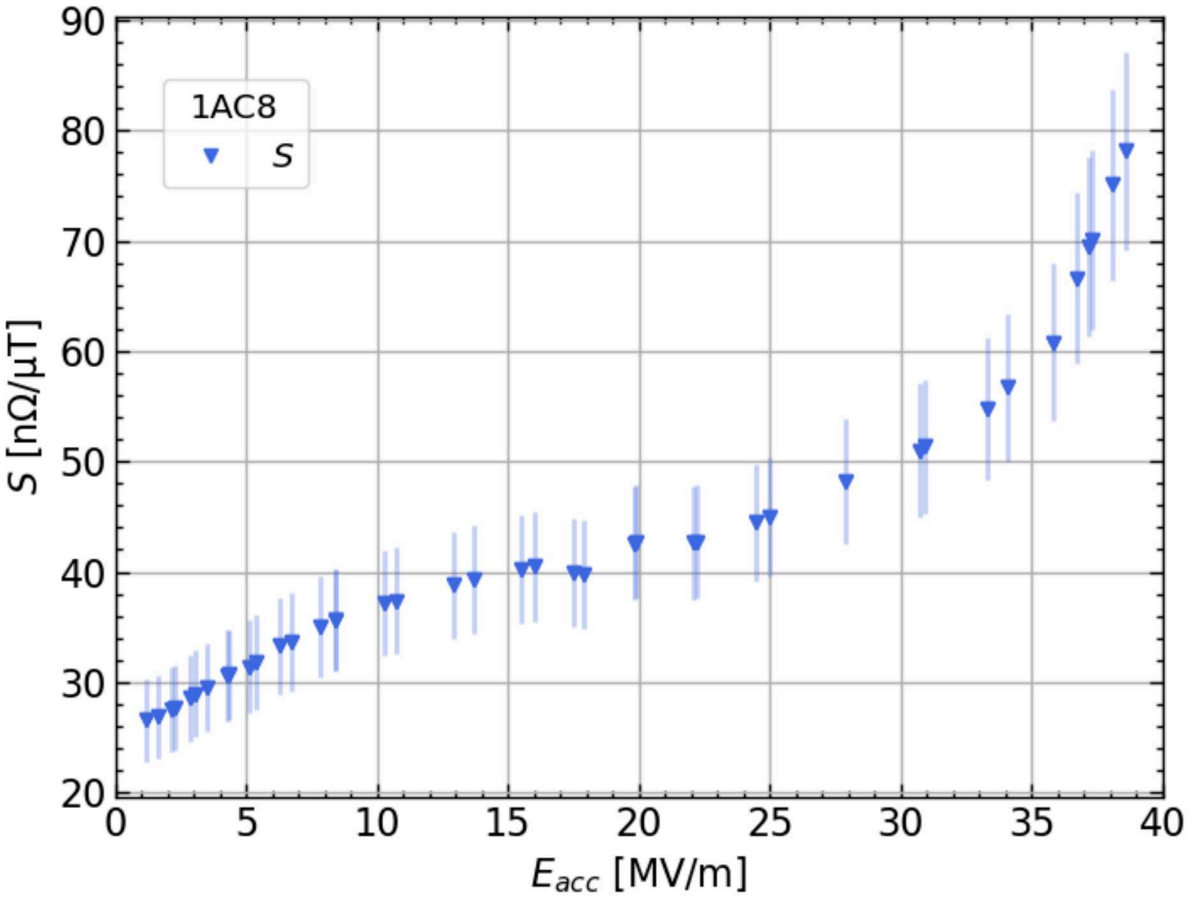

Figure 25: Sensitivity S as a function of the accelerating field E_{acc} of cavity 1AC8.

The values of sensitivity are shown in figure 25. The sensitivity values of this cavity 1AC8 deviate from the sensitivity values of the other three cavities within this work by a factor by about a factor 1.5-3, and may be attributed to the notably lower ΔB_{ext}. The shape of the sensitivity curve is as follows: at low E_{acc} an increase in Q_0 can be seen. The curve flattens out at about 15 MV/m and begins to rise more steeply at approximately 25 MV/m until 40 MV/m.

6.4 Fine Grain Cavity with Long Mid-T Heat Treatment

Cavity 1RI02 is made of fine-grain niobium. Its most recent treatment of cavity 1RI02 is a long mid-T heat treatment at 300°C for 20 hours. This temperature treatment has a considerably longer duration than the other cavities with heat treatments in this project.

For this cavity 1RI02 four test runs were conducted in total. TR 1 and TR 2 were performed with the standard cooldown rate comparable to the cooldown rates of the other cavity tests within this work. TR 3 was performed with a significantly slower cooldown. TR 4 was performed with the standard cooldown rate but with a current applied on the Helmholtz coil of 13 mA instead of 23 mA. This current results in an external magnetic field of about 5 μT instead of 10 μT.

The magnetic field as a function of time during cooldown and T_c transition of 1RI02 is presented for all four test runs in the following figure 26.

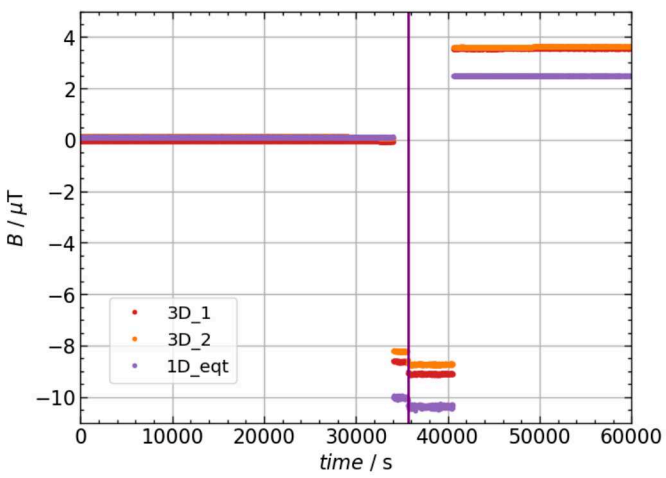

(a) standard cooldown

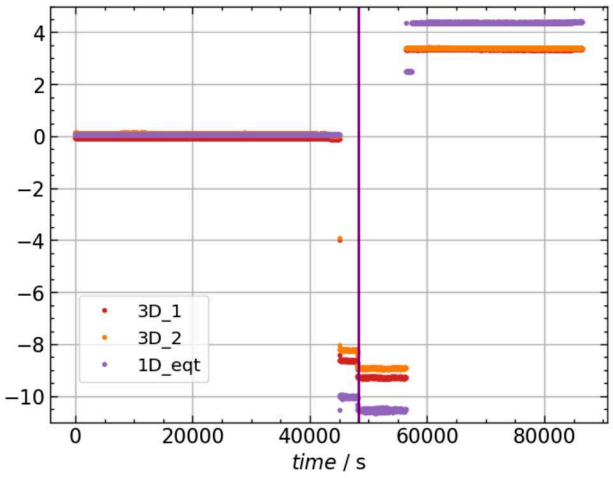

(b) standard cooldown

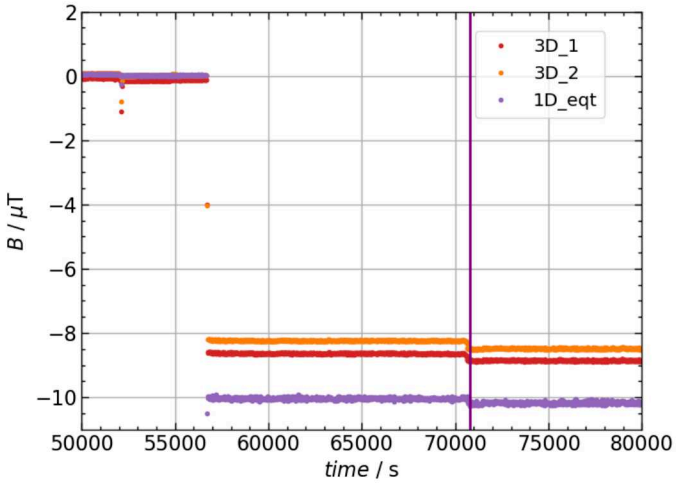

(c) slow cooldown

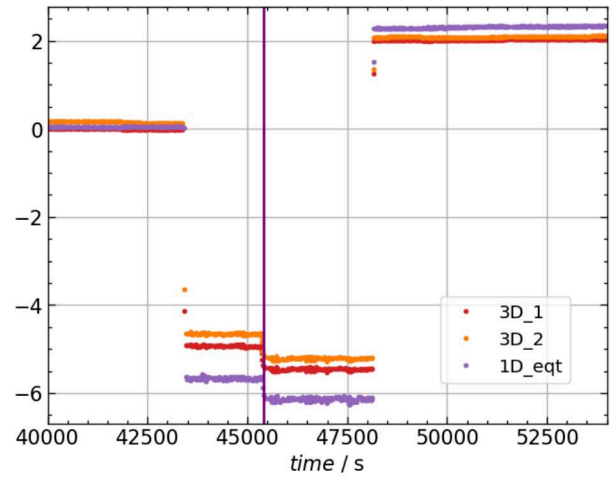

(d) lower B_{ext}

Figure 26: Comparison between TR 1, TR 2, TR 3, and TR 4 of the cooldown procedure and T_c transition of cavity 1RI02. All data were taken over a range of 30 K to 4 K. In (a), (b), and (c) an external magnetic field of 10 µT was applied during cooldown. In (d) an external magnetic field of 5 µT was applied during cooldown. The purple vertical line defines the time of T_c transition.

In figure 26 (c) only the cooldown and application of the external field is presented due to the removal of the external magnetic field being seen in a different data set. The values for determined ΔB_{ext} in TR 3 can therefore not be seen in 26 (c). For all four test runs the following ΔB_{ext} were determined: 3.60 µT for TR 1, 3.40 µT for TR 2. TR 3 is subjected to a slower cooldown with a ΔB_{ext} value of 4.0 µT. TR 4 is subjected to a lower external field with a ΔB_{ext} of 2.0 µT. The ΔB_{ext} is higher for the slow cooldown process and very low for the test with the low magnetic external field. Segments of the magnetic field data of figure 26 at 2 K are shown in the following figure.

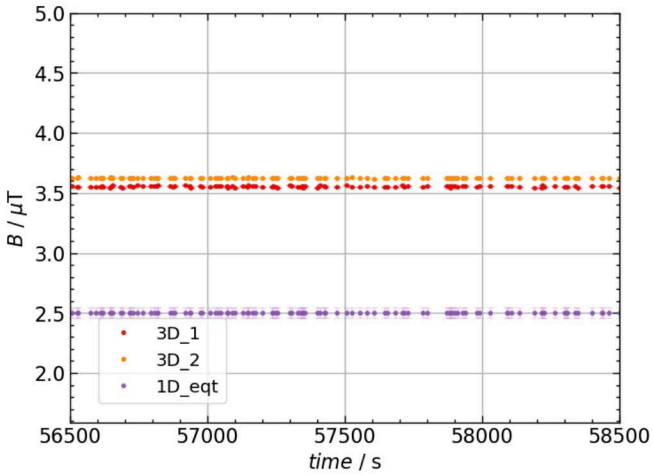

(a) standard cooldown

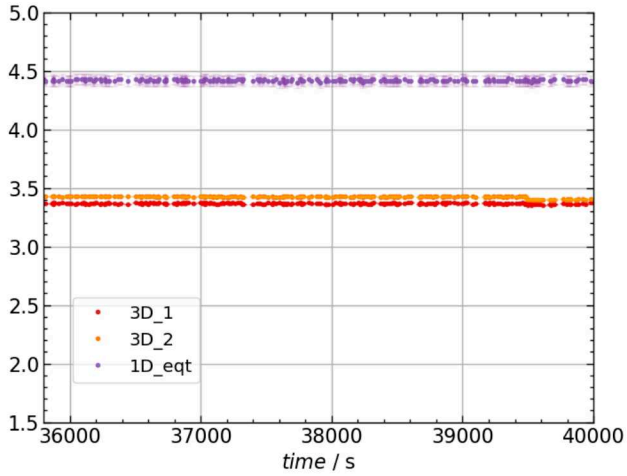

(b) standard cooldown

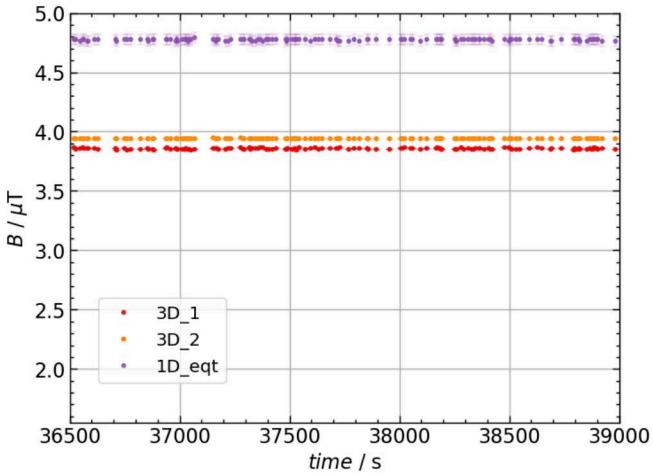

(c) slow cooldown

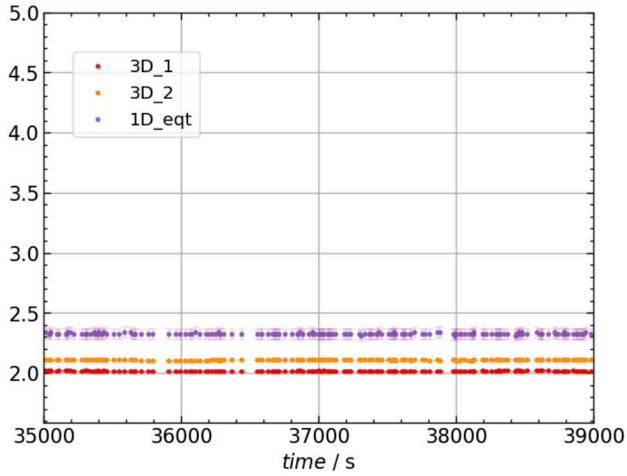

(d) lower B_{ext}

Figure 27: Magnetic field as a function of time for TR 1 (a), TR 2 (b), TR 3 (c) and TR 4 (d). All data were taken at 2 K. For TR 1, TR 2, and TR 3 an external field of 10 μT was applied during cooldown. TR 3 is done with a slower cooldown rate. For TR 4 an external magnetic field of 5 μT was applied during cooldown. The external field was removed before the magnetic tests at 2 K.

Although the variations between the sensor signals are large in figure 26 (a) and (b), both TR 1 and TR 2 show magnetic fields within the expected range of the ΔB_{ext} values in table 7 measured by the sensor $3D_2$. In TR 1 the signal of the single-axis sensor (purple) is lower than of the two three-axis sensors (orange and red). This is different in TR 2, TR 3 and TR 4 and for the magnetic field tests of the other cavities. The reason for this change in the relation of the sensor signals to one another is not clear.

The ΔB_{ext} value with 4 μT of TR 3 with a significantly slower cooldown rate, is slightly larger than for TR 1 and TR 2. However, in TR 4 the lower magnetic field of about 5 μT results in a substantially lower magnetic field of about 2.0-2.5 μT for the different sensor signals at 2 K. These lower magnetic field signals in TR 4 can be seen in figure 27 (d). With the low magnetic field applied in TR 4 the low measured field is expected and also results in a lower ΔB_{ext} value.

The corresponding baseline tests are presented in figure 28. Variations among the sensors in the scale of up to

100 nT can be seen when comparing the baseline tests. This deviation does not occur at the baseline tests of the other cavity tests of 1DE9, 1DE19 and 1AC8 and cannot be explained yet. Although according data has not been analysed for the baseline tests, a possible explanation could be the different temperature gradients during cooldown.

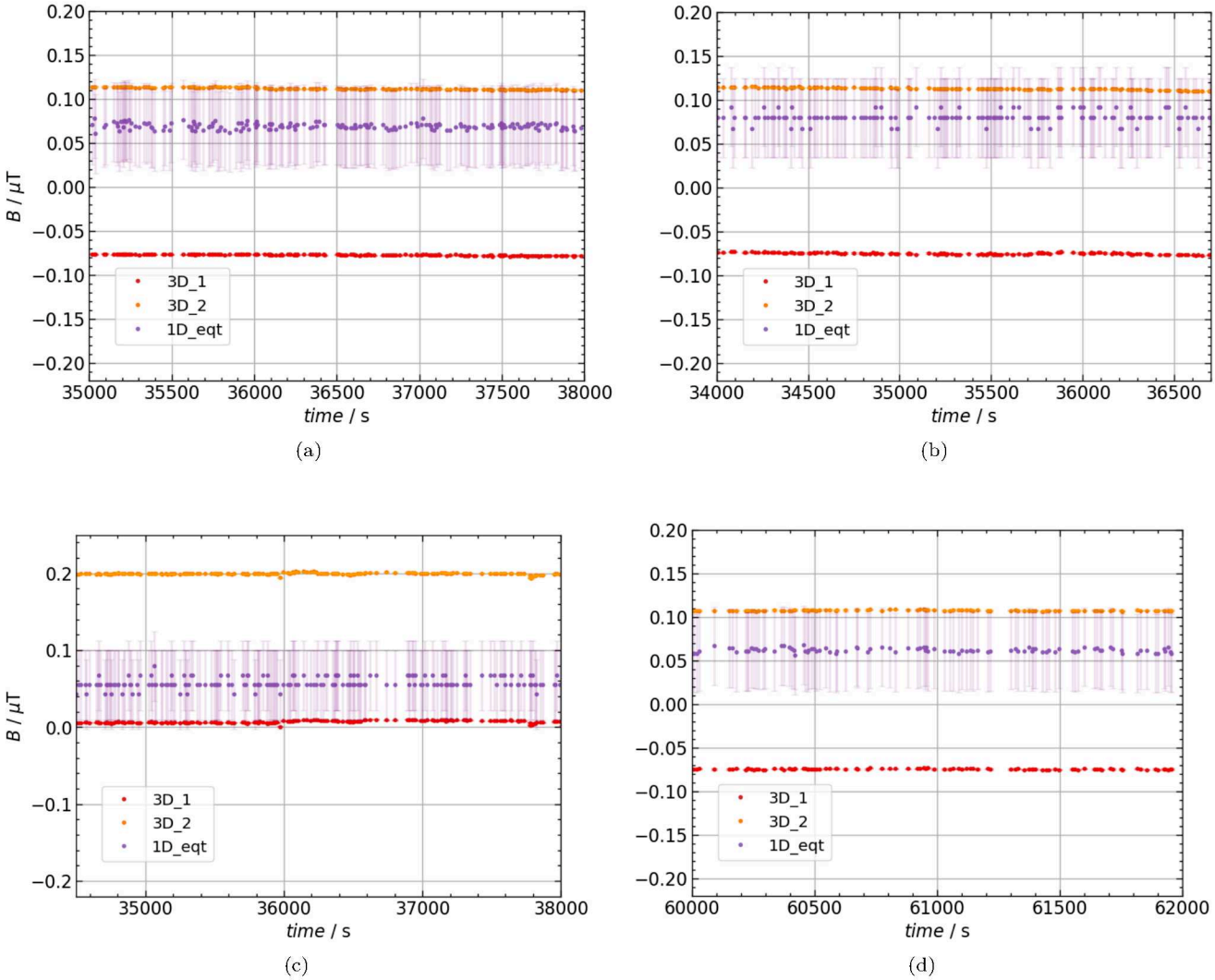

Figure 28: Baseline tests of magnetic field as a function of time for TR 1 (a), TR 2 (b), TR 3 (c), TR 4 (d) of cavity 1RI02. All tests were taken at 2 K no external magnetic field B_{ext} was applied during cooldown.

The quality factors of TR 1, TR 2, TR 3 and TR 4 are presented in figure 29. The similar ΔB_{ext} values observed in TR 1, TR 2, and TR 3 during cooldown indicate comparable magnetic field conditions. The quality factors of these three test runs result in Q_0 curves that closely overlap for the ΔB_{ext} tests. As expected, the quality factor curve of TR 4 with the lower applied external field results in the highest quality factor of this cavity, which approaches more closely to the values of the quality factors of the baseline tests. While the quality factor curves of TR 1, TR 2, and TR 3 start at about $3.0 \cdot 10^{-9}$, the curve of TR 4 starts at about $5.0 \cdot 10^{-9}$. To further investigate the impact of the external field strength, in future studies the external field could be continually lowered by a factor 2 and then evaluated to what extent the quality factor value changes until it approaches the results of the baseline tests.

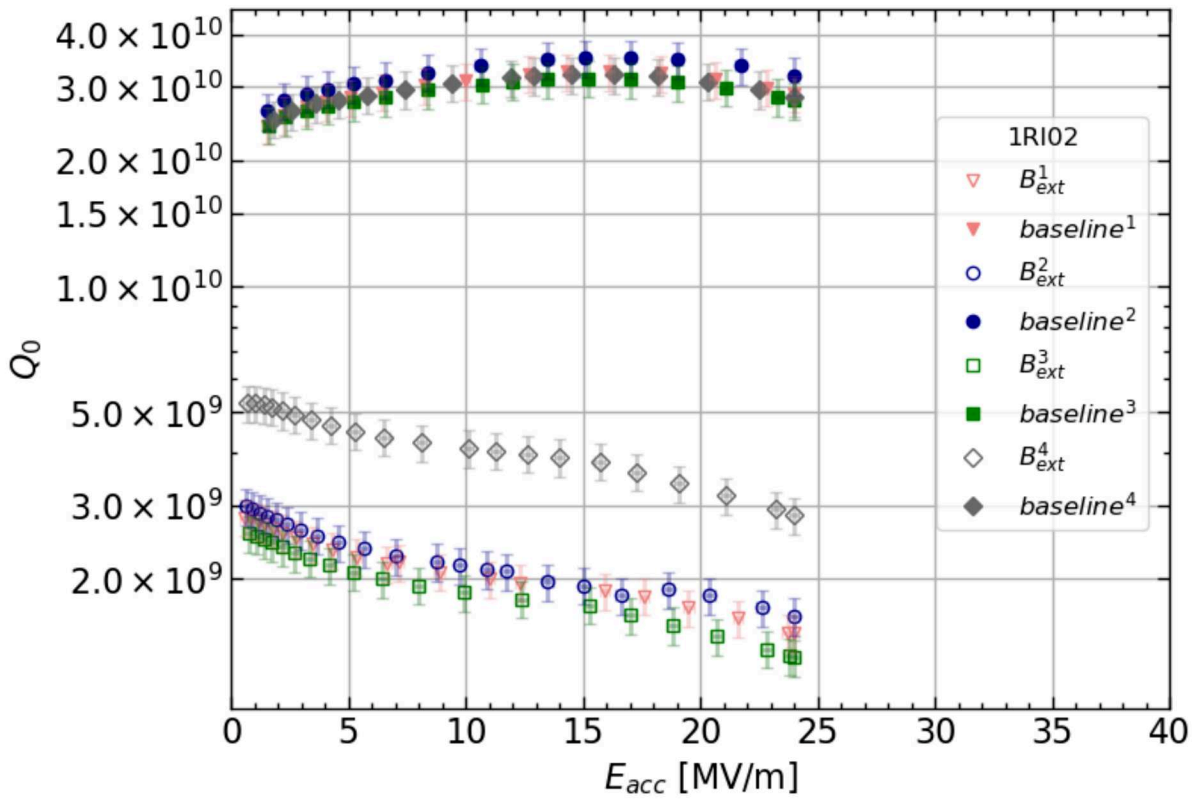

Figure 29: Quality factor Q_0 as a function of E_{acc} of TR 1 - TR 4 of cavity 1RI02 at 2 K.

TR 3 shows a slightly lower quality factor curve than TR 1, which also shows a slightly lower curve than TR 2. This would match the values of ΔB_{ext}. TR 3 has the highest ΔB_{ext} value followed by TR 1 and TR 2. Also, the difference of the ΔB_{ext} between TR 1 and TR 2 is very low and so is the difference between their corresponding Q_0 curves. However, the ΔB_{ext} of TR 3 is a bit higher and also its Q_0 curve is visibly lower. The trend in ΔB_{ext} values for the different test runs also matches with the temperature gradients during cooldown. The lowest temperature gradient leads to the lowest Q_0 curve and the largest temperature gradient to the highest Q_0 curve.

All quality factor curves of the baseline tests closely overlap. Only with a strong external field an impact on the quality factor values can be observed. Comparable to the other three cavities 1DE9, 1DE19, and 1AC8 the quality factor curve increases gradually for the baseline tests and decrease gradually for the B_{ext} tests. The cavity quenches at the low E_{acc} value of nearly 25 MV/m. The early quench could be connected to the 20 hour long mid-T heat treatment.

The according sensitivity values of cavity 1RI02 are shown in the following figure 30. For better presentation of the overlapping error bars in this figure, different colors were chosen for the previously discussed quality factor curves. S_1 (blue) was calculated from the Q_0 curves in pink, S_2 (purple) results from the Q_0 curves in blue, S_3 (green) results from the Q_0 curves in green and S_4 (pink) results from the Q_0 curves in gray. Yet, the sensitivity and quality factor curves are directly comparable by their corresponding number in the legend.

The differences in the sensitivity curves as an inverse function of Q_0 between TR 1 - TR 3 are comparable to their previously discussed quality factor correlations to each other. TR 4 with the lower external field results in the highest quality factor curve and in the lowest sensitivity to magnetic flux. This behaviour is expected when taking into account that a lower external magnetic field causes lower flux trapping than a high external field on the system.

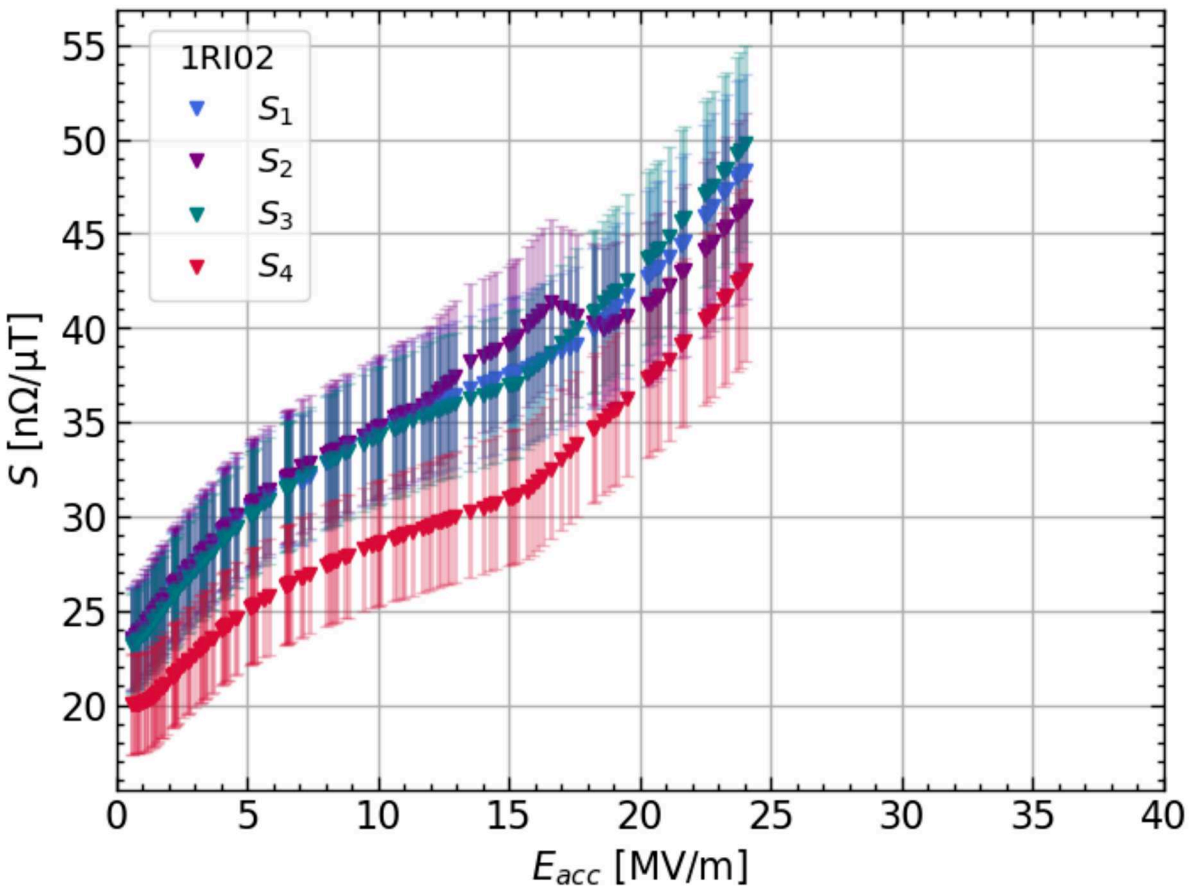

Figure 30: Sensitivity S as a function of the accelerating field E_{acc} for TR 1 - TR 4 of cavity 1RI02.

To conclude for all four cavities, cavity 1DE9 shows sensitivity values of about 10-25 nΩ/μT. Cavity 1DE19 has values of about 30-50 nΩ/μT. Cavity 1AC8 shows significantly higher sensitivity values of around 25-80 nΩ/μT. The sensitivity of cavity 1RI02 has values between 20-50 nΩ/μT.

The temperature gradients and ΔB_{ext} of TR 1, TR 2, TR 3, and TR 4 are presented in the following table.

Table 7: Difference in magnetic field ΔB_{ext}, cooldown gradients, and spatial temperature gradients for cavity 1RI02.

Parameter	TR 1	TR 2	TR 3	TR 4
dT/dt [K/s]	-0.040	-0.017	-0.003	-0.051
ΔK [K]	6.0	7.9	3.4	10.3
ΔB_{ext} [μT]	3.6	3.4	4.0	2.0

7 Comparison of Results

In this section, the variations between sensor signals in the measured magnetic field tests are discussed. Particularly, of the magnetic field tests of all cavities in which an external field is applied during cooldown and removed before starting the test at 2 K. Furthermore, the impact of the different cavity heat treatments and the temperature gradients are correlated to the quality factor and sensitivity of the cavity.

7.1 Variation between Sensor Signal

Firstly, the varying magnetic signals measured by the three different magnetic sensors on the cavity equator are presented in section 7.1.1 and interpreted in section 7.1.2.

7.1.1 Data of Magnetic Signals

The following tables show the differences between the sensor signals for the same test run. All three sensors recording the signal are mounted on the equator of the cavity at different azimuthal locations. These differences can be seen in the magnetic field data of all B_{ext} tests within section 6. The data in the tables show the differences between measured magnetic field signals in the nanotesla scale. The absolute values on the positive and negative axis scale of the sensor signals can be found in the figures of section 6. The signals of sensors $3D_1$, $3D_2$, and $1D_{eqt}$ are presented. All magnetic field data in the tables are approximate values read out from the magnetic field data with resolution in the nanotesla scale.

The following table presents sensor variation data of cavity 1DE9. The range of the signal differences within the magnetic field tests are between 50-850 nT. 1DE9 was electropolished and is made of fine-grain niobium.

Table 8: Comparison of differences between sensor signals during a B_{ext} test of cavity 1DE9.

ΔB_{signal}	TR 1 [nT]	TR 2 [nT]
$\lvert 3D_1 - 3D_2 \rvert$	300	50
$\lvert 3D_1 - 1D_{eqt} \rvert$	350	850
$\lvert 3D_2 - 1D_{eqt} \rvert$	50	800

The following table presents sensor variation data of cavity 1DE19 and is made of fine-grain niobium. The range of the signal differences within the B_{ext} cavity tests lies between 100-300 nT. 1DE19 has a mid-T heat treatment of 335 °C for 4.5 h.

Table 9: Comparison of differences between sensor signals measured during a B_{ext} test of cavity 1DE19.

ΔB_{signal}	TR 1 [nT]
$\lvert 3D_1 - 3D_2 \rvert$	100
$\lvert 3D_1 - 1D_{eqt} \rvert$	200
$\lvert 3D_2 - 1D_{eqt} \rvert$	300

1AC8 has a mid-T heat treatment of 350 °C for 3 h followed by a low-T heat treatment of 130 °C for 24 h and is made of single-crystal niobium. For cavity 1AC8 two different versions of magnetic field data are presented. The reason for that is a sudden shift in the sensor signal after the removal of the external magnetic field and after cooldown to 2 K. At this point, the sensor signal of $3D_2$ shows an abrupt anomaly. This observation is discussed in more detail in section 6.3 in regard to figure 22 (a) and (b).

The difference of the signals among the sensors $3D_1$, $3D_2$, and $1D_{eqt}$ before and after the signal anomaly is shown in the following tables. The signal differences before the anomaly range between 500 - 2000 nT, while after the anomaly the signals change between 1700 - 7000 nT.

Table 10: Comparison of differences in sensor signals during a B_{ext} test of cavity 1AC8, (a) before and (b) after the signal anomaly.

(a) Before the signal anomaly.

ΔB_{signal}	TR 1 [nT]	TR 2 [nT]
$\lvert 3D_1 - 3D_2 \rvert$	750	500
$\lvert 3D_1 - 1D_{eqt} \rvert$	2000	1750
$\lvert 3D_2 - 1D_{eqt} \rvert$	1250	1250

(b) After the signal anomaly.

ΔB_{signal}	TR 1 [nT]	TR 2 [nT]
$\lvert 3D_1 - 3D_2 \rvert$	5000	3000
$\lvert 3D_1 - 1D_{eqt} \rvert$	1700	1700
$\lvert 3D_2 - 1D_{eqt} \rvert$	7000	4500

The following table presents sensor variation data of cavity 1RI02. The range of the signal differences within the B_{ext} cavity tests lies within 100 - 1050 nT. 1RI02 has a long mid-T heat treatment of 300 °C for 20 h and is made of fine-grain niobium.

Table 11: Comparison of differences between sensor signals measured during a B_{ext} test of cavity 1RI02.

ΔB_{signal}	TR 1 [nT]	TR 2 [nT]	TR 3 [nT]	TR 4 [nT]
$\lvert 3D_1 - 3D_2 \rvert$	100	100	100	100
$\lvert 3D_1 - 1D_{eqt} \rvert$	1050	1050	950	350
$\lvert 3D_2 - 1D_{eqt} \rvert$	1150	950	850	250

7.1.2 Discussion of Magnetic Signals

Three different sensors, two three-axis sensors and one single-axis sensor, are placed on the equator of the cavity and are set up to measure the same magnetic field signal. However, the measured signal by the different sensors show a not negligible difference for the same magnetic field test of the same test run. In contrast, considering all baseline tests, in which no external magnetic field is applied during cooldown, it can be seen that the variations between the sensor signals do not change significantly when repeating the same baseline test. The change between the signals lies in the range that was determined for the sensors in the empty cryostat and is presented in section 4.1.4. This low variation is the case for all repeated baseline tests of all measured cavities. The magnetic field signals of the baseline tests can be seen in figures 12, 18, 23, and 28 of section 6. This observation shows that the more significant variations between sensor signals by the three sensors is not present at test conditions without any strong external field and appear only at the tests with a strong magnetic field applied. This is the case for the B_{ext} tests of this work at 10 µT or 5 µT.

The only exception in the baseline tests can be seen at the baseline tests of cavity 1RI02, where the measured field varies between the different baseline tests by about 0.05 - 0.1 nT. This variation can be seen in figure 28 on page 39. Although the reason for this minor variation in the baseline tests is unclear, it could stem from different cooldown rates influencing the flux trapping behaviour even for low magnetic fields. The temperature gradients during cooldown are not determined for the baseline tests but this can be a possible approach for future research. The cooldown gradients for the baseline tests are not determined in consideration of the relatively consistent low change in magnetic field test results of all baseline tests between different vertical tests.

Yet, the variation between magnetic signals after applying an external field is significantly higher as shown in the tables in section 7.1.1. These different signals measured by the three sensors when compared to the baseline tests, indicate that the divergence of the signals stems from the exposure to a strong magnetic field. During a magnetic test with an applied external field during T_c transition, the variations between signals and their relative ordering differ between sensors within the same test run, and also vary between separate test runs. Cavity 1DE9, 1AC8, and 1RI02 each have at least two test runs. Cavity 1DE19 has one test run. Before applying the external field B_{ext} at 30 K, the magnetic field data in each B_{ext} test are comparable and reflect the ambient field inside the cryostat. Thus, when no external magnetic field is present the variations between the sensors behave as in the baseline tests. One exception can be seen for TR 1 of cavity 1DE9 in figure 10 (a), where the single-axis sensors deviate from the two three-axis sensors by about 1000 nT already before the application of B_{ext}. The reason for this variation is not understood and could not be observed for almost any of the other B_{ext} tests conducted within this work. For all other test runs with B_{ext} of cavities 1DE9, 1DE19, 1AC8 and 1RI02 the magnetic signals measured before the application of B_{ext}, deviate only between 0 nT and 225 nT. The signal variations for baseline conditions were already discussed in section 4.1.4 and are thus expected. All magnetic field values recorded by the sensors at about

20 K - 30 K before applying the external field are shown in the following table. The table shows the measured values shortly before the application of an external field. All values are approximated in the nanotesla scale and taken at about 30 K.

Table 12: Comparison of sensor signals measured by $3D_1$, $3D_2$, and $1D_{eqt}$ on the equator of the cavity. The values are taken shortly before the application of the external magnetic field at about 30 K.

Sensor	B_{1DE9} [nT]		B_{1DE19} [nT]	B_{1AC8} [nT]	
	TR 1	TR 2	TR 1	TR 1	TR 2
$3D_1$	45	-25	-40	125	50
$3D_2$	50	0	-20	-40	-50
$1D_{eqt}$	1000	50	-225	125	100

Sensor	B_{1RI02} [nT]			
	TR 1	TR 2	TR 3	TR 4
$3D_1$	100	80	100	175
$3D_2$	-50	-75	-100	0
$1D_{eqt}$	100	75	50	50

In total, the magnetic field data recorded by all three sensors show variations between the sensor signals of the different sensors within the range of 25 - 225 nT. These variations lie within the expected background field of the cryostat as is shown in section 4.1.4. One exception of a deviation of 1000 nT for 1DE9 is observed in TR 1.

The changes in each signal can be observed during specific measurement operations within a single test run. Changes in signals regarding the measured magnetic field occur during the following operations: at the application of B_{ext}, during the transition through the critical temperature T_c, and after the removal of the external field B_{ext} at 4 K. All these operations with their corresponding signal changes are shown in figures 11, 17, 21, and 27 in section 6. The exact differences between each sensor signal in the nanotesla scale are presented in tables 8, 9, 10 and 11 in the previous section 7.1.1. Each sensor shows changes in signals in different orders and axis directions for the different sources mentioned above and is observed for all cavity tests. The aforementioned operations correlated to the changes in signals suggest that these changes are caused by variations in the magnetization of the sensor components. The changes in the signal of all three sensors were observed and compared for all the mentioned sources at which the change occurs within one test run. Yet, no systematic pattern can be determined regarding the magnetic field axis direction or order of the signal. This absence of exact correlations is the case not only for the signals between different test runs of the same cavity, but is also observed for test runs among magnetic field tests of different vertical tests. To conclude, the operations and changes in the field at the application of B_{ext}, T_c transition, and the removal of B_{ext} result in signal changes that are different for each sensor and are not yet understood.

In the following, the possible causes of varying magnetization of the sensing elements in the sensors are discussed. During T_c transition the Meissner effect may expel magnetic flux differently across the cavity surface. This stems from different crystal orientations within the grains of the niobium [2, p.12]. The presence of grain boundaries also enables fast diffusivity of magnetic flux into the niobium surface. This diffusivity behaviour regarding grain boundaries indicates spatial differences in regard to the magnetic flux trapping behaviour which may lead to the differences in the measured signal. The inhomogeneous surface structure of each cavity includes different surface defects and pinning centers which can cause uneven regional flux trapping or expulsion [3, p.731]. The different allocation of grain boundaries, different surface defects and pinning centres may cause different concentrations of magnetic flux trapping or expulsion within the azimuthal locations of the cavity equator. The three sensors are placed at different azimuthal locations on the equator and may thus be exposed to different concentrations of magnetic flux. This influence seems likely due to the flux trapping being fundamentally influenced by the presence of a strong magnetic field such as 10 µT or 5 µT. The niobium cavity is especially prone to influences on magnetic flux trapping when it surpasses T_c and reaches the Meissner state.

All signal variations between the three sensors are presented in section 7.1.1. This overview makes the con-

nection between the general signal variations and the cavity-specific observations clearer. The range of the signal differences for cavities 1DE9, 1DE19, and 1RI02 lie within about 50 - 1000 nT. Cavity 1AC8 behaves differently and displays notably higher variations between the three sensors. Additionally, one sudden signal shift is observed for both test runs of cavity 1AC8 after cooling down to 2 K. The relevance of this shift is discussed within the corresponding section 6.3 and not taken into account for the comparison of signal variations here. The magnetic field data for 1AC8 are taken at 2 K before this sudden signal shift.

With figure 22 and table 10 it is apparent that the variation of magnetic signals of 1AC8 between the three sensors are exceptionally higher than of all test runs of the other cavities. The different magnetic signals for 1AC8 range between 50-2000 nT before the anomaly of the $3D_2$ signal occurs. This larger change between the signals could be attributed to the single-crystal structure. Another unique property is the heat treatment, that consists of a mid-T heat treatment at 350 °C for 3 h followed by a low-T heat treatment of 130 °C for 24 h. This is the only cavity among the four cavities with an additional low-T treatment. Although both characteristics are unique to this cavity within the scope of this project, they may have contributed to greater magnetization of the sensor components, leading to the observed higher signal differences. Yet, the influence of these factors cannot be confirmed with certainty and more tests with similar cavity attributes would be required for statistical analysis. The absence of the grain boundaries in the single-crystal cavity 1AC8 is assumed to distribute the magnetic flux more evenly than on other cavities with grain boundaries [2, p.12]. The higher differences between the signals comparable to the range between 50-2000 nT of TR 1 was also observed in TR 2 of cavity 1AC8. The anomaly of the sensor $3D_2$ signal is not taken into consideration here for the comparison of sensor signal variations with the other cavities but is further explained in section 6.3.

Cavities 1DE9, 1DE19 and 1RI02 are all made of fine-grain niobium but are subjected to different chemical and heat treatments, which influence their magnetic flux properties. Cavity 1DE9 with electropolishing shows variations between the sensor signals in the range of 50-850 nT as seen in table 8. To obtain statistically valid statements about these variations in signals, another electropolished cavity is required to compare the measured fields by different sensors. Cavity 1DE19 shows variation between the signals of very low values within the range of 100 - 300 nT. This cavity has undergone a mid-T heat treatment at 335 °C for 4.5 hours. Only one test run was conducted for this cavity. Cavity 1RI02 got a long mid-T heat treatment of 300 °C for 20 h. The range between the signal variations of the sensors lies between 100-1050 nT. This cavity shows larger signal variations than 1DE9 and 1DE19.

A further reason for the variations between the sensor signals can be the different temperature gradients during cooldown. Between each of the test runs one warmup to 30 K and one cooldown process to 2 K was performed. This cooldown process may have a minor effect on the mechanical strain of the sensor position and thus reinforce this different magnetic field value measured by each sensor. The temperature gradient during cooldown also affects which part of the cavity is at which temperature at a certain time. [3, p.733] has shown that the temperature distribution is not even during a cooldown procedure. That means that the temperature on the equator of the cavity is not identical at all azimuthal positions of the cavity at a certain time. This can lead to different times for the transition through T_c depending on the temperature sensor location on the equator. The different times of T_c transition on the equator may influence the magnetic flux measured by each sensor at 2 K and depends on the sensor location on the equator. This shows that the magnetic flux trapping does not happen at the same time. Another cause for the signal variations can be different sensor calibrations. This can be investigated after a recalibration of all sensors via Bartington®.

In conclusion, the exact cause of the variations between magnetic field signals recorded by the different sensors on the equator of the cavity can not be determined with certainty. However, the different structure of the niobium surface, different chemical and heat treatments and different temperature gradients are likely to contribute to these variations of the sensor signals. A promising proposal to further study the signal variations of the measured magnetic flux in regard to the azimuthal sensor position at the cavity equator, would be to switch the sensor positions. This way, the spatial impact could be directly compared within different test runs. Additionally, well-defined sensor positions are necessary to compare magnetic signals measured at different vertical tests. This can be achieved by implementing defined holding systems for each sensor. Despite the undefined sensor positions in regard to the cavity, the insert is mounted into the cryostat following a system for precise comparability. This indicates that the angle positions of the insert in regard to the cryostat are comparable between each vertical test.

7.2 Correlation of Sensitivity with Heat Treatments and Temperature Gradients

In this section the different sensitivities measured for each of the cavities are discussed and correlated to their respective heat treatment and temperature gradient during cooldown. In the following table the calculated sensitivity values as a function of E_{acc} are presented with their calculated uncertainty to compare the values for the different vertical tests with different cavities.

Table 13: Comparison of sensitivity as a function of E_{acc}. In the first line of the table is the sensitivity with the corresponding cavity name, in the second line are the test runs of the cavity. Sensitivities for E_{acc} values of 4 MV/m, 5 MV/m and 8 MV/m are compared.

S_{1DE9} [nΩ/μT]		S_{1DE19} [nΩ/μT]	S_{1AC8} [nΩ/μT]	E_{acc} [MV/m]
TR 1	TR 2	TR 3	TR 4	
10.43 ± 1.73	12.33 ± 1.61	35.65 ± 3.82	30.19 ± 4.05	4
10.77 ± 1.76	12.68 ± 1.65	37.08 ± 3.96	31.31 ± 4.18	5
11.77 ± 1.87	13.68 ± 1.75	40.63 ± 4.29	35.20 ± 4.59	8

S_{1RI02} [nΩ/μT]				Eacc [MV/m]
TR 1	TR 2	TR 3	TR 4	
29.08 ± 3.19	29.21 ± 3.20	28.67 ± 3.13	23.96 ± 2.93	4
30.33 ± 3.31	30.54 ± 3.33	29.94 ± 3.25	25.03 ± 3.02	5
32.86 ± 3.54	33.33 ± 3.60	32.85 ± 3.52	27.41 ± 3.23	8

Figure 31 provides an overview of the different cavity treatments and the sensitivity values of their different test runs.

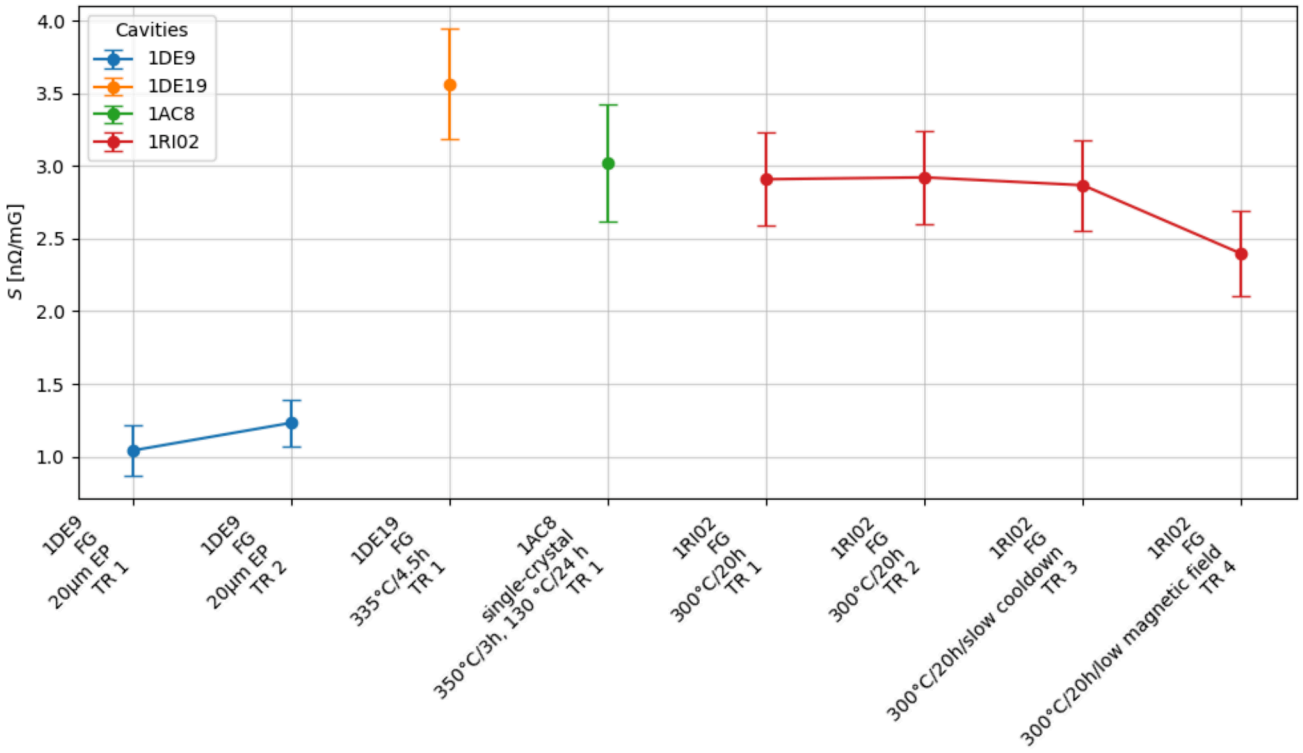

Figure 31: Comparison of the sensitivities between the different heat treatments and material properties measured at 4 MV/m.

To compare the sensitivity values in nΩ/mG, all values in nΩ/μT can be divided by a factor 10. The sensitivity of cavity 1RI02 is calculated for TR 1, TR 2, TR 3, and TR 4. TR 3 and TR 4 are different are exhibited to different test conditions then the other cavity tests. TR 1 and TR 2 were conducted with the standard cooldown rate comparable to the other cavity tests, TR 3 was performed with a significantly slower cooldown rate. In TR 4, a lower current of 13 mA was used to induce the magnetic field of 5 μT instead of 10 μT. The uncertainties presented in the table present the uncertainty for comparison between different vertical tests. Taking these uncertainties into account, it can be seen that the sensitivity of 1AC8 and 1RI02 are in identical order.

7.2.1 Comparison of Sensitivity for Different Cavity Treatments

In table 13 the sensitivity of at least two different test runs can be compared for cavity 1DE9, and for cavity 1RI02. Cavity 1DE19 and 1AC8 have sensitivity values of only one test run. [24, p.2765] compared S as a function of E_{acc} among different heat treatments of the same cavity. In figure 32 (a) the results of [24] are compared to the results presented here in this thesis (b).

The cavity treatments in [24] are different from the cavity treatments discussed within this project. Overall, it can be seen that the sensitivity values in figure 32(a) are generally lower than in figure 32(b). Additionally, the noted temperature and duration of the treatments discussed within this work can deviate from the actual temperature and duration of the heat treatment. Nonetheless, for an approximate comparison these nominal parameters regarding the heat treatments were used in this following discussion. All cavity heat treatments in figure 32 were performed for 3 h but at different temperatures. The cavities in this project vary in both treatment duration and temperature.

The EP cavities TE1-06-EP (dark blue) in figure 32 (a) and 1DE9 (light blue and darker blue) in figure 32 (b) have both undergone electropolishing, and yet show notable differences in their sensitivity to magnetic flux. Cavity TE1-06-EP displays accelerating field to approximately 25 MV/m, while cavity 1DE9 shows higher accelerating gradients of up to 30 MV/m, followed by a sudden drop, namely the well known high-field-Q-slope. At an accelerating gradient of 4 MV/m, TE1-06-EP exhibits a very low sensitivity of approximately 0.3 nΩ/mG, whereas 1DE9 reaches about 1 nΩ/mG. While both cavities have undergone similar surface treatments and their sensitivity curves follow a generally increasing trend with increasing E_{acc}, the higher sensitivity values observed in 1DE9 may be attributed to material differences or other factors, such as the grain structure.

Cavity 1DE19 (dark green) in figure 32 (b) has undergone a mid-T heat treatment at 335 °C for 4.5 hours. Its sensitivity curve begins just below 3 nΩ/mG, gradually increases, and then slightly flattens while it continually rises until it ends at around 4 nΩ/mG. The corresponding accelerating gradient goes to 21 MV/m before the cavity quenches. The slight flattening of the sensitivity curve happens at approximately 10 MV/m.

Two cavities in figure 32 (a), both subject to a mid-T heat treatment for 3 hours but at different temperatures than 1DE19, show comparable curve shapes. The sensitivity curve of cavity TE1-05-300 °C (red) displays a similar gradual flat rise but with overall lower sensitivity values than in 1DE19. TE1-05-300 °C starts its sensitivity curve at about 1.6 nΩ/mG and ends at about 2.5 nΩ/mG. Its accelerating field ranges up to 22.5 MV/m. Cavity TE1-06-325 °C (pink) also exhibits a similar sensitivity curve profile but with a more steadily rising curve than in 1DE19. It begins at approximately 1.4 nΩ/mG and reaches about 2 nΩ/mG before quenching at 22.5 MV/m. Overall, cavity 1DE19 in figure 32 (b) and cavity TE1-05-300 °C, and TE1-06-325 °C in figure 32 (a) show similar accelerating gradients and curve shapes but different absolute values. These differences may be attributed to different test conditions, heat treatments and material properties.

Cavity 1AC8 in figure 32 (b) is a single-crystal niobium cavity with a two-step heat treatment of 350 °C for 3 hours (mid-T) followed by 130 °C for 24 hours (low-T). Its sensitivity curve starts at about 2.7 nΩ/mG and ends at 8 nΩ/mG, with accelerating gradients of up to nearly 40 MV/m. This wide range of the accelerating gradient and surprisingly high sensitivity makes 1AC8 the cavity with the highest accelerating fields in figure 32 (b). The sensitivity curve for 1AC8 initially starts with a relatively sharp rise, followed by a flattening at around 15 MV/m, and then a strong increase starting at about 35 MV/m can be seen until the quench at about 40 MV/m. This behavior is unique compared to other sensitivity curves in figure 32 (b) but shares similarities with cavity TE1-06-150 °C (beige) in figure 32 (a). TE1-06-150 °C also shows a late-stage rise at high gradients, although its maximum sensitivity of 1.7 nΩ/mG is significantly lower than that of 1AC8. The accelerating gradient for TE1-06-150 °C

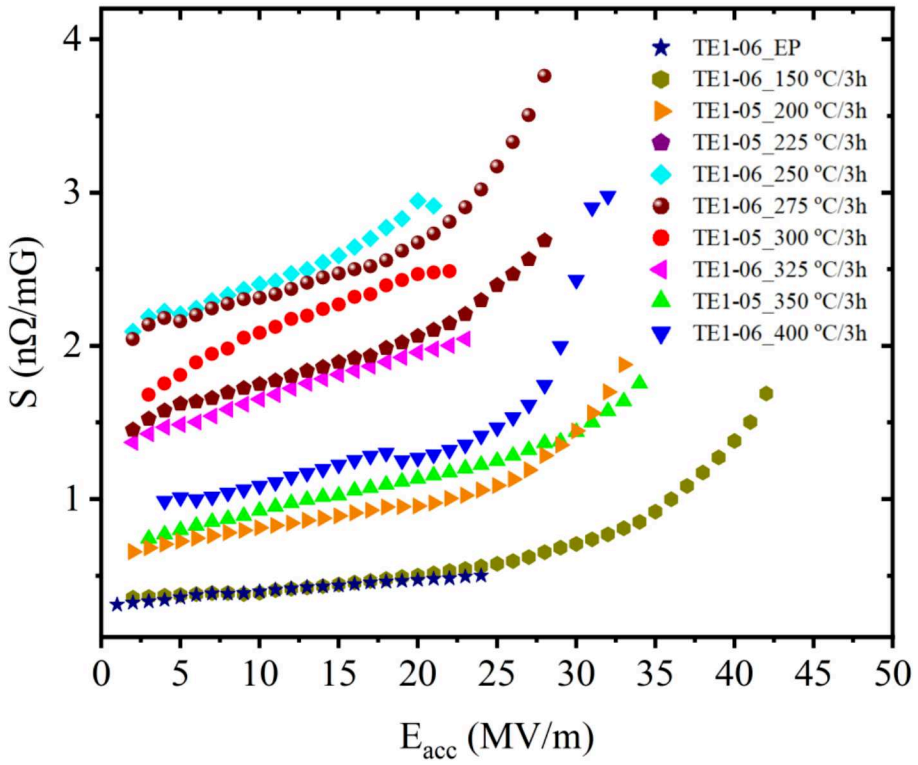

(a)

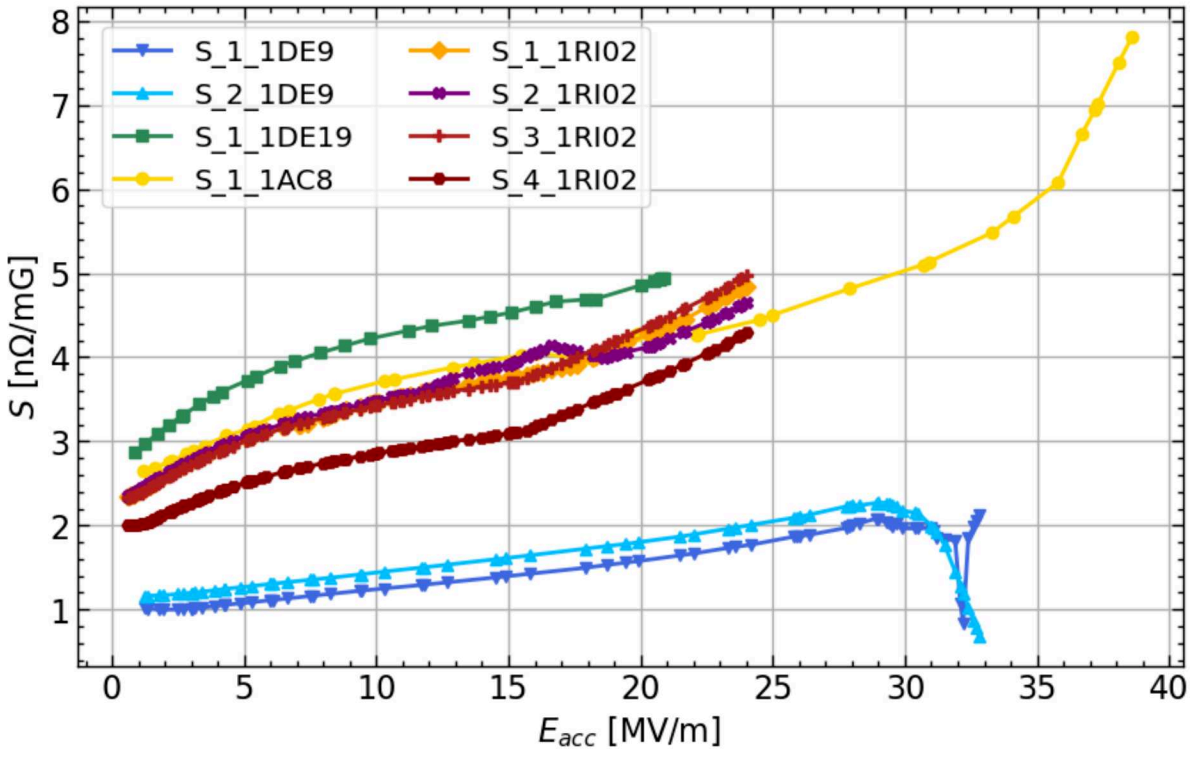

(b)

Figure 32: Comparison of the sensitivities measured on cavities with different heat treatments. (a) S as a function of E_{acc} between different heat treatments in [24, p.2765]. (b) S as a function of E_{acc} for cavities studied in this project.

reaches up to 43 MV/m, similar to 1AC8. The similarity in the late-stage rise at high gradients between 1AC8 and TE1-06-150 °C suggests that this characteristic is caused by the low-T heat treatment common for both cavities in figure 32 (a) and in figure 32 (b). However, the unique shape of the sensitivity curve of 1AC8, especially the strong initial rise and flattening at medium accelerating gradients, could be attributed to its single-crystal niobium structure. The single-crystal niobium structure of 1AC8, unique within the treatments in figure 32 (b), may exert different influences than on polycrystalline niobium.

In total, cavity 1AC8 shows the highest sensitivity and accelerating gradients in figure 32 (b). Although its sensitivity curve shape differs from most cavities in figure 32 (a), its strong rise at high accelerating gradients is similar to TE1-06-150 °C. The different shape suggests an influence by the different niobium properties but a similarity due to the low-T heat treatment.

Cavity 1RI02 in figure 32 (b) has undergone a long mid-T heat treatment at 300 °C for 20 hours. This cavity was tested four times. TR 1 (orange) and TR 2 (purple) are directly comparable to the test conditions of the other cavities in figure 32 (b). TR 3 (dark red) has a lower cooldown gradient, and TR 4 (brown) was tested with a significantly lower applied magnetic field. All four test runs show a thermal breakdown at approximately 24 MV/m.

The sensitivity curves of TR 1, TR 2, and TR 3 all start at about 2.5 nΩ/mG and quench at about 4.5 nΩ/mG. TR 4 starts at lower sensitivity than these three test run, at about 2 nΩ/mG and ends slightly below the others, at 4.3 nΩ/mG. This lower sensitivity curve of TR 4 is likely attributed to the reduced applied magnetic field. The reduced external field and thus the lower presence of magnetic flux indicates a lower sensitivity to magnetic flux. Also, despite the lower cooldown gradient of TR 3, the sensitivity curve of TR 3 closely overlaps that of TR 1. This similarity suggests that the slower cooldown did not significantly affect the overall sensitivity of this cavity.

In particular, the sensitivity curve of TR 2 exhibits a unique feature where an elevation between approximately 12 MV/m and 18 MV/m can be seen. Afterwards, the sensitivity increases sharply as in the curves of the other test runs and follows their common trend of a rising curve. This behavior is absent in other cavities in figure 32 (b) and can not be directly correlated to any cavity in figure 32 (a). However, a type of similarity can be seen in the curve of TE1-06-400 ° in figure 32 (a), which displays a dip at a comparable accelerating gradient similar to the elevation in TR 2 of 1RI02. This dip is also followed by a rising trend and therefore suggests some yet unknown instability in this region.

Generally, the slow increase of the sensitivity values in the test runs of 1RI02 in figure 32 (b) with a more abrupt increase starting at around 14 MV/m is comparable with the behavior observed in several cavity treatments in figure 32 (a). Cavities TE1-05-200 °C (orange), TE1-06-275 °C (dark brown), TE1-05-225 °C (turquoise), TE1-05-350 °C (light green), and TE1-06-400 °C (dark blue) all show a similar shape with an initial gradual rise that is followed by a stronger incline at medium accelerating gradients. The most consistent difference in figure 32 (a) are the higher accelerating gradients of these cavities compared to 1RI02 in figure 32 (b). Another difference between the treatments in 32 (a) compared to 1RI02 in 32(b) lies in the absolute sensitivity values where cavity 1RI02 exhibits larger sensitivity across all test runs compared to data in figure 32 (a). This difference is likely due to different test conditions. Particularly the different sensitivity values between the test runs of a higher and lower magnetic field applied between TR 1, TR 2, and TR 3 in comparison to TR 4 shows the clear influence on the sensitivity by the external field. Overall, the curve shape of 1RI02 in figure 32 (b) can be correlated to several sensitivity curves in figure 32 (a).

To conclude, in figure 32 (b) can be seen, that with the exception of the single-crystal cavity 1AC8, cavities with mid-T heat treatment quench at decreased accelerating gradients compared to the cavity with EP.

Overall, the sensitivity values in figure 32 (b) are higher by about a factor 2 than the sensitivity values in figure 32 (b). This result may stem from different test conditions or niobium characteristics, such as fine-grain, large-grain and single-crystal. No definite information regarding the niobium structure of the cavities in [24] was found. However, observing the lower sensitivity curve in TR 4 (lower magnetic field) of cavity 1RI02, it is very likely that the difference in sensitivity order stems from differences in regard to the magnetic test conditions. The different cooldown gradients can also influence the sensitivity of the cavity and are discussed in section 7.2.2.

Due to the completely different treatments the cavities within this work were subjected to, the oxygen diffusion length l can be used as a parameter for further comparison. The oxygen diffusion length shows the impact of the heat budget on the niobium. As 1DE9 was only electropolished, no diffusion length was calculated here. The

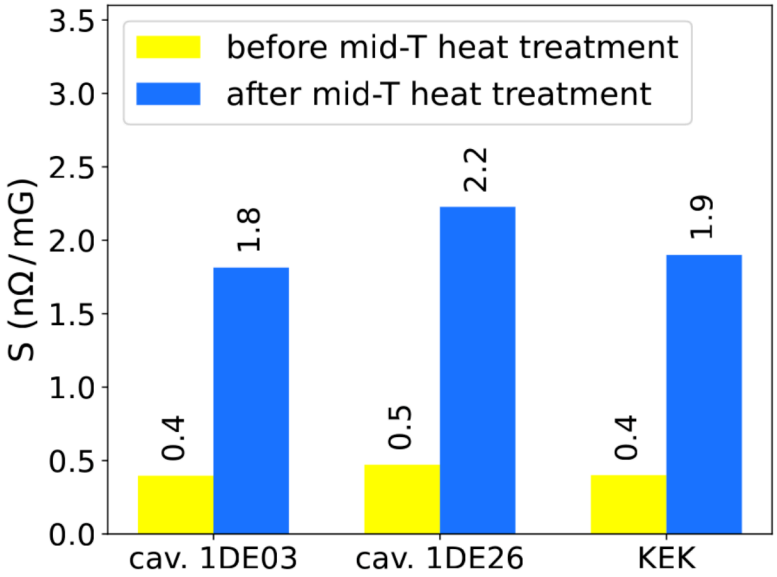

Figure 33: Sensitivity values for three different cavities before and after mid-T heat treatment [2, p.14].

diffusion length of 1DE19 is 1248 nm [2, p.6]. The diffusion length of cavity 1RI02 is 2387 nm calculated with the same method. The positioning of the temperature sensors in the ultra-high vacuum furnace is shown in [2, p.3]. Usually the temperature sensor closest to the cavity equator is used to calculate the diffusion length. The diffusion length of cavity 1AC8 was only determined after its mid-T heat treatment with approximately 2844 nm but not after its later low-T heat treatment. For 1AC8 the diffusion length was deduced for the temperature sensor TR2, which was not located closest to the cavity equator. This was due to a sensor failure and hence this value is only a rough assumption. In table 13 it can be seen that 1AC8 with the mid-T heat treatment of 300 °C/3 h followed by the low-T heat treatment of 130 °C/24 h shows nearly identical sensitivity values to 1RI02 subjected to the long mid-T heat treatment of 300 °C/20h. The diffusion length of 1AC8 with >2500 after the mid-T heat treatment is comparable to the diffusion length of 1RI02 with 2387 nm. This similar diffusion length may explain the nearly identical sensitivity to magnetic flux. Yet, this hypothesis is incomplete due to the absence of data on the diffusion length of 1AC8 after the later low-T heat treatment.

Taking into consideration the uncertainty of each sensitivity value, cavities 1DE19, 1AC8 and 1RI02 show comparable sensitivity to magnetic flux. In the results of [24, p.2765] can be seen that the sensitivity increases with increasing heat budget of the cavity treatment, which implies a higher oxygen diffusion length. However, the maximum of the sensitivity was not observed at the highest heat budget but at about 250 °C to 275 °C. Heat treatments with higher temperatures show decreased sensitivity again. This describes a non-linear correlation between the temperature treatments and the sensitivity. When neglecting the uncertainty of the sensitivity values, then 1DE19 has a slightly higher calculated sensitivity and a lower diffusion length than 1RI02 and 1AC8, which both have a higher diffusion length and a lower sensitivity. The higher S and lower diffusion length of 1DE19 fits to data at 250 °C and 275 °C in [24, p.2765].

In figure 33, taken from [2], it can be seen that the sensitivity of the same cavity increases significantly after mid-T heat treatment.

In this figure 33 it can be seen that the sensitivity is increased by a factor 4.5-5 after mid-T heat treatment. The cavities analysed in the scope of this project were not compared before and after mid-T heat treatment. However, cavity 1DE9 received only EP and can be compared to the three other cavities 1DE19, 1AC8, and 1RI02 with mid-T heat treatment. Here a factor of 3-3.5 increase in sensitivity can be observed for the cavities with mid-T heat treatment compared to the EP cavity. This shows that the same trend occurs in both studies. The different size of the factor may stem from different material properties of the cavities, different test conditions and different temperature

gradients. This is especially likely since different cavities are correlated for their sensitivity within this work instead of observing the same cavity before and after mid-T heat treatment. Additionally, different measurement methods, sensors and cavity properties between both studies likely have an influence on the comparison.

7.2.2 Comparison of Temperature Gradients

In [3] two cavities were measured in regard to their different temperature gradients and their sensitivity. The two cavities 1DE26 (280°/3 h) and 1DE9 (300°/3h) both had a mid-T heat treatment in these tests. To avoid confusion, cavity 1DE9 as it is used within this project was electropolished only later and is therefore not comparable to the condition of cavity 1DE9 in [3] concerning its treatment. Cavity 1DE9 in this work is therefore named 1DE9-EP in the following. In [3], the spatial temperature gradient was calculated from the temperature difference between the temperature sensor of the upper and lower beam pipe as is described in section 6.1. The values of the time-dependent cooldown gradient and the spatial temperature gradient can be seen in the corresponding tables 4, 5, 6, 7 in section 6. The spatial temperature gradients during cooldown shown in these tables vary between 3.4 K to 10.3 K for cavities 1DE9, 1DE19, 1AC8 and 1RI02.

Although the notation of $\Delta\mathrm{K}/\Delta l$ is used in [3], the spatial temperature gradient here is only notated as ΔK and the values are directly comparable to the values notated with $\Delta\mathrm{K}/\Delta l$. The length between the highest and lowest temperature sensors is 225 mm [2, p.12]. In [3, p.733] a lower spatial temperature gradient of 0 ΔK and a larger gradient of 4 ΔK were used for both tested cavities. For the lower temperature gradient cavity 1DE9 showed that the mid-T heat treatment caused the sensitivity to increase by a factor five. It went from 3.1 nΩ/μT to 15.7 nΩ/μT with the larger temperature gradient, and from 3.5 nΩ/μT to 17.7 nΩ/μT with the lower temperature gradient. Within this here presented study, the same cavity cannot be compared before and after mid-T heat treatment. However, the different temperature gradients can be correlated to the different test runs of the same cavity.

The temperature gradients of 1DE19 and 1AC8 cannot be compared to another test run of the same cavity. 1RI02 has 6.0 ΔK in TR 1, 7.9 ΔK in TR 2, and 3.4 ΔK of the slow cooldown in TR 3. The sensitivities of 1RI02 can be seen in table 13. The uncertainty in table 13 is overestimated for comparing test runs of the same vertical test. TR 4 of cavity 1RI02 cannot be compared to the other test runs of 1RI02 regarding its temperature gradient due to the additional parameter of the lower magnetic field. The sensitivity is compared at 4 MV/m in both studies [3]. The larger gradients of TR 1 and TR 2 result in slightly larger S values and slightly lower ΔB_{ext} values than in TR 3. In table 13 and in figure 32 can be seen that TR 1 and TR 2 with the higher spatial temperature gradients show slightly higher sensitivity than the sensitivity of TR 3 with the lower gradient. These data indicate that a lower spatial temperature gradient leads to a slightly lower sensitivity. This correlation regarding the temperature gradient is the opposite of the correlation in [3, p.733], where a lower temperature gradient leads to a higher sensitivity. Nonetheless, the difference within the sensitivity of TR 1, TR 2, and TR 3 is very low and lies within the uncertainty for different test runs within the same vertical test. The lower uncertainty of sensitivity for the same vertical test is attributed to 3 % for Q_0, 1 % for E_{acc}, and a σ_{3D} of 1 nT for ΔB_{ext}[10, p.9].

For cavity 1DE9-EP, the spatial gradient of 10.3 ΔK in TR 1 results in lower S values and 4.9 ΔK in TR 2 in higher S values. Here, the larger temperature gradient results in a lower S and the lower gradient results in a higher S. This correlation matches the results in [3, p.733].

Generally it can be concluded that cavity 1RI02 has the temperature gradients go from lowest to highest in the order of TR 3 < TR 1 < TR 2 < TR 4. This is reflected in the quality factor curves seen in figure 29, where the lowest curve is shown for TR 3, followed by TR 1, TR 2, and TR 4. The quality factor is calculated with the factor ΔB_{ext} from the surface resistance, which is the inverse of the quality factor with an additional geometry factor. The trend of the higher quality factor resulting from a larger temperature gradient therefore correlates with data in [3, p.733]. For cavity 1DE9 the temperature gradient is higher for TR 1 and lower for TR 2. The corresponding behaviour can be seen in figure 13, where TR 1 shows a higher measured quality factor curve and TR 2 has a lower measured quality factor curve.

These correlations to the quality factor of both cavities in regard to the temperature gradient show that the larger temperature gradient exhibits a higher quality factor and the lower temperature gradient exhibits a lower quality factor.

Another factor of influence on the correlation of the temperature gradient to the sensitivity is the inhomogeneous rate at which the temperature changes during the cooldown procedure. This causes that different temperatures are measured in different regions of the cavity at a certain time. As demonstrated by [3, p.733], the thermal profile is not uniform throughout the cavity during cooldown. This implies that at a certain time no uniform temperature can be found at different positions on the equator of the cavity. Differences in the results may also be attributed to the highly monitored test conditions in [3] compared to the test conditions here.

8 Conclusion

In the scope of this project, the possibility to measure magnetic flux trapping sensitivity with parasitic measurement methods at DESY has been achieved for the first time. These promising results were only possible due to systematic measurement approaches, such as the adjustment of different filter systems, new electronic components, and data acquisition. The measurement constellation with the built-in Helmholtz coil for the application of an external magnetic field in the insert allows for these parasitic sensitivity measurements along standard cavity performance tests in the future.

Based on the findings on the variations between the magnetic sensor signals measured by three sensors located at the cavity equator, the consistency between the signals greatly differs between two different test conditions. In one of the two test conditions a strong magnetic field (B_{ext}) is applied during cooldown and the critical temperature T_c transition, but it is removed during the magnetic field test at 2 K. In the other test condition (baseline) no external magnetic field is present during cooldown. While the signals recorded under baseline conditions are mostly comparable across all sensors and tested cavities, the signals taken under strong magnetic field conditions vary significantly for the different sensors. Three different sources are determined to cause the divergence of the sensor signals in different axis directions without a recognizable pattern among all tests. The signals diverge during the application of an external magnetic field, at T_c transition, and at the removal of the external field. The differences in signal strengths appear not only between magnetic signals across repeated test runs on the same cavity, but also within the same test run. Thus, different sensors measure a different signal at the same time despite them all being located on the cavity equator. These discrepancies in sensor signals lie in the range of several hundred nanoteslas. The origin of the variations can be correlated to the high sensitivity to magnetic flux of the magnetic sensors themselves.

Several contributing factors causing variations in sensor signals across all tests are identified. First, the differences in the local surface structure of the cavity, which seems to impact the measured signal of the three sensors at different azimuthal positions on the equator. Second, the chemical and thermal treatments can cause different magnetic flux trapping behaviour. Third, different temperature gradients during the cooldown procedure of each test run on the same cavity may have an impact. While three cavities within this work are fine-grain cavities, the sensor signal variations of the single-crystal niobium cavity have shown to be especially interesting. This cavity is unique in its crystalline structure and also in its additional low-T heat treatment. The single-crystal cavity exhibits the highest signal differences ranging up to 2000 nT. Although these data suggest a correlation between these cavity-specific characteristics and the increase in signal variations, no absolute relationship can be confirmed. Future studies are required to draw a more definite conclusion regarding the behaviour of magnetic signals measured by the sensors and should focus on controlling and isolating contributing variables. The sensors in future studies need to be mounted in reproducible positions on the cavity and require more repeated tests, switching the positions of the sensors in order to better understand these inconsistencies.

The sensitivity values between the cavity tests within this work in comparison to the work of [24] reveal consistent differences and similarities in both absolute sensitivity and curve shapes. Although the mid-T heat treated cavities in this work exhibit generally higher sensitivity values than of comparable data, similarities in the curve behaviour can be observed, such as the gradual rise and increased incline at mid-range accelerating gradients. Also, the correlation between the strength of the applied magnetic field in regard to the resulting sensitivity is clearly evident. The particularly high sensitivity at high accelerating gradients of the single-crystal cavity highlights the possible impact of the niobium grain structure and the low-T heat treatment. Overall, the sensitivity data within

this work shows several similarities with [24] in sensitivity curve shape and accelerating gradients.

A correlation between the oxygen diffusion length and the sensitivity to magnetic flux was explored via comparison of the diffusion length data among three mid-T heat treated cavities. All three cavities show comparable sensitivity while the oxygen diffusion length of one cavity is significantly lower than of the other two. This suggests a nonlinear relationship where the sensitivity does not continually increase with longer diffusion lengths. This aligns with the findings in [24], which show that a peak in sensitivity at medium heat budgets is followed by a decline in sensitivity for higher temperatures. Despite this expected outcome, incomplete data collection due to broken temperature sensors in the furnace prevents a more precise analysis of diffusion lengths in this project, which could have determined a more reliable correlation between the oxygen diffusion length and the sensitivity.

Moreover, it is confirmed that mid-T heat treatments consistently increase the sensitivity to trapped magnetic flux. It is also observed that the mid-T heat treated cavities show decreased accelerating gradients in comparison to cavities which are electropolished and have a low-T heat treatment, as it is the case for cavities treated by the current EuXFEL recipe. It is demonstrated that the sensitivity of cavities after a mid-T heat treatment is up to 3-5 times higher compared to before this heat treatment. The factor of sensitivity increases after mid-T heat treatments deviates from [2, p.14]. This deviation can be attributed to the different test conditions, where the same cavity was tested before and after mid-T heat treatment in [3, p.14], whereas here different cavities were compared. Thus, several differences such as material properties, temperature gradients and sensors impact the differences in sensitivity comparison. Nevertheless, both studies definitely show that mid-T heat treatments lead to a significantly enhanced sensitivity to trapped magnetic flux.

The comparison of spatial temperature gradients during cooldown and their impact on the sensitivity shows that for the mid-T heat treated cavity the sensitivity for different temperature gradients is comparable considering the measurement uncertainty. For the cavity with electropolishing, the larger temperature gradient leads to lower sensitivity, which is in alignment to the correlations found in [3]. Despite the similarity in sensitivity for different temperature gradients for the mid-T heat treated cavity, the expected correlation is found in its quality factor for the different test runs and is consistent between both cavities. Influences on the differences in both studies may be attributed to different test conditions, sensors, and cavity properties. More statistics will help to draw conclusions in the future.

In summary, this study provides valuable insights into the performance of niobium 1.3 GHz SRF cavities, particularly on the impact of medium-temperature heat treatments on sensitivity to magnetic flux trapping. For the first time at DESY, sensitivity to magnetic flux was deduced by parasitic measurements. This possibility is only enabled by a systematic approach to both the experimental setup and data analysis, which provided these invaluable results. The here analysed data show that mid-T heat treatments significantly increase the sensitivity to magnetic flux compared to cavities without this heat treatment. Additionally, it is explored to what extent the temperature gradient impacts the sensitivity of the cavity, although more data is required to identify a final link. The study also examines the variations of magnetic field signals measured by different sensors on the cavity equator. Overall, these findings emphasize the importance of thermal influences and material properties to optimize SRF cavities. This indicates that the magnetic hygiene of the cavity environment becomes a very important point in order to avoid flux trapping. These insights form a paramount foundation for future research aimed at refining the cavity design of a second generation of mid-T/low-T heat treated cavities, which can be used for the upgrade of the European XFEL.

References

[1] H. Ito, H. Araki, K. Takahashi, and K. Umemori. Influence of furnace baking on q–e behavior of superconducting accelerating cavities. *Progress of Theoretical and Experimental Physics*, 2021(7):071G01, 2021. doi:https://doi.org/10.1093/ptep/ptab056.

[2] C. Bate, K. Kasprzak, D. Reschke, L. Steder, L. Trelle, H. Weise, M. Wiencek, and J. Wolff. Correlation of srf performance to oxygen diffusion length of medium temperature heat treated cavities. *Superconductor Science and Technology*, 38(2):025003, 2025. doi:https://doi.org/10.1088/1361-6668/ad9fe8.

[3] J. Wolff, J. Eschke, A. Gössel, W. Hillert, K. Kasprzak, D. Reschke, L. Steder, L. Trelle, M. Wiencek, et al. Impact of medium temperature heat treatments on the magnetic flux expulsion behavior of srf cavities. 2023. doi:10.18429/JACoW-SRF2023-WEPWB065.

[4] H. Padamsee, J. Knobloch, and T. Hays. *RF Superconductivity for Accelerators*. Wiley Series in Beam Physics and Accelerator Technology. Wiley, 1998. ISBN 9780471154327. URL `https://books.google.de/books?id=2leaQgAACAAJ`.

[5] J-M. Vogt, O. Kugeler, and J. Knobloch. Impact of cool-down conditions at t c on the superconducting rf cavity quality factor. *Physical Review Special Topics—Accelerators and Beams*, 16(10):102002, 2013. doi:https://doi.org/10.1103/PhysRevSTAB.16.102002.

[6] F. Schlander. Results on quality factors of 1.3 ghz nine-cell cavities at desy. *SRF2013, Paris, France*.

[7] Jacek Sekutowicz. Personal communication, 2025.

[8] B Bein. Systematic studies of a cavity quench localization system. Technical report, Deutsches Elektronen-Synchrotron, 2019.

[9] Y. Bozhko, V. Anashin, L. Belova, T-A. Boeckmann, M. Kholopov, V. Konstantinov, B. Petersen, S. Pivovarov, E. Pyata, D. Sellmann, et al. Test stands for testing serial xfel accelerator modules. In *AIP Conference Proceedings*, volume 1434, pages 1100–1107. American Institute of Physics, 2012. doi:https://doi.org/10.1063/1.4707030.

[10] D. Reschke, V. Gubarev, J. Schaffran, L. Steder, N. Walker, M. Wenskat, and L. Monaco. Performance in the vertical test of the 832 nine-cell 1.3 ghz cavities for the european x-ray free electron laser. *Physical review accelerators and beams*, 20(4):042004, 2017. doi:10.1103/PhysRevAccelBeams.20.042004.

[11] J. Polinski, M. Chorowski, P. Duda, Y. Bozhko, B. Petersen, and J. Schaffran. Design and commissioning of vertical test cryostats for xfel superconducting cavities measurements. In *AIP Conference Proceedings*, volume 1573, pages 1214–1221. American Institute of Physics, 2014. doi:https://doi.org/10.1063/1.4860844.

[12] Thomas Scherbacher. 3d magnetic field measurements on superconducting cavities with bartington® cryomag® sensors at desy. Bachelor's thesis, 2023.

[13] Bartington Instruments. *Operation Manual for CryoMag® Three-Axis Magnetic Field Sensor*. Bartington Instruments, n.d.. Operational manual.

[14] Wikipedia contributors. Fluxgate magnetometer. `https://en.wikipedia.org/wiki/Magnetometer#Fluxgate_magnetometer`. Accessed: May 9, 2025.

[15] Bartington Instruments. *CryoMag® Three-Axis Magnetic Field Sensors*. Bartington Instruments, n.d.. Data sheet.

[16] Bartington Instruments. Operation manual for mag-01 mag-01h single axis fluxgate magnetometers with mag probes b-g, n.d.. Operational Manual.

[17] Foerster. *Product Information: MAGNETOSCOP 1.070 Portable Magnetometer*. Foerster, n.d.. Product manual.

[18] Foerster. Calibration certificate: Foerster magnetometer, n.d.. Calibration certificate.

[19] Wikipedia contributors. Helmholtz-Spule – Wikipedia, die freie Enzyklopädie, 2025. URL `https://de.wikipedia.org/wiki/Helmholtz-Spule`. Accessed: May 9, 2025.

[20] Bartington Instruments. *Operation Manual for DecaPSU Power Supply Unit*. Bartington Instruments, n.d.. Operational manual.

[21] Bartington Instruments. Mag-01h single axis fluxgate magnetometer, n.d.. Product datasheet.

[22] Hinweise zum Physikalischen Praktikum I & II für Studierende der Naturwissenschaften. Praktikum script, n.d. Unpublished course material.

[23] F. Kramer, S. Keckert, O. Kugeler, and J. Knobloch. Systematic investigation of flux trapping dynamics in niobium samples. *Proc. IPAC'22*, pages 1200–1203, 2022. doi:10.18429/JACoW-IPAC2022-TUPOTK006.

[24] P. Dhakal, B. Khanal, E. Lechner, and G. Ciovati. Impact of medium temperature heat treatment on flux trapping sensitivity in srf cavities. *JACoW Publishing*, 2024. doi:10.18429/JACoW-IPAC2024-WEPS33.

Acknowledgements

I would like to express my gratitude to all those who have supported and guided me throughout the entire process of this bachelor research project. This work would not have been possible without the expertise and collaboration of many individuals.

First of all, I am very grateful to my supervisors, Prof. Dr. Wolfgang Hillert and Dr. Lea Steder, for the opportunity to pursue this project. I am especially thankful to Dr. Lea Steder for her continuous support and mentorship throughout every stage of this research. Her constant feedback and availability were invaluable.

I would also like to thank Dr. Marc Wenskat for initiating the contact with the MSL Group at DESY and Detlef Reschke for the helpful input on the theoretical aspects of this project. Special thanks go to Dr. Mateusz Wiencek, who played a fundamental role in performing all the measurements in the AMTF and generously offered his time and support whenever I needed it. Moritz Korf played a supporting role in the success of processing the measurement data. His help allowed me to overcome challenges that would have been difficult to solve within the same time frame otherwise. Furthermore, I would like to acknowledge Carsten Müller and the team at the electrical laboratory for providing and installing the necessary electrical components for my measurements in the AMTF. Lastly, I want to thank Tristan de Lange for reviewing the language aspect of this thesis and for offering mental support throughout this challenging journey.

This project was a collective effort which not only shaped my understanding in regard to this research field, but also provided me with valuable skills for my academic future.

Statutory Declaration

I declare that I have authored the Bachelor's thesis independently and have not used any aids other than those specified. I have clearly labelled all passages that are taken from other works in terms of wording or meaning as borrowed material, stating the exact source in each case. I confirm that I have not already submitted this thesis in the same or a similar version in another examination procedure. If electronic aids based on generative artificial intelligence (gAI) were used in the course of the preparation of this Bachelor's thesis, I confirm that my own work was the main focus and that complete documentation of all aids used is available in accordance with good scientific practice. I am responsible for any incorrect or distorted content, incorrect references, violations of data protection and copyright law or plagiarism generated by the gAI. I agree that the Bachelor's thesis may be published.

Hamburg, 18/05/2025
Place, Date


Signature